Bulk and surface ordering phenomena in binary metal alloys

2003 J. Phys.: Condens. Matter 15 R1429

(http://iopscience.iop.org/0953-8984/15/34/201)

INSTITUTE OF PHYSICS PUBLISHING JOURNAL OF PHYSICS: CONDENSED MATTER

J. Phys.: Condens. Matter **15** (2003) R1429–R1500 PII: S0953-8984(03)34491-1

TOPICAL REVIEW

Bulk and surface ordering phenomena in binary metal alloys

Stefan Müller

Lehrstuhl für Festkörperphysik, Universität Erlangen-Nürnberg, Staudtstraße 7, 91058 Erlangen, Germany

E-mail: s.mueller@fkp.physik.uni-erlangen.de

Received 13 March 2003
Published 15 August 2003

Abstract

In the 1988 edition of Nature's 'News and Views', J Maddox wrote that '*one of the continuing scandals in physical sciences is that it remains in general impossible to predict the structure of even the simplest crystallographic solids from knowledge of their chemical composition*' (Maddox 1988 *Nature* **335** 7). There is, however, the possibility of making some progress in this direction by combining two fundamental areas of physics: quantum mechanics and statistical physics. The starting point is an electronic structure theory density functional theory (DFT) (Hohenberg and Kohn 1964 *Phys. Rev.* **136** 864B, Kohn and Sham 1965 *Phys. Rev.* **140** 1133A) which independently establishes the range (first neighbours, second neighbours, etc), type (pairs, three body, four body, etc) and chemical character (charge transfer, atomic site effects, etc) of the interaction energies. All these can be determined from cluster expansions (CE) (Sanchez *et al* 1984 *Physica* A **128** 334) which give access to both huge parameter spaces (e.g. for ground-state searches) and systems containing more than a million atoms (e.g. for microstructure studies). It will be shown that, together with Monte Carlo simulations, CE open the possibility of *quantitatively* studying alloy properties which possess a delicate temperature dependence, such as short-range-order effects, mixing enthalpies or dynamic processes like the ageing of microstructures. This method is extended to alloy surfaces in order to investigate geometric relaxations as well as surface segregation, i.e. the enrichment of one component in the near-surface region. To establish a complementary, experimental view of the geometrical structure and chemical composition of surfaces, experimental low energy electron diffraction spectra are analysed by the use of a multiple-scattering theory (Pendry 1974 *Low Energy Electron Diffraction* (London: Academic), Van Hove and Tong 1979 *Surface Crystallography by LEED* (Berlin: Springer)) providing a test of our DFT predicted surface properties.

0953-8984/03/341429+72$30.00

Contents

1. Introduction

If A and B atoms are forced to crystallize on a common lattice, they may either order (AB bonds) or cluster (AA and BB bonds) depending on whether the occupation of neighbouring lattice sites by identical or different species is energetically favoured. From a fundamental point of view, the answer to the question of the physical behaviour of a binary alloy $A_{1-x}B_x$ as a function of concentration and temperature seems straightforward: an optimization of the Gibbs free energy $G(x, T)$ would immediately allow for the calculation of the alloy's equilibrium properties for any arbitrary concentration x and temperature T. The determination of $G(x, T)$, however, is not an easy task: we have to deal with a many-body problem and therefore, approximations have to be made which must be tested carefully with respect to their validity.

Generally, theoretical investigations about phase stability and alloy formation either use semi-empirical concepts [7–11] (e.g. based on macroscopic observations) or apply an electronic structure theory [2, 3]. At a first glance, the latter approach appears to be more general in the sense that the alloy is described by the rules of quantum mechanics. However, many alloy problems need the consideration of both huge configuration spaces and models containing thousands of atoms—a number far beyond the capacity of today's computers. As a consequence, most modern approaches to treat metal alloys and their surfaces compromise by simplifying the electronic Hamiltonian [12, 13], using empirical parameters [14–18] or by forbidding symmetry-lowering geometric relaxations [19–22]. In addition to the system size, theoretical studies must account for the alloys' specific phenomena which do not exist in pure-element crystals. Examples are surface segregation, describing the deviation from the alloy's bulk-like composition in the near-surface layers, or short-range order (SRO), defining to what extent a disordered phase of a real alloy differs from the ideal random alloy.

From the experimental point of view, tremendous efforts were made over the last decades to improve our knowledge of metal alloys. These activities led to extremely valuable experimental data collections [23–26] of alloy properties and phase diagrams. The large interest is fuelled by the technical relevance of metal alloys. Indeed, their applications range from lightweight cars and aircraft turbine blades to protective coatings in corrosive environments and magnetic devices. For example, it is believed that the use of so-called ‘heat-treatable’ alloys in the automotive industry will reduce the weight of cars by about 40% over the next ten years without losing today’s safety standards [27]. These (mainly) Mg- and Al-based alloys can be efficiently hardened by controlled heating and cooling processes [28]. An understanding of the microscopic processes behind this hardening effect is an important prerequisite for the technical application.

How can we treat and solve such problems connected to alloy formation, phase stability and geometric structure *without* any empirical parameters as input, but with an accuracy that allows the *quantitative* comparison with experimental data? First, a quantum-mechanical approach based on density functional theory (DFT) [2, 3] is used as the starting point for the alloy investigations. Those methods are called ‘first-principles methods’ in the sense that, for a given crystal lattice, no parameters are optimized by fitting experimental data. The access is, however, restricted to relatively small system sizes ($<$200 atoms). Moreover, the temperature dependence of alloy properties must be considered. This cannot be done by methods which only search the *positional* space such as molecular dynamics and not the *configurational* space being essential for modelling e.g. surface segregation. These two restrictions will be overcome by additionally applying concepts from statistical physics. On the one hand, cluster expansions (CE) [4] are used to treat systems ranging from a few up to a million atoms without giving up the accuracy of modern DFT calculations. On the other hand, Monte Carlo (MC) simulations permit us to study finite-temperature properties such as SRO phenomena or mixing enthalpies. The consideration of activation barriers for atomic exchange processes allows us to study the dynamics of microstructures using effective interactions retrieved from quantum-mechanical calculations. Regarding the surfaces of alloys, the theoretical predictions will be checked with experimental data resulting from the—again quantum-mechanical—evolution of low-energy electron diffraction (LEED) [29] intensities. Indeed, LEED probably is the most powerful and successful method in surface crystallography, with a geometric accuracy approaching the picometre level. This accuracy is reached by applying a multiple scattering theory [5, 6] in order to fit experimental intensity spectra with respect to their shape and peak positions. The combination of LEED, DFT, MC and CE can even be used to learn more about incommensurate systems.

The structure of the present work is as follows: our starting point is the fundamental question of how to quantify ordering, followed by a short description of the most relevant (semi-)empirical models. Next (section 3), the principal theoretical procedure and its extension to surface properties are introduced. Here, we will also see how DFT allows us to investigate strain effects in alloy systems. In section 4, the method will be applied to volume properties relevant for ordering, phase stability and electronic structure of metal alloys. In addition to the thermodynamic behaviour of different systems, we will also discuss ageing processes in quenched solid solutions leading to the formation of characteristic microstructures, the so-called precipitates. Finally, section 5 focuses on surface properties, addressing first segregation profiles and surface structures, next the SRO, and eventually going beyond the limits of CE: the description of an incoherent crystal problem.

2. How to describe ordering in metal alloys

The temperature–composition phase diagram of a binary solid state alloy, $A_{1-x}B_x$, may consist of homogeneous single-phase regions (such as ordered compounds A_mB_n) as well

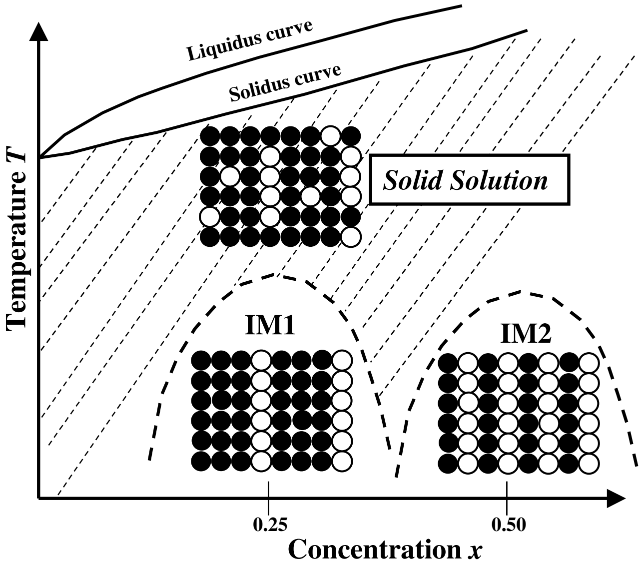

Figure 1. Portion of a schematic phase diagram of a binary alloy system $A_{1-x}B_x$. Beside two intermetallic compounds with ideal compositions $x = 0.25$ and 0.50, a third solid phase can be detected where no LRO exists. Such phases are called 'solid solutions'.

as heterogeneous, phase-coexistence regions [24]. A portion of such a phase diagram is schematically sketched in figure 1. The two full curves at higher temperatures are the liquidus and solidus curves which separate the region where the liquid and solid coexist from the liquid and solid phase, respectively. In the solid phase, two intermetallic compounds, i.e. long-range-ordered (LRO) phases, 'IM1' and 'IM2', exist at low temperatures, whilst the rest of the solid phase region represents a 'solid solution' which is stable over a large concentration and temperature regime. Although such solid solutions are still often treated as a substitutionally disordered alloy, where lattice sites are randomly occupied by A and B atoms, it had already been known for a long time that in reality more or less all solid solutions show some kind of SRO. The consideration of SRO is essential for a correct, quantitative description of the energetics and structure of this alloy phase. Therefore, the physical properties of solid solutions must be modelled by a *disordered* alloy which is not necessarily a *random* alloy.

If we wish to describe and understand the properties of different solid phases and their stability on theoretical grounds, we are confronted with a number of problems:

(i) Many theoretical models are restricted to some pair interactions which, in general, do not reproduce experimentally determined alloy properties quantitatively. Instead, many-body interactions must be considered whose determination can be rather complex.
(ii) Most intermetallic compounds undergo atomic relaxations in their unit cell (consistent with the symmetry of the compound). Neglecting such relaxations can change the hierarchy of stability between different intermetallic phases and even lead to a wrong ground state.
(iii) The quantitative prediction of SRO phenomena often requires models with giant unit cells. Model systems containing up to 10^5 atoms may be demanded, i.e. much more than the about 200 metal atoms treatable by today's computers within the framework of quantum mechanics.
(iv) The temperature dependence of ordering phenomena must not be neglected. However, in general, electronic structure theories neglect configurational entropy.

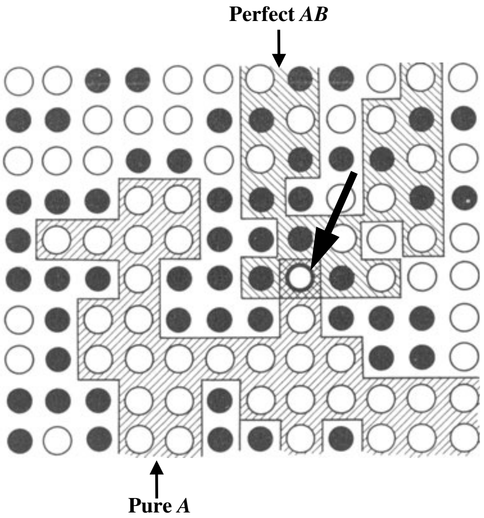

Figure 2. The dilemma in describing ordering (taken from [30]): does the atom marked by an arrow belong to ‘a cluster of pure A atoms’, or to a ‘region of perfect AB order’?

At a first glance, this looks like a totally hopeless dilemma, e.g. we did not yet introduce a measure of *how* to quantify ordering, let alone a model of how to predict it. Ziman [30] nicely described the difficulty in handling ordered zones in a disordered matrix by the help of figure 2: for the given configuration, we cannot decide if the atom marked by an arrow belongs to a ‘cluster of pure A atoms’ or to a ‘region of perfect AB order’. He demonstrated by applying percolation theory that almost every A atom belongs to an infinite cluster of A atoms. Paradoxically, if we are looking for ordered domains (figure 2), then almost every atom belongs to an infinite domain with perfect AB ordering. Help comes by introducing statistical concepts [30–32]: for a system consisting of N sites each surrounded by M neighbours, the probability of a bond being of AB type is given by

$$P_{\mathrm{AB}} = \lim_{N\to\infty}\left(\frac{N_{\mathrm{AB}}}{\frac{1}{2}MN}\right) \tag{1}$$

with N_{AB} being the total number of AB-type bonds. The denominator gives the total number of bonds in the system. We can now easily introduce a *nearest-neighbour correlation parameter* Γ_{AB}. Assuming that each site of the system is independently occupied by an A or B atom with probability x_{A} or x_{B} ($x_{\mathrm{A}} + x_{\mathrm{B}} = 1$), P_{AB} would be $2x_{\mathrm{A}}x_{\mathrm{B}}$. Then, Γ_{AB} is defined by the difference

$$\Gamma_{\mathrm{AB}} = \tfrac{1}{2}P_{\mathrm{AB}} - x_{\mathrm{A}}x_{\mathrm{B}}. \tag{2}$$

Dividing Γ_{AB} by $-x_{\mathrm{A}}x_{\mathrm{B}}$ leads to the well-known *Warren–Cowley SRO parameter* [33]

$$\alpha_j = 1 - \frac{P^j_{\mathrm{AB}}}{2x_{\mathrm{A}}x_{\mathrm{B}}}. \tag{3}$$

Here, α_j is already extended to arbitrary neighbour distances j. The sign of α_j indicates whether atoms in a given distance j prefer AB ordering ($\alpha_j < 0$) or clustering ($\alpha_j > 0$). The SRO parameters are normalized such that $-1 \leqslant \alpha_j \leqslant +1$; $\alpha_j = 0$ for all j stands for a perfect random alloy, i.e. an alloy without any atomic correlations. Since α_j can be determined from diffuse x-ray and neutron diffraction experiments [34–36], a *quantitative* comparison between calculation and measurement is possible.

In principle, the knowledge of the Gibbs free energy

$$G = H - TS \tag{4}$$

of the alloy system as a function of concentration x, with H being the enthalpy, T the temperature and S the entropy, gives access to all equilibrium properties of the system. However, only the enthalpy H is directly related to the internal 'crystal energy', which is determined by the bond strength. Putting temperature effects aside for the moment, two different concepts can be used to determine H: (i) (semi-)empirical models, which are largely based on macroscopic observations, or (ii) an electronic structure theory based on quantum mechanics.

Starting with the former, the most famous empirical model for predicting solid solution formation is probably the set of Hume-Rothery [7, 37] rules. Hume-Rothery studied solid solutions of binary systems in the early 1930s and he proposed three factors controlling the extent of solid solubility, namely atomic size, electronegativity and the number of valence electrons of the two elements. His pioneering work still plays an important role in today's understanding of solid solutions. Another famous, semi-empirical access to alloy formation is Miedema's atomic cell model [8, 38, 39]. It assumes that processes between atomic Wigner–Seitz cells of A and B atoms correspond to those which happen when a macroscopic piece of metal A is put into contact with a piece of metal B. This is called the *macroscopic atom picture*. As the boundary conditions have changed at the interface area between the A and B cells, the atomic volumes of the cells will change, too. Miedema and co-workers assumed [8, 38, 39] that this change in boundary conditions is responsible for the formation enthalpy, ΔH_f, of an alloy, whereby the amount of ΔH_f is proportional to the size of the contact area between dissimilar atomic cells. The model is astonishingly successful, especially with respect to the sign of formation enthalpies [40]. Although the model fails for some groups of alloys, its practical usefulness is accepted, especially in metallurgy.

Many attempts have been made to find a *single* characteristic property of binary alloys that would automatically determine whether, for a given concentration, two elements form an intermetallic compound or phase-separate. From the many efforts to sort compounds with respect to their structure, the best known collection is due to Pettifor, in whose structure maps [9, 41] each of the two elements in a binary compound gets a 'coordinate value', placing it in a given structure domain of an empirical structure-sorting map. This phenomenological coordinate, the so-called Mendeleev number [42], originates from the electronegativity of each element. Over the years, a lot of studies have been made to improve the validity of structure maps by the help of microscopic atomic coordinates. Probably the most successful examples are Zunger's orbital radii method [10] which uses the difference between pseudopotential (PP) radii sums (constructed for first-principles calculations) as the 'coordinate value' (the concept of PPs will be explained in section 2.1) and Villars' [11] coordinate plots combining macroscopic with microscopic coordinates.

In this review the bulk and surface properties of metal alloys are studied *without* any experimental parameters as input. As already mentioned in the introduction, we use DFT [2, 3] as the starting point for our studies. Although DFT permits one to calculate alloy properties with an accuracy that often allows for a quantitative comparison with experimental data, it is usually limited to a small subset of the configuration space. The geometric relaxation of unit cells consisting of more than 100 atoms already becomes extremely difficult, and even impossible for some cases. So, compared to the 2^N configurations of a binary system containing N atoms, we are restricted to a very small part of the parameter space. Normally, a set of 'intuitive structures' is chosen and that with the minimal energy is postulated as the ground-state configuration. This, however, fails to allow for surprises: only one of the chosen

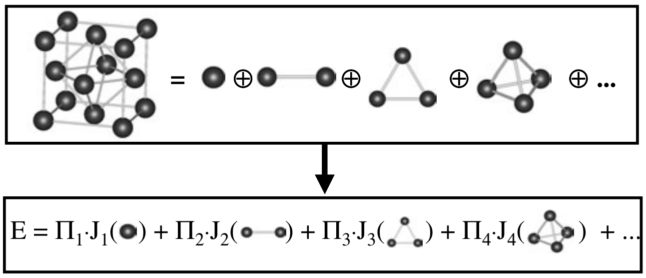

Figure 3. The concept of CE: the crystal is separated into characteristic figures (shown here for the fcc lattice). The energy of any configuration can then be written as a linear combination of the characteristic energies J_f of the figures.

input structures can result as the ground state. In principle, there are two possibilities to circumvent this problem:

(i) A simplified electronic Hamiltonian combined with perturbation theory is used [12], or the quantum-mechanical total energy is replaced by phenomenological effective pair potentials [13]. However, the precision of these approaches is very limited, and so they only work for specialized cases.
(ii) The accuracy of DFT is extended to huge configuration spaces by combining DFT with concepts from statistical mechanics.

The basic idea by Sanchez *et al* [4] is called CE and outlined in figure 3: for a given underlying lattice, the crystal structure is divided into characteristic figures such as pairs, triangles, etc. Then, the energy of *any* configuration σ on this lattice can be uniquely written [4] as a linear combination of the characteristic energies J of each individual figure. In practice, the only error we make is that the sum must be truncated at some point. The Π_f's in figure 3 are structure-dependent factors and will be discussed in detail in section 3.2.

The CE ansatz allows us to treat physical problems ranging from a few up to a million atoms without giving up the accuracy of modern DFT calculations. However, this concept still needs to be extended to finite temperatures. This problem can be solved by using $E(\sigma)$ in figure 3 in MC simulations. We can even extend the field of application to non-equilibrium processes by switching from thermodynamic MC to kinetic MC [43]. For this, activation barriers for exchange processes between neighbour atoms have to be considered and the number of possible exchange processes between atoms must be restricted to small distances. Indeed, the combination of a CE with MC allows us to treat the energetic properties of large systems and their temperature dependence with the accuracy of quantum-mechanical calculations [44]. This option is, for example, essential to calculate thermodynamic properties of precipitates[1] in metal alloys [45, 46] and their time evolution [47].

So far, we have ignored the fact that every solid is finite and therefore has a surface. Including surface effects in our description of binary metal alloys is an important prerequisite to understand processes which depend on an interaction between the bulk and the surface. The most important example is probably the interplay between bulk diffusion (controlled by kinetics) and surface segregation (controlled by thermodynamics). Surface segregation describes the deviation of the chemical composition in the near-surface layers, compared to the bulk, and plays a technologically important role, as it may strongly influence physical and

[1] Precipitates are characteristic microstructures which may consist of many thousands of atoms, as discussed in sections 4.3 and 4.4.

chemical processes such as catalysis, crystal growth or corrosion. For these reasons, it is not surprising that, for many years, efforts have been undertaken to understand surface segregation by (semi-)empirical models [48, 49] as successfully applied to bulk properties. Modern approaches for describing surface segregation use either empirical potentials like the embedded atom method [15, 16] or the coherent potential approximation (CPA) [21, 22] which—at least in practice—does not consider symmetry-lowering relaxations. So, the latter only works for systems with a very small misfit between the lattice parameters of the constituents. Yet, the spacing between the near-surface layers can be rather different from the bulk value [50]. Such relaxations are often strongly correlated to the segregation profile of the surface. In other words, surface segregation is not independent of geometric properties.

Furthermore, our model must account for the broken symmetry at the surface. This reduces the conserved point symmetry operations of the bulk (e.g. the 48 operations for cubic fcc or bcc lattices) to a much smaller, orientation-dependent number. Consequently, the symmetric degeneration of CE figures decreases and therefore the number of geometrically different figures (figure 3) in the CE increases. This concept was, for example, recently applied to study surface segregation in Ni–Al alloys for $T = 0$ K [51].

The principles of quantum mechanics do not only allow us to calculate alloy surface properties from first principles, but also help test the correctness of the prediction by analysing experimental data. The method of choice is LEED [29], probably the most powerful and successful method in surface crystallography, with a geometric accuracy approaching the picometre level. Since there exists a number of excellent review articles [52–54], only the principal concepts will be described here briefly. The power of LEED comes from the high elastic electron scattering cross section of atoms, when the incident electrons have rather low energies (20–600 eV $\leftrightarrow \lambda \sim 0.5$–2.5 Å). This leads to multiple scattering and so to many interference peaks which carry information on the surface structure and allow its retrieval with high accuracy. The diffraction pattern, which can be observed by a suitable detector, reflects the translation symmetry of the surface structure. In order to obtain the individual atomic positions, the intensity of different diffraction orders must be recorded as a function of energy. Due to the multiple-scattering processes, a full-dynamical rather than a kinematic scattering theory must be applied for the intensity analysis [5, 6]. The calculated spectra of a physically meaningful surface model are compared to the experimental spectra using a numerical 'reliability factor' [55, 56]. The model has to be modified until experimental and theoretical spectra agree. Over the last two decades, the introduction of perturbation methods [57, 58] opened up the possibility of applying LEED to, for example, complex alloy surfaces [59], metal films [60] and metal–metal interfaces near the surface [61, 62]. The code used in this work, called 'TensErLEED', was developed in Erlangen by Blum and Heinz [63]. By combining scattering theory, perturbation methods and a frustrated simulated annealing procedure [64] 'TensErLEED' allows us to deal with huge parameter spaces. Since LEED $I(E)$ spectra are not only sensitive to the geometric position of atoms, but also to the chemical composition [65] as well as vibrational amplitudes [66], the technique permits a detailed characterization of alloy surfaces as well as correlations between surface segregation and ordering [67].

3. Theoretical methods and procedures

3.1. Density functional and elasticity theory: tools for predicting alloy properties

First-principles calculations based on the density-functional approach have been very useful in understanding the stability of simple single-phased materials. This includes calculations of perfectly ordered compounds [68] as well as perfectly random alloys [69, 70]. Since there exist a number of excellent review articles [71, 72] and books [73–75] about DFT, only some general remarks will be given here. DFT is based on the Hohenberg–Kohn theorem [2] stating that the energy of a system of interacting electrons in an external potential depends only on the ground-state electronic density. In our case, namely the investigation of solid structures, the external potential is the Coulomb potential caused by the nuclei in a solid. The ground-state density can, in principle, be calculated from a variation ansatz, i.e. without any Schrödinger equation. However, for treating real problems the variational approach is impractical. Help came in 1965 from Kohn and Sham [3] who showed that the density wanted is given by the self-consistent solution of a set of single-particle equations, called Kohn–Sham equations:

$$\left[-\frac{\hbar^2}{2m}\nabla^2 + V_{\mathrm{e-nuc}}(\boldsymbol{r}) + V_{\mathrm{H}}(\boldsymbol{r}) + V_{\mathrm{XC}}(\boldsymbol{r})\right]\Psi_i(\boldsymbol{r}) = \epsilon_i\Psi_i(\boldsymbol{r}). \tag{5}$$

In this Schrödinger-like equation, the first term on the left side represents the kinetic energy operator, $V_{\mathrm{e-nuc}}$ is the Coulomb potential due to the nuclei, V_{H} is the Hartree potential and V_{XC} is the exchange-correlation potential. The latter comes from replacing the kinetic energy of interacting particles by that of non-interacting particles (which can be treated exactly) plus a term containing all correlation and exchange effects (which is unknown, but small compared to the other energy contributions). Well-known approximations for V_{XC} are the local density approximation (LDA) [76, 77] and the generalized gradient approximation (GGA) [78]. In LDA, the energy density of the inhomogeneous system is approximated by the density of the *homogeneous* electron gas which possesses exactly the same density as the actual *inhomogeneous* system. Although this sounds like a very rough approximation, especially for systems with strongly varying density, it works astonishing well for a huge number of problems. In GGA, additionally the gradient of the density is considered which can be important for systems where $n(\boldsymbol{r})$ changes dramatically with $\boldsymbol{r}$.

In practice, we can distinguish between more or less two different types of strategies: methods using complex, but efficient, basis sets for the wavefunctions, such as the linearized augmented plane-wave method (LAPW), and methods based on so-called PP using plane waves as the basis set (for a survey see, for example, the book by Singh [79]). The concept of PP is roughly that most physical properties of a solid are determined by the valence electron structure. Then, the number of plane waves necessary to describe the system can be tremendously decreased by replacing core electrons and ionic potential by a PP which is energetically much weaker and corresponds to a node-free wavefunction. Thereby, the PP has to fulfil the conditions that

(a) the scattering properties of the elements are conserved and
(b) outside the core region PP and the pseudo-wavefunction are identical to the corresponding full potential and wavefunction.

Until some years ago, it was a very delicate task to study transition metals (TM) by ‘classical’, norm-conserving PP [80, 81]. With the development of ultrasoft PP [82, 83] and, more recently, so-called PAW potentials (‘projector augmented wave’) [84, 85] concepts from LAPW entered into PP codes and allow for an accurate and fast treatment of practically all metal systems by a plane-wave basis set.

Most calculations in this work use PP codes, namely parallel total energy (PEtot) [86] and the Vienna *ab initio* simulation package (VASP) [87]. The latter was applied for all surface calculations in this work. The LAPW method [88] was used to study the system Ag–Pd (section 4.1) and for comparison with PP results.

While calculated total energies do not allow for a direct comparison with experimental data, because the absolute energy values depend on the applied approach (e.g. LAPW or PP

Table 1. Experimental [24] and theoretical formation enthalpies and lattice parameters for the ordered B2 phase of FeAl, CoAl and NiAl.

System		ΔH_f (eV/atom)	Lattice parameter (Å)
FeAl, B2	Exp.	−0.26	2.862
FeAl, B2	DFT	−0.30	2.879
CoAl, B2	Exp.	−0.56	2.862
CoAl, B2	DFT	−0.57	2.855
NiAl, B2	Exp.	−0.64	2.887
NiAl, B2	DFT	−0.66	2.898

ansatz), differences *between* them should not depend on the selected code within statistical errors and errors due to the chosen approximations (e.g. LDA or GGA). One of the most relevant physical properties of alloys, being essential for all our further studies, is the *formation enthalpy*, $\Delta H_f(\sigma)$, per atom of an alloy structure σ. It is defined as the energy gain or loss per atom with respect to the bulk constituents at their equilibrium lattice constants. For an intermetallic compound $\mathrm{A}_m\mathrm{B}_n$ (consisting of m A and n B atoms per unit cell) ΔH_f is given by

$$\Delta H_f(\mathrm{A}_m\mathrm{B}_n) = \frac{1}{m+n}[E^{tot}(\mathrm{A}_m\mathrm{B}_n) - m \cdot E^{tot}_{\mathrm{A}}(a_{\mathrm{A}}) - n \cdot E^{tot}_{\mathrm{B}}(a_{\mathrm{B}})]. \tag{6}$$

Here, a_{A} and a_{B} are the equilibrium lattice constants of the elements A and B in their bulk, and $E^{tot}_{\mathrm{A}}(a_{\mathrm{A}})$ and $E^{tot}_{\mathrm{B}}(a_{\mathrm{B}})$ are the respective total energies. Since all total energy values are negative, a positive sign of ΔH_f stands for phase separation, while a negative sign of ΔH_f means ordering. The total energy of the compound $\mathrm{A}_m\mathrm{B}_n$, $E^{tot}(\mathrm{A}_m\mathrm{B}_n)$, must correspond to the *geometrically fully relaxed configuration*, i.e. the structure has to be optimized (consistent with the symmetry of the structure) with respect to the aspect ratio of unit cell vectors, cell internal atomic displacements and the volume of the unit cell. As is well known [89–91], the consideration of relaxations is essential for a quantitatively correct calculation of energetic properties such as, for example, phase stability. As an example, table 1 compares the result of GGA calculations for formation enthalpy and lattice parameters of the B2 structure (CsCl structure) of Co–Al, Ni–Al and Fe–Al with experimental data [24]. Within theoretical and experimental uncertainties the values agree very well. Two points should be emphasized:

(i) All three enthalpies are negative, meaning that ordering is preferred over phase separation.
(ii) The energetic hierarchy in our calculations agrees perfectly with experiment. The B2 structure is most stable in Ni–Al and least stable in Fe–Al.

This result is even more important than the absolute values of ΔH_f, because it demonstrates the possibility of studying alloy problems which demand a comparison of the phase stability *between* different systems by DFT calculations. It should be mentioned that the concept of equation (6) also holds for *disordered* alloy structures $\mathrm{A}_{1-x}\mathrm{B}_x$. Then, $\Delta H_f(\sigma)$ is called the *mixing enthalpy* per atom of σ and is given by

$$\Delta H_{mix}(\sigma) = \frac{1}{N}E^{tot}(A_{1-x}B_x, \sigma) - (1-x)E^{tot}_{\mathrm{A}}(a_{\mathrm{A}}) - xE^{tot}_{\mathrm{B}}(a_{\mathrm{B}}) \tag{7}$$

with N being the total number of atoms in the disordered alloy.

In order to understand the trends in formation enthalpies, one sometimes wishes to decompose $\Delta H_f(\sigma)$ in characteristic energy portions as strain energy, containing information about the elastic properties of the alloy, and chemical energy, containing information about the strength of the different interaction energies between atoms. In section 4.3 we will see how this idea permits one to understand the size versus shape relation of characteristic microstructures in metal alloys. Indeed, combining DFT with elasticity theory can help to calculate the strain behaviour of metal alloys. Since strain is determined by the mechanical behaviour of the system, we separate the two components by creating an interface in a well-defined orientation between A and B atoms and demand that the whole system act as a pseudomorphic, epitaxial system, i.e. there are no dislocations at the interface. The idea to compare a binary alloy with an epitaxial film/substrate system allows us to specify two types of quantities [92]:

(i) The *hydrostatic deformation energy* $\Delta E_A^{\text{hydro}}(a)$ being the energy required to hydrostatically deform the solid element A to the lattice constant a of the alloy.

(ii) The *epitaxial strain energy* $\Delta E_A^{\text{epi}}(a, \hat{G})$, representing the energy of the elemental solid A epitaxially (or, biaxially) deformed to the 'substrate' lattice constant a in the two directions orthogonal to $\hat{G}$ and *relaxed* along $\hat{G}$.

The ratio of these two energies defines the *epitaxial softening function* [92, 93]

$$q(a, \hat{G}) = \frac{\Delta E_A^{\text{epi}}(a, \hat{G})}{\Delta E_A^{\text{hydro}}(a)}. \tag{8}$$

Since it is always easier to deform a material epitaxially (biaxially) than hydrostatically (triaxially), $q \leqslant 1$. Small values of $q(a, \hat{G})$ indicate elastically soft directions $\hat{G}$. As an example, figure 4(b) shows calculated softening functions, $q(a, \hat{G})$, for the fcc elements Al and Cu along the crystal directions indicated in figure 4(a). Obviously, the crystallographic order of elastic softness can change as a function of the lattice parameter. For example, an only 2% compression of Al (figure 4(b)) is softer along (110) than along (100), while at equilibrium the opposite is true. This clearly indicates that, for a description of strain effects in metals, not only the direction dependence of strain (*anisotropic* strain effects), but also the dependence of strain on the lattice parameter (*anharmonic* strain effects) must be taken into account [95, 96]. In the harmonic elasticity theory, q depends only on the direction $\hat{G}$, but *not* on the substrate lattice constant a [90, 92, 97]:

$$q_{harm}(\hat{G}) = 1 - \frac{B}{C_{11} + \Delta\gamma_{harm}(\hat{G})} \tag{9}$$

with bulk modulus $B = \frac{1}{3}(C_{11} + 2C_{12})$ and anisotropy parameter $\Delta = C_{44} - \frac{1}{2}(C_{11} - C_{12})$. The harmonic constants C_{11}, C_{12} and C_{44} can be easily calculated from first-principles calculations [92] and consequently, Δ and B, too. γ_{harm} is a geometric function of the spherical angles Θ (polar angle) and Φ (azimuth angle) formed by $\hat{G}$:

$$\begin{aligned}\gamma_{harm}(\Phi, \Theta) &= \sin^2(2\Theta) + \sin^4(\Theta)\sin^2(2\Phi) \qquad (10)\\ &= \frac{4}{3}\sqrt{4\pi}\left[K_0(\Phi, \Theta) - \frac{2}{\sqrt{21}}K_4(\Phi, \Theta)\right].\end{aligned}$$

Here, K_l is the cubic harmonic of angular moment l. If anharmonic effects become important as in metal alloys, q additionally depends on the lattice parameter a:

$$\gamma(a, \hat{G}) = \gamma_{harm}(\hat{G}) + \sum_{l=0}^{l_{\max}} b_l(a)K_l(\hat{G}). \tag{11}$$

This equation now also includes higher-order cubic harmonics as necessary to go beyond the harmonic approximation (more details are given by Ozolins *et al* [95]). Then, equation (9) becomes

$$q(a, \hat{G}) = 1 - \frac{B}{C_{11} + \Delta\gamma(a, \hat{G})}. \tag{12}$$

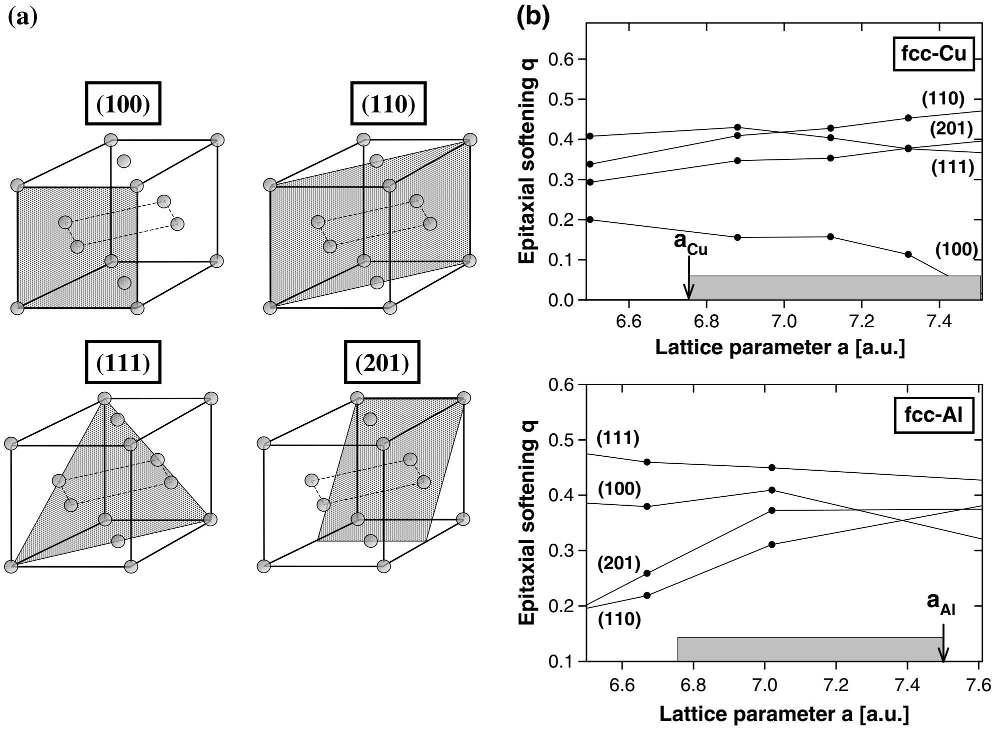

Figure 4. (a) Low index crystal orientations of the fcc lattice indicated by hatched areas. (b) Epitaxial softening function $q(a, \hat{G})$, equation (8), for Cu and Al calculated via LDA. The shaded areas mark the lattice parameter range between the two components of the corresponding alloy. Arrows denote the position of the equilibrium lattice constant a_{eq} of each element. The lines are drawn merely to guide the eye [94].

With $q(a, \hat{G})$ resulting from DFT calculations as displayed in figure 4(b), the quantity $\gamma(a, \hat{G})$ can be taken from equation (12) and, in turn, the coefficients $b_l(a)$ results via equation (11). The determination of $b_l(a)$ permits one to generalize calculated epitaxial energies, $\Delta E_A^{\mathrm{epi}}(a, \hat{G})$ for a discrete set of directions to *arbitrary* directions $\hat{G}$.

We will apply it to parametrize the equilibrium *constituent* (or *coherency*) *strain energy* $\Delta E_{\mathrm{CS}}^{\mathrm{eq}}(x, \hat{G})$ which is defined as the strain energy required to maintain coherence between a 'piece' of material A and a 'piece' of material B along an interface with orientation $\hat{G}$. This structure represents a so-called *superlattice* (SL) $\mathrm{A}_n\mathrm{B}_n$ along a certain direction $\hat{G}$ with $n \to \infty$. In practice, the calculated elemental epitaxial energies are used to determine the constituent strain energy that is determined by the equilibrium value of the composition-weighted sum of the epitaxial energies of A and B:

$$\Delta E_{\mathrm{CS}}^{\mathrm{eq}}(x, \hat{G}) = \min_{a_p}[x \Delta E_{\mathrm{A}}^{\mathrm{epi}}(a_p, \hat{G}) + (1 - x) \Delta E_{\mathrm{B}}^{\mathrm{epi}}(a_p, \hat{G})] \tag{13}$$

where $a_p(x)$ is the lattice constant that minimizes $\Delta E_{\mathrm{CS}}^{\mathrm{eq}}$ at each x. The constituent strain can be illustrated by a three-dimensional parametrization in terms of a sum of cubic harmonics, as shown in figure 5 for three different Al concentrations of the system Al–Cu. Here, the distance from the surface to the centre of the cube represents the strain energy in this crystallographic direction. For $\mathrm{Al}_{0.1}\mathrm{Cu}_{0.9}$, we see that this distance is maximal along the body diagonal (marked by a bold circle), i.e. the crystallographic [111] direction, whilst the distance is shortest along

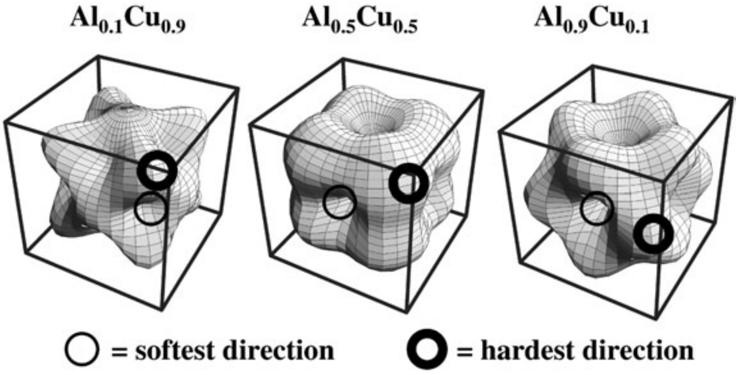

Figure 5. Parametric three-dimensional presentation of the constituent strain $\Delta E_{\mathrm{CS}}^{\mathrm{eq}}$, equation (13), of Al–Cu for compositions of 10, 50 and 90% Al. The distance from the surface to the centre of the cube represents the amount of strain energy.

the square face diagonal (marked by a thin circle), i.e. the [110] direction. With increasing Al composition the situation changes: $Al_{0.5}Cu_{0.5}$ owns the smallest constituent strain for [100], while [111] is still the hardest direction. For 90% Al, the figure has a 'depression' in the very soft [100] direction, but a protrusion in the hard [111] direction. As we will see next, the concept of constituent strain is very important to describe morphological properties of alloys.

3.2. Bridging length scales and treating finite temperatures: cluster expansion and Monte Carlo method

As discussed in section 2, the idea of CE [4] is to express the atomically relaxed energy, $E(\sigma)$, of arbitrary lattice configurations σ on a given, underlying lattice as a linear sum of energies characteristic of geometric figures, such as biatoms, triatoms, etc (see figure 3). To realize this idea in practice we transform the 'alloy problem' to an Ising model. Each atom i of an $A_{1-x}B_x$ alloy is assigned to a spin value $S_i = -1$, if i is an A atom, and to $S_i = +1$, if i is a B atom. Then, the energy of each configuration can be expressed by an Ising expansion:

$$E(\sigma) = J_0 + \sum_i J_i S_i(\sigma) + \sum_{j<i} J_{ij} S_i(\sigma) S_j(\sigma) + \sum_{k<j<i} J_{ijk} S_i(\sigma) S_j(\sigma) S_k(\sigma) + \cdots . \qquad (14)$$

The first two terms on the right define the energy of the random alloy (with zero mutual interactions), the third term contains all pair interactions, the fourth all three-body interactions, etc. This equation can be brought to a compact form by introducing a correlation function $\bar{\Pi}_F$ for each class of symmetry-equivalent figures F [44]:

$$\bar{\Pi}_F(\sigma) = \frac{1}{ND_F} \sum_f S_{i_1}(\sigma) S_{i_2}(\sigma) \cdots S_{i_m}(\sigma). \qquad (15)$$

Here, D_F gives the number of figures of class F per site. The index f runs over the ND_F figures in class F and m denotes the number of sites of figure f. Then, equation (14) becomes [90]

$$E(\sigma) = N \sum_F D_F \bar{\Pi}_F(\sigma) J_F. \qquad (16)$$

This 'rewriting' of equation (14), however, does not help to answer the question of *how* the interactions J_F of the system can be determined. As discussed by Zunger [44], one can follow three different concepts to solve this problem:

(i) An empirical fit of the interactions to experimentally determined features of the corresponding alloy phase diagram is used [17, 18]. However, this access is limited to a small number of interactions, while most alloy systems usually demand the consideration of more than about 20 pair and 10 multi-body interactions for a quantitative description.
(ii) Ordered structures are treated as a perturbation of the random alloy modelled by the virtual crystal approximation (VCA) [98] or the CPA [19, 20, 99–101]. Although this access provides first-principles results (i.e. without the use of fitting procedures), it is limited to alloys consisting of similar constituents in the sense that first-order perturbation theory is valid, and is only practical for calculating pair interactions.
(iii) The direct inversion method by Conolly and Williams [102] is applied.

For a set (about 15–40) of N_σ mostly simple ordered compounds with typically no more than 2–16 basis atoms the energies E_{DFT} of the geometrically relaxed structures are calculated via DFT. Then, the N_σ energies are used to construct N_F interactions J_F by solving

$$\sum^{N_\sigma} \omega_\sigma \left| E_{\mathrm{DFT}}(\sigma) - N \sum^{N_F} D_F J_F \bar{\Pi}_F(\sigma) \right|^2 = \text{Minimum} \qquad (17)$$

with respect to the N_F values of J_F. Here, ω_σ are weight factors which can be chosen, for example, as determined by the number of conserved point group operations of configuration σ in the way that the highest weight is attributed to the least symmetric configurations, since they should contain more distinct environments than the high-symmetry configurations. Naturally, $N_F \leqslant N_\sigma$ in order to prohibit an overestimation of the interactions. The finally resulting set of J_F's has to pass a number of tests before it can be applied to physical problems [103]:

(i) *Stability of interactions:* a certain interaction is only negligible for the CE fit if its consideration or neglect does not change the modulus and sign of *all* other interactions used. Otherwise, this interaction is essential for the stability of the CE. The same argument holds for adding or removing the energy, E_{DFT}, of one structure σ to the set of energies used to construct the effective interactions J_F. Again, the pair and multi-body interactions should not change more than a few millielectronvolts.
(ii) *Energy prediction of geometrically relaxed structures:* the interactions fitted by the minimization must be able to predict the energy, $E(\sigma)$, of a structure σ which was *not* used for the fit. This can be easily checked by calculating the DFT energies of some arbitrary ordered compounds and comparing them with those obtained from the CE. Furthermore, a certain input structure σ is essential for the CE construction, if its removing leads to a drastic increase of the minimum on the right side of equation (17) for *any* of the remaining $N_\sigma - 1$ structures.

Indeed, a reasonable selection of the input structures is a delicate task and needs some experience. One efficient tool to find structures with important ‘structure information’ for the determination of the interactions is a ground-state search [104, 105] in the early stage of the construction. For a ‘starting set’ of about 20 DFT energies of arbitrary input structures, a CE fit is performed. The resulting interactions are then used to predict the energy of *all possible structures* with, for example, up to 16 atoms per unit cell (the latter is indeed a very reasonable restriction, since most known stable structures in binary metal alloys own clearly less than 16 atoms per unit cell). Such an analysis based on equation (16) takes only a few hours on a high-performance PC. Afterwards, the corresponding CE formation enthalpies, ΔH_f, of all structures are plotted as a function of composition and a ground-state line is constructed. This is schematically shown in figure 6: An individual structure σ only contributes to the ground-state line if the linear energy average between the stable structures at the next highest

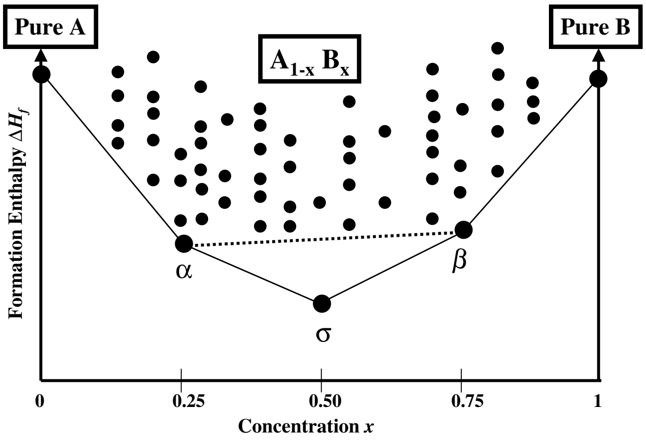

Figure 6. Schematic ground-state diagram of a binary alloy $A_{1-x}B_x$. The ground-state line was constructed from 60 energies of relaxed structures (given by dots) by use of equation (18). Besides the pure elemental crystal the ground-state line is formed by three structures α, σ and β for concentrations $x = 0.25, 0.50$ and 0.75, respectively. If σ would lie energetically above the broken tie line between α and β, a mixture of α and β would be more stable than σ.

and lowest concentration is energetically less favourable than the formation enthalpy of σ. More precisely, for three structures α, σ and β with $x(\alpha) < x(\sigma) < x(\beta)$ which are the lowest in energy for their individual concentrations, the structure σ has to fulfil the condition

$$\Delta H_f(\sigma) < \frac{x(\sigma) - x(\beta)}{x(\alpha) - x(\beta)}\Delta H_f(\alpha) + \frac{x(\sigma) - x(\alpha)}{x(\beta) - x(\alpha)}\Delta H_f(\beta) \tag{18}$$

in order to be the ground state at $x(\sigma)$. If equation (18) holds, a mixture of the phases α and β would be higher in energy than structure σ. With the ground-state line constructed, we check for all structures which lie on or very close to it (so-called 'excited states') whether they were already considered as input structures for the CE. If not, their DFT energy is calculated and added to the input-structure set, while input structures with ΔH values far above the ground-state line are removed from the original input structure list. The procedure is repeated until the ground-state line becomes stable. Examples for ground-state diagrams will be discussed in section 4.1.

There remains, however, a very critical point: as shown by Laks *et al* [90], any CE in real space *fails* to predict the energy of long periodic coherent SLs. For a given SL A_nB_n, equation (16) predicts a formation enthalpy $\Delta H_f = 0$ as $n \to \infty$. This indeed is an intrinsic fault of any finite CE and is easy to understand: if we consider an A atom of an A_nB_n SL 'far' away from the A/B interface so that all figures f connect the A atom exclusively to other A atoms, then the finite CE interprets the A atom as a bulk crystal atom and consequently $\Delta H_f = 0$. However, as discussed in section 3.1, the formation enthalpy of an infinite SL should be defined as the equilibrium constituent strain energy, because in the limit $n \to \infty$ the SL formation enthalpy depends only on its strained constituents, and not on the interface properties. The problem can be solved [44, 90] by transforming a group of interactions to the reciprocal space and adding the constituent strain term explicitly. This is easiest to do for the pair interactions. For this, we introduce the Fourier transform of real-space pair interactions, $J_{pair}(\boldsymbol{k})$, and the structure factor $S(\boldsymbol{k}, \sigma)$:

$$J_{pair}(\boldsymbol{k}) = \sum_j J_{pair}(\boldsymbol{R}_i - \boldsymbol{R}_j)\exp(-\mathrm{i}\boldsymbol{k}\boldsymbol{R}_j) \tag{19}$$

$$S(\boldsymbol{k},\sigma) = \sum_j S_j \exp(-\mathrm{i}\boldsymbol{k}\boldsymbol{R}_j). \tag{20}$$

Then the formation enthalpies for any arbitrary atomically relaxed configuration σ are expressed by [44]

$$\Delta H_{\mathrm{CE}}(\sigma) = \sum_{\boldsymbol{k}} J_{pair}(\boldsymbol{k})|S(\boldsymbol{k},\sigma)|^2 + \sum_F D_F J_F \bar{\Pi}_F(\sigma) + \Delta E_{\mathrm{CS}}(\sigma). \tag{21}$$

This solution was introduced by Zunger and co-workers [44, 90] and is called mixed-space cluster expansion (MSCE). The first term includes all pair figures in $\boldsymbol{k}$ space. The second term represents many-body interactions and runs over symmetry inequivalent clusters consisting of three or more lattice sites. It also includes J_0 and J_1 from equation (14). D_F again stands for the number of equivalent clusters per lattice site and $\bar{\Pi}_F(\sigma)$ are the structure-dependent geometrical coefficients given by equation (15). The last term represents the constituent strain energy of the structure σ, $\Delta E_{CS}(\sigma)$, and can be calculated by expanding the equilibrium constituent strain energy (equation (13)), $\Delta E^{\mathrm{eq}}_{\mathrm{CS}}(x,\hat{k})$, as [90, 106]

$$\Delta E_{\mathrm{CS}}(\sigma) = \sum_{\boldsymbol{k}} J_{\mathrm{CS}}(x,\hat{k})|S(\boldsymbol{k},\sigma)|^2 \tag{22}$$

with

$$J_{\mathrm{CS}}(x,\hat{k}) = \frac{\Delta E^{\mathrm{eq}}_{\mathrm{CS}}(x,\hat{k})}{4x(1-x)}. \tag{23}$$

Now, J_{CS} contains the correct long-periodic SL limit, namely the constituent strain energy[2].

Analogous to the real-space expansion, equation (16), we need the formation enthalpies $\Delta H_f(\mathrm{A}_m\mathrm{B}_n)$ of ordered compounds as input to determine the sets of coefficients $\{J_{\mathrm{pair}}(\boldsymbol{k})\}$, and $\{J_f\}$ of the CE. The pair and multi-body interactions results by the fit to the N_σ formation enthalpies $\{\Delta H_f\}$, minimizing the root mean square (rms) error [44]:

$$\Delta^2_{\mathrm{rms}} = \frac{1}{N_\sigma}\sum_\sigma w_\sigma[\Delta H_{\mathrm{CE}}(\sigma) - \Delta H_{\mathrm{LDA}}(\sigma)]^2 + \frac{t}{\alpha}\sum_{\boldsymbol{k}} J_{pair}(\boldsymbol{k})[-\nabla^2_{\boldsymbol{k}}]^{\lambda/2} J_{\mathrm{pair}}(\boldsymbol{k}) = \min \tag{24}$$

where λ (even) and t are free parameters and α is a normalization constant [90]. The second term on the right, i.e. the $\boldsymbol{k}$-space smoothness criterion, automatically selects essential short-ranged pair interactions. After equation (24) was applied to the pair interactions, a large number of different sets of three- and four-body figures is tested for whether it improves the rms error of the overall fit. An individual multi-body interaction is only added to the fit if it clearly decreases Δ_{rms}. Table 2 shows the $N_\sigma = 25$ input formation enthalpies ΔH_f (‘direct’) and the via MSCE fitted enthalpies (‘CE’) for Al–Zn. All enthalpies with an asterisk denote structures not used in the fit, i.e. they present ‘real’ predictions. The table gives the stoichiometry of all used input structures as well as the information whether the structures possess a SL of Al and Zn layers along a certain direction. For example, $V3$ is defined by an AlZn$_3$ SL in the [111] direction. So, there are always three Zn(111) layers followed by one Al(111) layer. The average error of fitting $N_\sigma = 25$ enthalpies is 1.5 meV whereas the resulting prediction error for the 9 structures not used for the fit is 2.2 meV. Figure 7 gives the resulting pair and multi-body interactions for the system Al–Zn. It can be seen that pair interactions converge rapidly, so that consideration of 15–20 pair interactions is sufficient.

---

[2] It has been found [106] that attenuating the constituent strain term can be important in strongly anharmonic, ordering type systems. This is realized by an exponential damping function. However, since attenuating the constituent strain has no significant effect on the systems considered in this paper, this will not be discussed here.

Table 2. Formation enthalpies of Al–Zn structures determined via DFT calculations (‘direct’) and CE. The compounds are sorted by SL direction and composition. Compounds marked by an asterisk did not enter the input of the CE fit, but represent predictions. While the ‘average error’ gives the standard deviation of CE formation enthalpies of input structures, the ‘average prediction error’ represents the standard deviation of all predicted structures. The ‘maximum error’ is the largest deviation between the CE and LDA values of the structures considered [94]. MSCE for AIZN. Average error (CE, 25 structures): 1.5 meV; average prediction error (9 predictions *): 2.2 meV; maximum error: 4.1 meV.

		Formation enthalpies (meV/atom) for direction					
Stoichiometry	x_{Al}	[100]	[110]	[111]	[201]	[311]	Others
Zn	0.0						fcc
direct:							0.0
CE:							0.6
$AlZn_3$	0.25		Y3*	V3	D0$_{22}$b	W3	L1$_2$
direct:			24.8	4.3	13.3	9.0	5.3
CE:			24.2	3.7	12.5	11.0	9.2
$AlZn_2$	0.333	$\beta 2$	$\gamma 2$	$\alpha 2$			
direct:		14.9	17.7	2.0			
CE:		18.3	21.3	3.3			
Al_2Zn_3	0.40	Z7*					
direct:		7.0					
CE:		7.2					
AlZn	0.50	L1$_0$		L1$_1$			
direct:		23.5		7.4			
CE:		26.9		9.9			
Al_2Zn_2	0.50	Z2	Y2	V2	CH(40)	W2	
direct:		9.0	24.6	4.8	24.8	18.6	
CE:		9.6	26.8	7.3	28.8	22.3	
Al_3Zn_3	0.50	Z6*	Y6*	V6			
direct:		6.2	18.8	2.8			
CE:		5.7	16.4	3.2			
Al_4Zn_4	0.50			V8*			SQS8*
direct:				1.8			18.4
CE:				1.7			20.9
Al_3Zn	0.60	Z5*					
direct		6.0					
CE:		6.2					
Al_2Zn	0.667	$\beta 1$	$\gamma 1$	$\alpha 1$			
direct:		17.4	32.6	15.9			
CE:		20.4	33.7	16.7			
Al_3Zn	0.75	Z1	Y1*	V1	D0$_{22}$ a	W1*	L1$_2$
direct:		10.2	26.0	14.6	27.6	23.0	35.1
CE:		14.1	27.2	12.7	31.6	25.8	34.9
Al_7Zn	0.875						D7
direct:							10.7
CE:							12.4
Al	1.00						fcc
direct:							0.0
CE:							−0.6

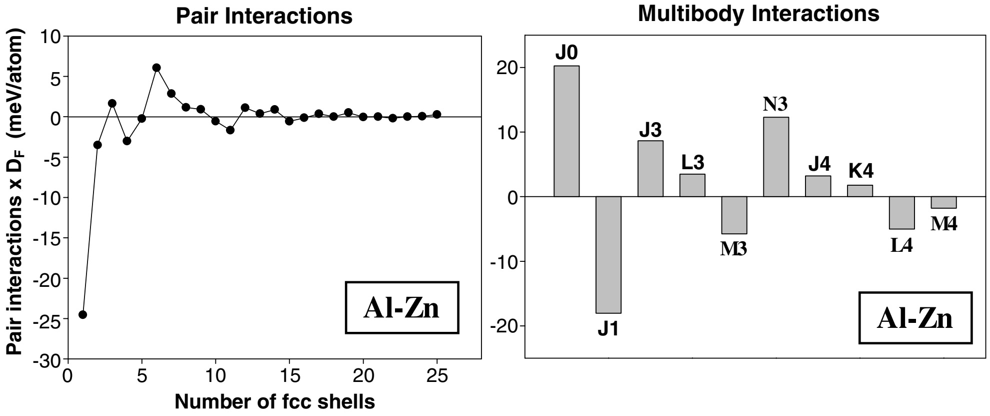

Figure 7. Pair and multi-body effective cluster interactions for Al–Zn deduced from the fit of table 2. The symbols characterize individual multi-body interactions: '3' stands for three- and '4' for four-body interactions. In general, the distance between atoms increases with the letter, i.e. for example, 'J' means only nearest neighbours, 'K' nearest neighbours and one second nearest neighbour, etc.

As example for the energetic behaviour of long-periodic superstructures, figure 8 shows via MSCE calculated interfacial energies of $\mathrm{Al}_n\mathrm{Zn}_n$ SL as a function of period length n for five different crystal orientations. Hereby, the interfacial energy per atom is defined as

$$I(n,\hat{G}) = \tfrac{1}{2}(\Delta H_f^{\mathrm{SL}}(n,\hat{G}) - \Delta E_{\mathrm{CS}}^{eq}(x=0.5,\hat{G})) \tag{25}$$

where the factor $\frac{1}{2}$ results from the fact that there are two interfaces. It can be seen that, for small n, the interfacial energies are not only direction-dependent, but also depend on n. In other words, the chemical interactions at the interfaces dominate the interfacial energy. This effect can, for example, be of importance for ultrathin sandwich films in multi-layer systems. With increasing n the influence of the interfaces on the interfacial energy disappears. $I(n,\hat{G})$ is now determined by the direction-dependent strain energy necessary to maintain coherence between the blocks of Al and Zn layers.

For finite-temperature studies, equation (21) can be used in MC simulations. The code we applied for studying thermodynamic properties is a simple Metropolis algorithm [107] allowing for flipping pairs of A and B atoms in an *arbitrary* distance with the aim of reaching the equilibrium configuration as fast as possible. The procedure is as follows:

(i) Select randomly a pair of A and B atoms.
(ii) Calculate the energy difference δE caused by exchanging the two atoms. If $\delta E < 0$, flip the two spins; if $\delta E > 0$, flip the two spins with a probability of $\exp(-\delta E/kT)$ (again, E is obtained from equation (21)).
(iii) Go to 1.

Besides the temperature dependence of the alloy's free energy, MC simulations can be used to calculate coherent phase boundaries in the phase diagram. Following the fluctuation-response theorem [108], the specific heat c_v of the system at a certain temperature can be calculated by the fact that c_v is proportional to the equilibrium fluctuations of the energy, $\langle E^2\rangle - \langle E\rangle^2$. Since the energy exhibits a point of inflection for a second-order phase transition at the transition temperature T_{trans}, its response function $c_v = (\partial E/\partial T)_v$ has a maximum at T_{trans}. Although a phase transition is—strictly speaking—only defined for an *infinite* system, one usually also

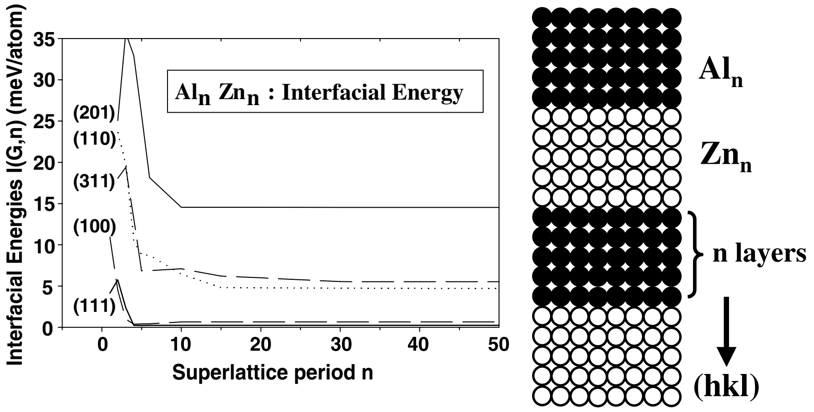

Figure 8. Via MSCE calculated interfacial energies for Al$_n$Zn$_n$ SL as a function of direction and period length n.

speaks of a phase transition of a *finite* system, given by the maximum of c_v at the transition temperature. If the MC simulations are applied for different concentrations x, the resulting T_{trans} values can be used to construct the coherent phase boundary of a system.

Another important application of MC simulations is the prediction of the system's ordering. Of special interest are SRO effects in disordered alloys which can quantitatively expressed in terms of SRO parameters, as introduced in section 2. For this, we rewrite equation (3) in the equivalent form

$$\alpha_{lmn}(x) = 1 - \frac{P_{lmn}^{\mathrm{A(B)}}}{x} \tag{26}$$

where $P_{lmn}^{\mathrm{A(B)}}$ is the conditional probability that, given an A atom at the origin, there is a B atom at (lmn). For comparison with experimental data, the so-called 'shells' lmn are introduced which are defined by the distance between A and B atoms in terms of half-lattice parameters, $(l\frac{a}{2}, m\frac{a}{2}, n\frac{a}{2})$, e.g. for an fcc lattice the nearest-neighbour distance would be described by the shell (110), the second-nearest-neighbour distance by (200) and so on. As already mentioned, the sign of α indicates whether atoms in a given shell prefer to order ($\alpha < 0$) or cluster ($\alpha > 0$). The SRO parameter may be written in terms of the CE pair correlations as [95]

$$\alpha_{lmn}(x) = \frac{\langle \bar{\Pi}_{lmn} \rangle - q^2}{1 - q^2} \tag{27}$$

where $q = 2x - 1$ and $\langle \bar{\Pi}_{lmn} \rangle$ is the pair correlation function, equation (15), for the shell (lmn). In diffraction experiments the diffuse scattering due to SRO is proportional to the lattice Fourier transform of $\alpha_{lmn}(x)$ [34, 35]:

$$\alpha(x, \boldsymbol{k}) = \sum_{lmn}^{n_R} \alpha_{lmn}(x) \mathrm{e}^{\mathrm{i} \cdot \boldsymbol{k} \cdot \boldsymbol{R}_{lmn}} \tag{28}$$

where n_R stands for the number of real space shells used in the transform. Equation (27) together with (28) opens the possibility of comparing both, experimental and theoretically predicted diffuse diffraction patterns (reciprocal space) and SRO parameters (real space). This concept will be applied in section 4.2 to understand SRO phenomena in binary metal alloys *quantitatively*.

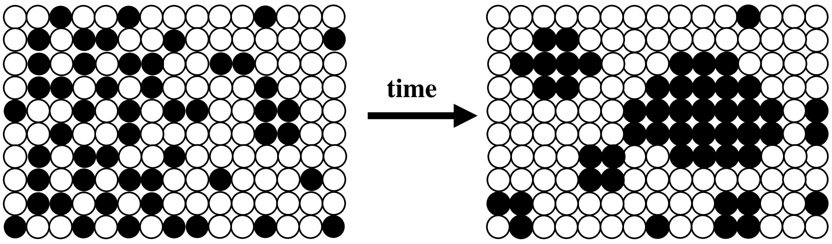

Figure 9. Schematic crystal plane of an $A_{1-x}B_x$ alloy with characteristic islands formed by B (black) atoms during the ageing process.

3.3. *Beyond thermodynamics: simulation of dynamic processes*

The kinetic MC method [43, 109, 110] is one of the most successful approaches to describe diffusion, growth and microstructure evolution in alloy systems [111]. Different approaches for describing shape evolutions of microstructures in alloys are used, such as the Onsager equation in mean-field approximation [112–114], a microscopic mean-field kinetic equation [115], the stochastic field method [116] or the discrete atom method [117–119]. In contrast to such continuum models that require a knowledge of the energy surface for *arbitrary atomic configurations*, we now use the discussed 'MSCE plus MC' combination to investigate the time evolution of characteristic microstructures in binary alloys, the so-called precipitates.

Perhaps the best-known examples of heterogeneous phase coexistence are phase separation of an alloy into its constituents [24] $A_{1-x}B_x \rightleftharpoons (1-x)A + xB$ or into a constituent plus a compound [24], e.g. $A_{1-x}B_x \rightleftharpoons A_3B + A$. Such solid state decomposition reactions create *precipitates* which represent an important part of the microstructure of many alloy systems. The early stage of these reactions typically involves the formation of *coherent precipitates* that adopt the crystallographic lattice of the alloy from which they emerge [120]. Because of their practical importance (see sections 4.3 and 4.4), the time evolution of the precipitates' sizes and shapes is of interest, too. In this section, we will introduce two kinetic MC algorithms, again based on the MSCE Hamiltonian, equation (21). Figure 9 demonstrates the situation by a simplified two-dimensional presentation: a quenched solid solution (left frame) is aged at a certain temperature (e.g. room temperature). During this ageing process islands are formed (right frame) which may show a characteristic size and shape distribution (we assume that the islands are formed by black B atoms in an A-rich $A_{1-x}B_x$ alloy). The question is whether the distribution of these islands as a function of ageing time can be calculated from first principles.

As already mentioned, our main focus is on the distribution of the islands as a function of temperature and ageing time; the path of an individual B atom through the crystal is less interesting. Therefore, we make the following assumptions:

(i) The islands are formed by nearest-neighbour site flips only and not by continuous atomic motion. The energies $E_{\text{CE}}(\sigma)$ before and after spin flips always correspond to geometrically fully relaxed configurations. This is guaranteed by the MSCE Hamiltonian, equation (21).

(ii) Our model does not consider vacancies. This assumption is motivated by the fact that, for a correct calculation of the precipitate distribution, the detailed exchange process does not play much of a role as long as the time constant for the exchange process is known. (In bulk crystals the exchange of A and B atoms is based on a three-particle process with a vacancy as the third particle.)

(iii) Additional to the energy difference between two neighbouring sites occupied with

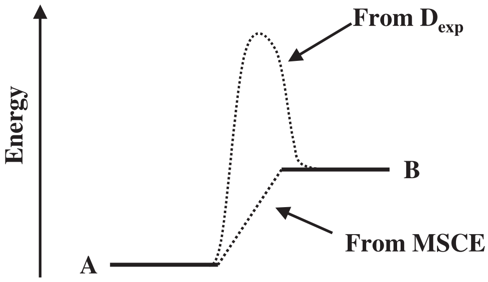

Figure 10. Basic assumption in our simulations: while the energy difference between two neighbouring atoms can be easily calculated from the MSCE, an average and temperature-dependent activation barrier is calculated from experimental, temperature-dependent diffusion data.

dissimilar atoms, the activation barrier for the exchange has to be taken into account as schematically shown in figure 10. It is possible to compute diffusion coefficients from first principles, but this can be complicated and time-consuming.

Instead, the energy barriers between different configurations are taken from experiment: the frequency $1/\tau_0$ for the exchange process as a function of temperature T can be deduced from the experimental diffusion constant [28] $D_{exp}(T)$ via

$$\tau_0(T) = \frac{a_{\mathrm{nn}}^2}{D_{exp}(T)}, \tag{29}$$

where a_{nn} is the average nearest-neighbour distance between atoms. Although this might appear as a very rough approximation, $D_{exp}(T)$ contains the real 'average' energy barrier, and therefore the exchange frequency implicitly contains this information too. It should be noted that this approximation pertains *only* to the activation barrier and *not* to the configurational energy (figure 10), $E(\sigma)$, given by the MSCE of equation (21).

Two types of algorithms were constructed which we may call 'algorithm I' and 'algorithm II' in the following. Algorithm I (described here for A-rich A–B alloys) has the following simple structure:

(i) Find all N atoms of B in a random configuration, order them by site indices and select the B atom with the lowest site index.
(ii) Determine how many of its neighbours are A atoms.
(iii) Select an arbitrary one of the A neighbours.
(iv) If the energy difference δE caused by exchanging the two atoms is $\delta E < 0$, flip the two spins, but if $\delta E > 0$, flip the two spins with a probability of $\exp(-\delta E/kT)$. Here, δE is obtained from equation (21) (given by the difference of the formation enthalpies of the structures before and after the spin flips). Note that this energy results with all atoms relaxed and so corresponds to the (local) energy minimum of the configuration σ.
(v) Repeat steps 2–4 for all B atoms.
(vi) Use equation (29) to transfer 1 MCS into 'real time'.
(vii) Go to point 1.

In this algorithm, one Monte Carlo step (MCS) is defined as 'one trial for each B atom to switch site with a neighbouring A atom'. The *advantages* of this algorithm are:

(i) B atoms are not chosen randomly: instead *each* B atom has the chance to 'jump' once per MCS. Therefore, the exchange processes of different B atoms with A atoms are as simultaneous as possible.

(ii) One MCS represents a constant time interval, i.e. MC time and real time are linearly related.

The *disadvantage* of the algorithm is its inefficiency when most of the B atoms are already attached to one of the islands, as in the right frame of figure 9. Since precipitation is a phase-separating process, the probability that any B atom will ever move again, i.e. leave the island to which it is already attached, becomes very low. Especially at low temperatures, B atoms at the interface between B islands and the A matrix will practically never leave this area.

Possible solutions for this problem could be: (a) cluster algorithms, or (b) enforcing the exchange process. Cluster algorithms [121, 122] are based on the idea that forming a cluster consisting of many spins first and flipping them simultaneously is less time-consuming than flipping individual spins. However, such algorithms would not be very efficient, when the formation of large clusters is very computer-time-consuming, but the probability for flipping them is very low. In this case, the flip is rejected for many clusters. This is exactly the situation encountered in phase-separating systems.

The main problem of forcing a B atom to leave the island boundary (method (b)) is that it will most likely return to the island boundary in the next MCS (because the probability is very high for this). Forbidding this second step in the simulation leads to a non-Markovian process, which demands a complex re-consideration of the relation between the experimental diffusion constant and the computer time unit 'MCS'. Furthermore, the question arises, for how many MCS the 'returning' event has to be forbidden. Even if we do not allow for a certain B atom to return to the island in MCS step j, following the removal in MCS step $j-1$, it is very likely that this 'returning' event will happen in MCS step $j+1$. The best solution for this problem seems to be an algorithm where the selected B atom is forced to jump *without destroying the Markovian process* [47]. This is realized in the following algorithm ('algorithm II'):

(i) Find all of the N atoms of B in a random configuration and order them by site indices.
(ii) Determine all possible jumps S for *each* of the N atoms of B (for an fcc lattice $S^{max} = 12N$, when all B atoms only have A atoms as neighbours).
(iii) Calculate the energy change $\delta E(i)$ for *all* allowed 'jumps' for every B atom ($i = 1, \ldots, S$).
(iv) If $\delta E(i) > 0$, calculate $W_i = (1/\tau_0)\exp(-\delta E(i)/kT)$. If $\delta E(i) < 0$, calculate $W_i = 1/\tau_0$. Do this for all allowed 'jumps', $i = 1, \ldots, S$ (use equation (29) to calculate τ_0).
(v) Calculate $P_i = W_i/W_{\mathrm{tot}}$, where $W_{\mathrm{tot}} = \sum_{i=1}^{S} W_i$.
(vi) Select randomly one jump i from the S possible events according to their probability P_i.
(vii) Calculate the new total simulation time $t_{\mathrm{MCS}} = t_{\mathrm{MCS}-1} + 1/W_{\mathrm{tot}}$. (Note that $W_{\mathrm{tot}} = \sum_{i=1}^{S} W_i$ is *not* a constant, but is different for each MCS. So, recording t_{MCS} after each MCS is a 'must'.)
(viii) Recalculate all $\delta E(i)$'s.
(ix) Return to step 4.

The efficiency of this method strongly depends on whether the calculation of the new $\delta E(i)$'s (step 8) is time-intensive. An accepted spin flip demands a recalculation of $S(\boldsymbol{k}, \sigma)$ in equation (21). However, as shown by Lu *et al* [89], the MSCE method allows us to avoid the necessity of recalculating $S(\boldsymbol{k}, \sigma)$ after each move by directly calculating the *change* in $J_{\mathrm{pair}}(\boldsymbol{k})|S(\boldsymbol{k}, \sigma)|^2$ for each move in real space [89]. In practice, algorithm II is clearly slower for short ageing times and high temperatures, i.e. when most of the spin flips are accepted. The advantage of algorithm II lies in the simulation of long ageing times: as we can see from step 4 of the algorithm, a single MCS is now *not longer a constant real time unit*, but depends on the corresponding probability W_{tot}. In practice, one MCS can now represent real times of

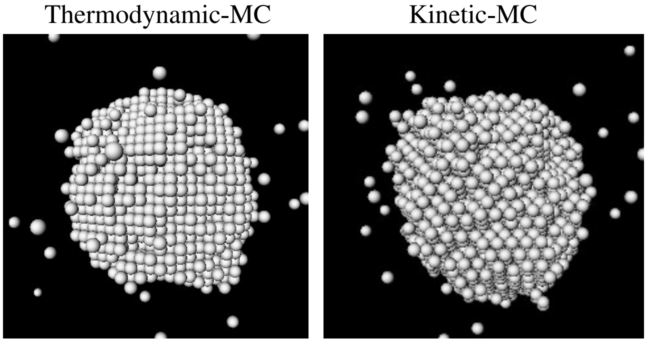

Figure 11. Comparison between equilibrium configurations for an $Al_{0.92}Zn_{0.08}$ alloy ($T = 300$ K) resulting from thermodynamic and kinetic MC simulations (only Zn atoms are shown) [47].

1/1000 s up to many minutes. As a rough rule, we can conclude that algorithm II is to be preferred if one MCS corresponds to a real time of about 1 s.

In algorithm II a single MCS corresponds indeed to only a single exchange of one B atom with one A atom and *not* to one trial flip for each B atom. Since the ‘flip channel’ i is always chosen randomly and mostly a large number of B atoms (typically 10^3–10^5) is considered to describe real ageing processes, the probability that the same B atom is chosen in MCS step i, when it was already chosen in MCS step $i - 1$ is extremely small. So, due to the large system size it is not necessary to forbid certain exchanges between A and B atoms, i.e. we do not have to give up the restriction that the algorithm should be based on the Markovian process. The concept of algorithm II is strongly related to that of the so-called ‘residence-time algorithm’ [110], where one transition is performed at each MCS, too. Different to the work of Soisson *et al* [123], who applied such an algorithm to study Cu precipitation in Fe–Cu alloys, our model does not consider any vacancy jump mechanism. However, the configurational part of the energy is treated with DFT accuracy. Our present kinetic simulations are restricted to nearest-neighbour ‘jumps’ only. Though this will probably not work generally, it was already successfully applied in the literature [117]. For certain applications, an extension to second-, third- and further nearest-neighbour exchange processes may be needed.

Both algorithms fulfil the condition of detailed balance which guarantees the convergence of the Markovian chain [124]. Although the kinetic MC algorithms are not suitable for studying equilibrium configurations (indeed, it takes about an order of magnitude longer to reach equilibrium via kinetic MC than via thermodynamic MC algorithms), the calculations of an equilibrium configuration are an important test regarding the validity of the developed kinetic MC algorithms. As an example [47] for the kinetic MC versus thermodynamic MC comparison, figure 11 shows the result for an fcc-based $Al_{0.92}Zn_{0.08}$ alloy embedded in a $30 \times 30 \times 30$ MC cell at $T = 300$ K where the three-dimensional precipitates consist of Zn atoms only (therefore, in figure 11 only Zn atoms are shown). The predicted precipitate shapes resulting from kinetic MC and thermodynamic MC agree very well (a more quantitative comparison can be found in [47]). In section 4.4 we will see how the algorithms developed permit one to investigate real, three-dimensional, ageing processes in binary metal alloys.

3.4. How to study surfaces. . .

As already discussed in section 2, a successful description of alloy surfaces demands the consideration of surface-specific phenomena. These are:

Table 3. Surface energies of fcc-Al and fcc-Zn. For all three considered orientations, fcc-Zn has the lower surface energy.

Surface orientation	ΔE_{surf} (eV/atom)	
	Al	fcc-Zn
(100)	0.55	0.54
(110)	0.83	0.64
(111)	0.42	0.25

(i) *Multi-layer relaxations:* distances between near-surface layers can profoundly differ from the bulk layer spacing.

(ii) *Surface segregation:* the chemical composition in the first few layers may strongly deviate from the bulk concentration.

(iii) *Surface reconstruction:* the enrichment of one component near the surface may lead to the formation of a superstructure ($ma_1 \times na_2$), with a_1 and a_2 being the in-plane lattice vectors of the unreconstructed surface and m, n are integers. Such superstructures can be generated by long-range ordering of different atomic species ('chemical superstructure') or by buckling of atoms ('geometric superstructure'). This buckling can also be statistical in the sense that unlike atoms within a single layer are above or below the average layer plane, but no LRO can be observed.

(iv) *Order–disorder transition:* bulk and surface ordering can be completely different. It is, for example, possible that the bulk structure is a disordered alloy, while the surface structure exhibits lateral LRO. Even if both surface and bulk represent disordered alloys, their SRO behaviour can be different.

We will now transfer our theoretical concepts discussed above to surfaces. This includes (a) DFT as well as (b) CE and MC simulations. Furthermore, the possibility of verifying our calculations by (c) LEED intensity analyses is introduced.

(a) DFT at surfaces. In the last few years, DFT calculations have become more and more important in understanding the electronic and structural properties of surfaces, from pure elements [125–128] and adsorbate systems [129, 130] to epitaxial films [131–133] and alloy surfaces [51]. Although the main activities were in the field of semiconductor surfaces, the development of efficient computer codes and faster computers today permit us to treat very complex metal and alloy surfaces requiring model systems containing up to about 200 metal atoms. This even allows us to study grain boundaries (see section 5.3).

The most common model in first-principles calculations to describe surfaces is the use of repeated, periodic slabs: first, a bulk-like crystal consisting of N_{bulk} atoms is formed by stacking atomic layers normal to the surface of interest. For this model, a DFT calculation is performed. The resulting total energy of the system, $E_{\mathrm{tot}}^{\mathrm{bulk}}$, represents the reference energy. Next, a certain number of layers are removed so that a slab consisting of N_{surf} atoms with two vacuum/solid interfaces emerges. The structure at this 'interface' has to be relaxed in the DFT calculation, yielding $E_{\mathrm{tot}}^{\mathrm{surf}}$. Then, the *surface energy*, i.e. the energy necessary to create the surface of a pure-element crystal, is given as

$$\Delta E_{\mathrm{surf}} = \frac{1}{2}\left(E_{\mathrm{tot}}^{\mathrm{surf}} - \frac{N_{\mathrm{surf}}}{N_{\mathrm{bulk}}} E_{\mathrm{tot}}^{\mathrm{bulk}}\right). \tag{30}$$

The factor $\frac{1}{2}$ takes the two surfaces into account. Naturally, the number of layers and removed layers has to be increased until ΔE_{surf} remains unchanged. Because it always costs energy to create a surface, $\Delta E_{\mathrm{surf}} > 0$. As an example, table 3 gives the surface energies per atom for the three low index surfaces of fcc-Al and fcc-Zn. Although Zn normally possesses the hcp structure, the calculations for Zn were performed for fcc-Zn, because in Al–Zn alloys (see section 4.3) Zn is forced to crystallize on the fcc lattice and therefore the properties of fcc-Zn are important for investigating the Al–Zn alloy system. From the surface energies of the pure elements, we may already guess that, especially for Al–Zn(111) surfaces, Zn will probably segregate to the alloy surface because of its very low surface energy as compared to Al(111). While a guess on such simple grounds may be valid for phase-separating systems when clustering is preferred at the surface, it may totally fail for ordering systems because interactions between unlike atoms are totally ignored. As an example, in section 5 $\mathrm{Co}_{0.5}\mathrm{Al}_{0.5}(100)$ surfaces are discussed where the bulk forms an intermetallic compound, namely the B2 structure. This structure can be described by alternating Co and Al layers along the [100] direction. For this system, a small surplus ϵ of Co atoms (called 'defect atoms' or 'antisites', because they have to occupy sites of the Al sublattice) in a $\mathrm{Co}_{0.5+\epsilon}\mathrm{Al}_{0.5-\epsilon}$ alloy leads to the segregation of Co antisites to the Al-terminated alloy surface, although Al has the lower surface energy. For such surfaces, the interactions between neighbouring like and unlike atoms will certainly strongly influence the properties of the alloy surface. In order to take those interactions into account, we introduce the following two quantities: the *surface energy of the alloy* is defined analogous to that of the pure element as the difference between the energy of the alloy surface slab, $E_{\mathrm{tot}}(N_{\mathrm{surf}}^{\mathrm{A}}, N_{\mathrm{surf}}^{\mathrm{B}})$ (with $N_{surf}^{\mathrm{A(B)}}$ being the number of A and B atoms in the surface slab) and the corresponding volume slabs, $E_{\mathrm{tot}}(N_{\mathrm{bulk}}^{\mathrm{A(B)}})$ (with $N_{\mathrm{bulk}}^{\mathrm{A(B)}}$ being the number of A and B atoms in the bulk), of the pure materials. From this difference, the formation enthalpy $\Delta H_f(\mathrm{AB}, N_{bulk}^{A}, N_{bulk}^{B})$ of the stable bulk phase (e.g. the B2 structure for Co–Al) has to be subtracted:

$$\begin{aligned}\Delta E_{\mathrm{surf}} = \frac{1}{2N_{\mathrm{surf}}}\Bigg(& E_{\mathrm{tot}}(N_{\mathrm{surf}}^{\mathrm{A}}, N_{\mathrm{surf}}^{\mathrm{B}}) - \frac{N_{\mathrm{surf}}^{\mathrm{A}}}{N_{\mathrm{bulk}}^{\mathrm{A}}} E_{\mathrm{tot}}(N_{\mathrm{bulk}}^{\mathrm{A}}) \\ & - \frac{N_{\mathrm{surf}}^{\mathrm{B}}}{N_{\mathrm{bulk}}^{\mathrm{B}}} E_{\mathrm{tot}}(N_{\mathrm{bulk}}^{\mathrm{B}}) - \Delta H_f(\mathrm{AB}, N_{\mathrm{bulk}}^{\mathrm{A}}, N_{\mathrm{bulk}}^{\mathrm{B}})\Bigg).\end{aligned} \tag{31}$$

N_{surf} stands for the number of atoms in the surface unit cell. Although this definition accounts for interactions between A and B atoms, the resulting surface energy refers to the surface of a *perfectly ordered* compound, namely one characterized by the subtracted formation enthalpy, ΔH_f (here, the B2 structure). In reality, however, the energetic situation is much more complex: the formation of the segregation profile demands the transport of individual atoms (e.g. Co antisites in Co–Al) from the bulk to the surface and vice versa. More specifically, the energy to *replace* an A atom at the surface by a B atom from the bulk comes into play. This energy is called the *segregation energy*:

$$\begin{aligned}\Delta E_{\mathrm{seg}} = & \frac{E_{\mathrm{tot}}(N_{\mathrm{surf}}^{\mathrm{A}} - 2, N_{\mathrm{surf}}^{\mathrm{B}} + 2)}{2} - \frac{E_{\mathrm{tot}}(N_{\mathrm{surf}}^{\mathrm{A}}, N_{\mathrm{surf}}^{\mathrm{B}})}{2} \\ & + E_{\mathrm{tot}}^{\mathrm{bulk}}(N_{\mathrm{bulk}}^{\mathrm{A}}, N_{\mathrm{bulk}}^{\mathrm{B}}) - E_{\mathrm{tot}}^{\mathrm{bulk}}(N_{\mathrm{bulk}}^{\mathrm{A}} - 1, N_{\mathrm{bulk}}^{\mathrm{B}} + 1).\end{aligned} \tag{32}$$

The individual terms in this equation need some more explanation: $E_{\mathrm{tot}}(N_{\mathrm{surf}}^{\mathrm{A}}, N_{\mathrm{surf}}^{\mathrm{B}})$ gives the energy of the bulk-like terminated alloy surface, i.e. with no antisite in the bulk or at the surface. Now, we repeat the calculation with an antisite of atom type B in the topmost alloy layer. Since there are two surfaces, the total number of A atoms in the surface slab decreases by 2 atoms, while the number of B atoms increases by 2 atoms. The difference between the energies with and without an antisite determines whether the stability of the surfaces is decreased or increased by the antisite. However, the same energy balance has to be made for the bulk, i.e. the bulk energies with and without an antisite have to be compared (since for Co–Al(100) our DFT model consists of an odd number of atomic (100) layers in order to conserve the point symmetry of the slab, there is only a single antisite in the centred layer). So, the segregation energy determines whether antisites segregate to the surface or remain in the bulk. The difference in bulk energies with and without an antisite is also known as *antisite energy*:

$$\Delta E_{\mathrm{AS}} = E_{\mathrm{tot}}^{\mathrm{bulk}}(N_{\mathrm{bulk}}^{\mathrm{A}} - 1, N_{\mathrm{bulk}}^{\mathrm{B}} + 1) - E_{\mathrm{tot}}^{\mathrm{bulk}}(N_{\mathrm{bulk}}^{\mathrm{A}}, N_{\mathrm{bulk}}^{\mathrm{B}}). \tag{33}$$

Segregation energies of binary alloys will be discussed in section 5.1.

(b) Surface CE and MC. The problem with the definition of the segregation energy, equation (33), comes from the fact that it describes the energetics of all atoms in some *average* environment. Although this approximation is certainly correct when the segregating species prefers to occupy a certain atomic site in the surface layer, it will probably fail to describe quantitatively the segregation profile of disordered alloys at finite temperatures. Then the energy of an atom at the surface depends on its *particular* structural environment. So, for many alloy surfaces SRO must be considered which again demands, analogous to the bulk alloy, the consideration of a large number of atoms per layer. This can be done by extending the combination of bulk CE and MC methods to surfaces. For this, we have to regard that the symmetry at the surface is reduced compared to the bulk. Consequently, the number of geometrically different figures, for which effective interactions are constructed, will increase. For this reason, a larger number of input structures is needed to stabilize the surface interactions compared to the bulk. It is, however, possible to circumvent a part of this problem by treating the surface interactions as a correction of the bulk interactions. Since energies are additive, we may write

$$\Delta H_f^{\mathrm{CE}} = \Delta H_f^{\mathrm{vol}} + \Delta H_f^{\mathrm{surf}}. \tag{34}$$

For the volume CE, $\Delta H_f^{\mathrm{vol}}$, the mixed-space presentation, equation (21), may be used. Since most segregation profiles are restricted to a very small number of surface layers, a real-space presentation can be applied for the surface part, as successfully demonstrated by Drautz *et al* [51] for Ni-rich Ni–Al surfaces. The advantage in treating the surface interactions as 'perturbations' of the bulk interactions comes from the fact that the DFT calculations for different surface terminations (SRO models) and segregation profiles must not consider an infinite bulk reservoir. We only have to make sure that the DFT slab model is thick enough that the centre layer of the slab becomes bulk-like. For example, in the case of Co–Al already nine layer thick surface slabs are sufficient, because the layer distances between layers number 4 and 5 and layers number 5 and 6 are bulk-like for the geometrically relaxed slab. For the real-space CE presentation the energy of a structure σ can then be written as

$$E(\sigma) = \sum_{i=1}^{N} \left\{ \sum^{N_F} \bar{\Pi}_F(\sigma) D_F J_F + \sum^{N_F'} \bar{\Pi}_F'(\boldsymbol{R}_i) D_F'(\boldsymbol{R}_i) \delta J_F(\boldsymbol{R}_i) \right\}. \tag{35}$$

We see that for the surface part the interactions become site-dependent. Here, $\boldsymbol{R}_i$ defines the position of the atom i with respect to the alloy surface. So, for an atom i within the segregation profile, every individual interaction J_f to neighbouring atoms will be corrected to $J_f + \delta J_f(\boldsymbol{R}_i)$. Naturally, with increasing distance from the alloy surface, $\delta J_f \rightarrow 0$ and consequently the surface term in equation (35) becomes zero. The extended Hamiltonian can now again be used in MC simulations. Analogous to the bulk calculations, we choose a random configuration as the starting point and determine the segregation profile as a function of temperature by MC simulated annealing. Since the concept of CE allows us to treat large systems (see section 3.2), the number of atoms per layer can be chosen large enough (e.g. 5000 atoms per layer) to make layer-dependent SRO phenomena visible. A layer-dependent analysis of SRO allows for studying correlations between ordering and segregation. This combination of surface CE and MC permits us to study surface segregation for *geometrically fully relaxed surfaces* by purely quantum mechanical and statistical principles, i.e. without any continuum approaches, empirical parameters or neglecting correlations between structure and segregation.

(c) LEED intensity analysis. So far, our calculations regarding surface structure and segregation profiles are predictive. Now, we want to establish a complementary, experimental view of the geometric structure and chemical composition by analysing LEED $I(E)$ spectra via a multiple-scattering theory. Because of the huge number of publications in this field only some main aspects are mentioned here: the solution of the time-independent Schrödinger equation for an electron influenced by the potential of the crystal surface is given by the Lippmann–Schwinger equation [134, 135]. Here the state $|\Psi\rangle$ of a scattered LEED electron is given by

$$|\Psi\rangle = (\mathbf{1} + \boldsymbol{G_0 T})|\vec{k}_0\rangle \tag{36}$$

with $\boldsymbol{G_0} \equiv (E - V_0 - \frac{p^2}{2m})^{-1}$ being Green's operator for the free electron. V_0 is called the 'inner potential' and considers the influence of exchange and correlation effects on the LEED electron (real part) inside the crystal surface as well as inelastic processes (imaginary part). The matrix $\boldsymbol{T}$ in equation (36) is defined by $\boldsymbol{V}|\Psi\rangle = \boldsymbol{T}|\vec{k}_0\rangle$ with $\vec{k}_0$ being the direction of the incident electrons and allows for a self-consistent solution of the scattering problem. In principle, the transferred intensity by diffraction of an incident electron beam from direction $\vec{k}_0$ to direction $\vec{k}_g$ may be directly calculated as

$$I(\vec{k}_0, \vec{k}_g) = |A_0(\vec{k}_0, \vec{k}_g)|^2 = |\langle \vec{k}_g|\mathbf{1} + \boldsymbol{G_0 T}|\vec{k}_0\rangle|^2. \tag{37}$$

In practice, however, this is done in three steps as schematically shown in figure 12. First, the atomic t matrix, which describes the amplitude of the scattering of a spherical wave by an atom, is calculated. Due to spherical symmetry the atomic scattering matrices $\boldsymbol{t}^i$ are diagonal in angular momentum space. Because of the low electron energy (typically 30–600 eV) they can be calculated by a *small* number of atomic phase shifts δ_i^j:

$$\langle l'm'|\boldsymbol{t}^j|lm\rangle = t_l^j \delta_{l,l'}\delta_{m,m'} \tag{38}$$

$$\text{with} \qquad t_l^j = \frac{1}{2\mathrm{i}k_0}(\exp(2\mathrm{i}\delta_i^j) - 1) \tag{39}$$

$$\text{and} \qquad k_0 = \sqrt{2(E - V_0)}. \tag{40}$$

The atomic scattering matrices are then applied to calculate the diffraction matrix M of an atomic layer. Finally, the layers are stacked to form a real three-dimensional crystal surface (figure 12). The $\boldsymbol{t}^i$'s can also be used for applying perturbation methods to LEED theory. The basic idea [57, 58] comes from the fact that LEED $I(E)$ spectra only slightly change their shape for small structural changes. The parameter variations are not even restricted to geometrical parameters. Changes in the chemical composition of the surface and in vibrational amplitudes also lead to continuous changes in the shape of the $I(E)$ spectra and therefore can be treated via perturbation theory, too.

In order to study the surface structure of substitutional disordered alloys, the atomic scattering matrices of elements A and B can be combined via the so-called average T-matrix approximation (ATA) [136]:

$$\boldsymbol{t}^i_{\mathrm{ATA}} = c_i\boldsymbol{t}_{\mathrm{A}} + (1 - c_i)\boldsymbol{t}_{\mathrm{B}}. \tag{41}$$

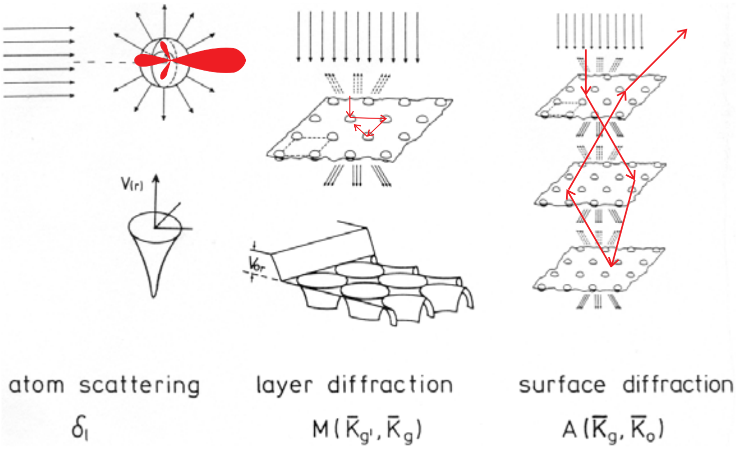

Figure 12. The principle of a full dynamical LEED intensity calculation: first, the atomic scattering matrix is evaluated. Next, a layer scattering matrix is calculated in angular momentum space. Finally, the layers are stacked to form a three-dimensional surface structure. The thickness of the slab depends on the penetration depth of the LEED electrons [53].

(This figure is in colour only in the electronic version)

Here, the original scattering matrices are replaced by a composition-weighted average *t* matrix. Since different chemical elements possess different scattering behaviours, the LEED analysis allows for a detailed determination of the composition of *each individual* surface layer, only limited by the finite mean free path. Therefore, a very accurate determination of the segregation profile of a binary alloy is possible. The chemical 'resolution' is naturally the higher the more different are the phase shifts of the pure elements. The disadvantage of the approximation is the inability of ATA to describe SRO effects. The advantage is the direct access to correlations between segregation profile and geometric surface structure.

For the comparison between experimental and theoretical best-fit spectra so-called reliability factors [55, 56] (R factors) are used. The probably best-suited R factor for the comparison of LEED spectra represents the *Pendry R-factor* R_p [55]. It attempts to treat *all* peaks as well as minima with equal weight (while the human eye would always favour large peaks over small peaks) and is based on the logarithmic derivative of the $I(E)$ curves:

$$R_p = \frac{\int (Y_{exp} - Y_{th})^2 \, \mathrm{d}E}{\int (Y_{exp}^2 + Y_{th}^2) \, \mathrm{d}E} \tag{42}$$

$$\text{with} \qquad Y = \frac{L}{1 + V_{0i}^2 L^2}$$

$$\text{and} \qquad L(E) = \frac{1}{I(E)} \frac{\mathrm{d}I(E)}{\mathrm{d}E}.$$

Here, V_{0i} is the damping potential, where $2V_{0i}$ can be taken as the average peak width of single peaks at half-maximum. The big advantage of R_p is that it allows for the calculation of a statistical error [55] given by the variance of R_p:

$$\mathrm{var}(R_p) = R_p^{min} \sqrt{\frac{8V_{0i}}{\Delta E}} \tag{43}$$

with ΔE being the complete energy range of the $I(E)$ database and R_p^{min} the minimum R factor.

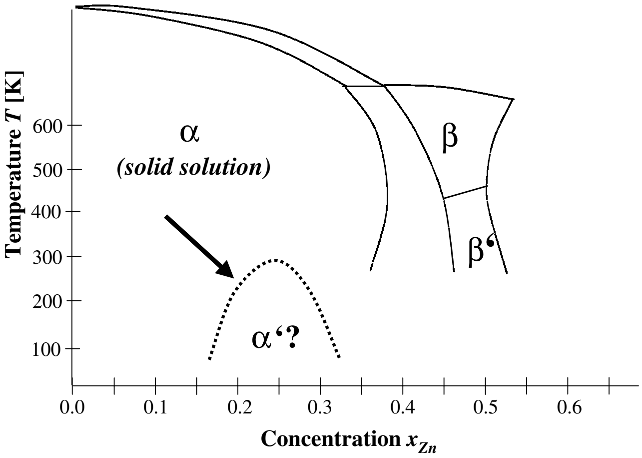

Figure 13. Schematic phase diagram for Cu-rich Cu–Zn alloys: while it is known that the bcc-based solid solution β orders in a B2 structure (β') for low temperatures, it is a long-standing question whether a long-range-ordered phase exists in the regime of the fcc-based solid solution α, too.

In section 5 we will see how the combination of LEED and DFT allows for a detailed characterization of surface structures.

4. Bulk properties of metal alloys

4.1. Ground state

The ground-state search of binary compounds by total-energy calculations and diagrammatic approaches suffers largely from the need that the small group of crystallographic configurations considered must include the stablest one. The combination 'MSCE plus MC' allows us to circumvent this problem as is now demonstrated for the many decades old question about the existence of a LRO phase in α-brass. Figure 13 schematically shows the phase diagram for Cu-rich Cu–Zn alloys. Below 35–38% Zn, the historically most-widely used form of brass [137] exists, so-called α-brass, with a disordered fcc structure. As the disordered bcc alloy (β) is known to have the B2 structure at low temperatures (β'), it was long suspected [138] that the disordered fcc alloy (α) will also order at lower temperatures. However, this ordered phase (which we might term α') was never detected—as we will see—possibly due to a low order–disorder transition temperature $T_{\text{trans}}^{\alpha\alpha'}$. Moreover, there are definite clues from experiment that ordering plays an important role in α-brass, i.e. it cannot be described as a *random* alloy. First, measurements [23] of the mixing enthalpy of the alloy yield negative values, suggesting the tendency of Cu and Zn atoms to order crystallographically below some temperature $T_{\text{trans}}^{\alpha\alpha'}$. Second, measurements of the diffuse neutron scattering [139] of a sample quenched from high temperature ($T > T_{\text{trans}}^{\alpha\alpha'}$) exhibit strong deviations from randomness, manifested by peaks of the scattering around the $\langle 1\frac{1}{4}0\rangle$ position and symmetrical equivalents in the Brillouin zone. Such peaks indicate that the disordered alloy develops non-random composition waves, i.e. there is a tendency for crystallographical order at low temperatures.

In 1931, Hume-Rothery [138] noted that Cu–Zn belongs to a class of compounds whose structure correlates with the electron-per-atom (e/a) ratio. In systems created from the $d^{10}s^1$ noble metals (Cu, Ag, Au) and elements on their right in the Periodic Table (i.e. d^{10} s^xp^y

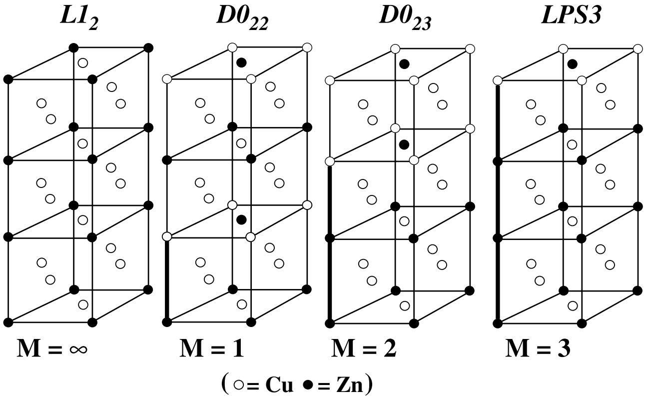

Figure 14. Schematic pictures of the compounds L1$_2$ (Cu_3Zn), D0$_{22}$ (Cu_3Zn), D0$_{23}$ (Cu_6Zn_2) and LPS3 (Cu_9Zn_3). The latter three 'long-periodic SL' (LPS) can be constructed from L1$_2$ by antiphase boundaries along [001] with modulation wavelength $M = 1$, 2 and 3, respectively.

elements with full d-bands), the d-band of the solute atoms lies far below the Fermi level and thus its influence on the Fermi electrons on alloying is negligible. During alloying, the kinetic energy of the free electrons is lowered due to the formation of a gap at the Brillouin zone boundary by the introduction of an extra period characteristic of the ordered compound formed. Since this mechanism depends only on the valence electrons, the structure formed is uniquely defined by e/a. Based on this ansatz, investigations by Sato and Toth [140] predicted a long-periodic superlattice (LPS) as a possible ground state for Cu_3Zn. This is created from the L1$_2$ structure by antiphase boundaries with a periodicity of a certain number of L1$_2$ unit cells along the [001] direction (figure 14). More quantitative attempts to predict the structure of α- and α'-brass were carried out [69, 141–143] using the CPA [69, 145]. So, Johnson *et al* [141] calculated the equilibrium lattice parameter of fcc-disordered $Cu_{1-x}Zn_x$ (finding a small deviation from Vegard's rule) and mixing enthalpies. With the structures of disordered (α) and ordered (α') phases of brass being a many decades old, yet unsolved, fundamental problem in alloy theory, we attempt here a solution by applying the MSCE combined with MC simulations: starting with a random configuration at a temperature far above the solidus line, the temperature is stepwise reduced until no more exchange processes between Cu and Zn atoms take place. The procedure has to be repeated for different cell sizes, temperature grids and number of MC-steps per temperature to minimize the possibility of being stuck in a local minimum.

Figure 15 shows the thus found lowest energy structure obtained by MC simulated annealing of the LDA energy functional of equation (MSCE), out of about $10^{15\,600}$ possible configurations. The structure can be identified as D0$_{23}$ (Cu_6Zn_2), as already suggested earlier from experimental studies by Reinhard *et al* [139]. It can be viewed as a SL consisting of L1$_2$ and a translated L1$_2$ structure (L1$'_2$) as shown in figure 14: D0$_{23}$ is constructed from L1$_2$ by forming an antiphase boundary after every two lattice constants in the [001] direction, i.e. the modulation period M of the structure with respect to L1$_2$ is $M = 2$, as visualized in the lower part of figure 15 [144].

The identification of a certain compound of the LPS group by its formation enthalpy is a very delicate task, because there are only a few interactions that differ for different LPS structures. Table 4 gives the total number of neighbours for the first eight neighbour distances in an fcc lattice and how much of these neighbour bonds are built by unlike atoms for different

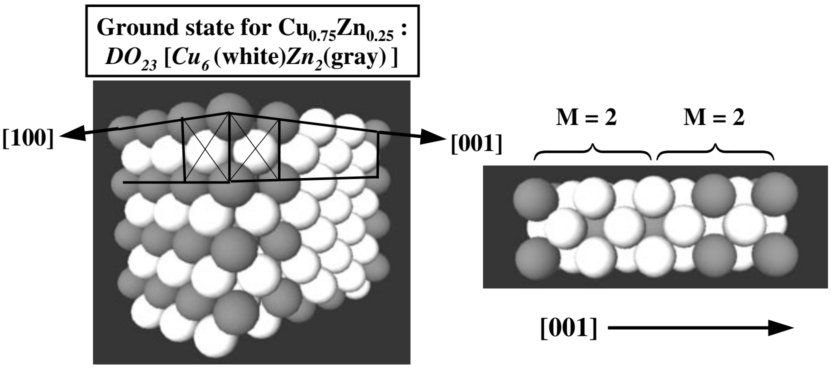

Figure 15. Result of the ground-state search by MC annealing [144]: the ground state found is a perfectly ordered $D0_{23}$ SL, characterized by a modulation wavelength of $M = 2$ between antiphase boundaries along [001].

Table 4. Number of neighbours, corresponding distance (in units of fcc lattice constants) and number of neighbouring pairs consisting of different chemical species for the $L1_2$, $D0_{22}$, $D0_{23}$ and LPS3 structures.

			No. of B atoms around A			
Neighbour	Total no. of neighbour atoms	Distance (a)	$L1_2$	$D0_{22}$	$D0_{23}$	LPS3
1st	12	$1/\sqrt{2}$	12	12	12	12
2nd	6	1	0	2	1	1
3rd	24	$\sqrt{3/2}$	24	16	20	20
4th	12	$\sqrt{2}$	0	8	4	4
5th	24	$\sqrt{5/2}$	24	24	24	24
6th	8	$\sqrt{3}$	0	8	4	4
7th	48	$\sqrt{7/2}$	48	48	48	48
8th	6	2	0	0	2	1

members of the LPS group. If we count the number of B atoms for a given A atom at the origin, the first difference between $D0_{23}$ and LPS3 occurs for the 8th (!) neighbour distance. Consequently, differences in the formation enthalpies between LPS structures often amount to only a few meV/atom. So, calculations of ΔH_f for the LPS group via DFT demand extremely strict convergence criteria regarding plane-wave basis, k-point set and geometric relaxations. As we have recently shown [144], a large number of pair and multi-body interactions are necessary to construct a stable MSCE that properly considers the delicate energy balance between the various competing phases of Cu_3Zn. The consideration of less than 10 pair interactions would even lead to a wrong ground state, as experienced in earlier CPA studies where the stable structure obtained for Cu_3Zn at $T = 0$ was $L1_2$ [142], which is inconsistent with the measured [139] SRO (see the next section). Nevertheless, these earlier calculations of Turchi *et al* [142, 143] signalled already the propensity of developing some long-periodic superstructures at low temperatures. Figure 16(a) compares the energies of the long-period SL E_M versus M for Cu_3Zn and Cu_3Pd, whereby values for Cu_3Pd are taken from Lu *et al* [89]. In excellent agreement with the LDA calculated formation enthalpies of Cu_3Zn (shown as open squares) our prediction locates a minimum for $M = 2$, corresponding to the $D0_{23}$ structure. Lu *et al* [89] found for Cu_3Pd the $M = 3$ structure as the most stable structure of the LPS group. We see that with increasing M the formation enthalpies are nearly energetically degenerated.

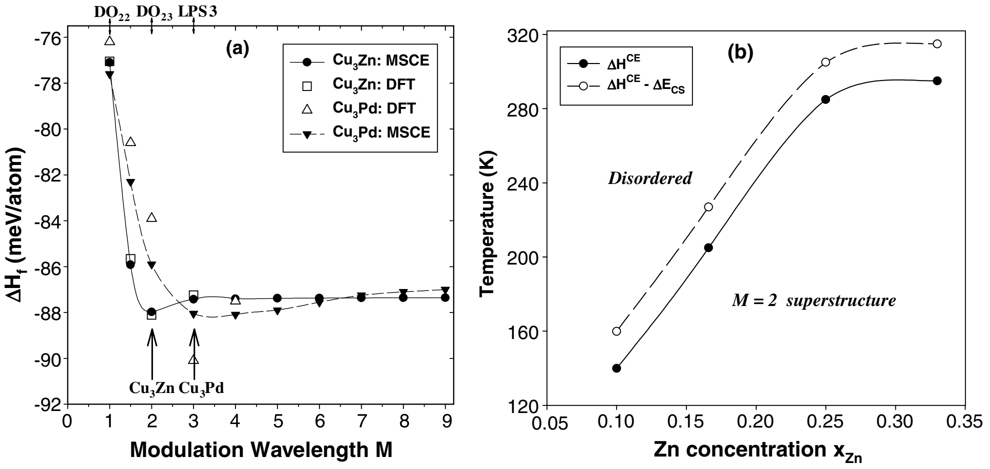

Figure 16. (a) Direct (DFT-LDA) and via MSCE calculated formation enthalpies for the LPS group of Cu_3Zn and Cu_3Pd. (b) Coherent phase boundary in α-brass calculated with (full curve) and without (broken curve) taking the constituent strain energy, ΔE_{CS}, into account [144].

Indeed, different experimental investigations on Cu_3Pd alloys [146–148] report the coexistence of LPS structures in the Cu–Pd alloy system with practically arbitrary modulation wavelength.

The question remains why the predicted $D0_{23}$ ground-state structure up to now was not observed experimentally as an ordered phase for $x_{Zn} = 0.25$. One possibility would be that the system disorders already at very low temperatures. To test this, we calculated the coherent phase boundary, which separates the ordered $M = 2$ SL from the disordered alloy (figure 16(b)). As discussed in section 3.2, this phase boundary (full line) can be identified by MC simulated annealing, recording the specific heat c_v as a function of temperature. We see that, indeed, the transition temperatures are very low on the scale of growth temperatures (usually of the order of 10^3 K). Thus, it might be difficult to detect the ordered phase directly. In section 4.2 we will see how the SRO behaviour of the disordered phase close to this phase boundary can help to verify the correctness of our prediction.

In order to study the importance of the constituent strain energy, ΔE_{CS} (equation (22)) for the stability of the found LRO phase, we switched ΔE_{CS} off in equation (21) and repeated our MC simulations to determine the coherent phase boundary again. The resulting curve is shown as a broken line in figure 16(b). We see that $\Delta H_{CE} - \Delta E_{CS}$ leads to about 20 K higher transition temperatures, while the two curves are practically parallel, i.e. the temperature difference between them is rather independent from the Zn concentration. The behaviour is understandable in terms of the ordering energies, δE_{ord}, given by

$$\delta E_{\mathrm{ord}} = \Delta H_{\mathrm{ord}} - \Delta H_{\mathrm{rand}}. \tag{44}$$

Here, ΔH_{ord} and ΔH_{rand} are the formation enthalpies, equation (6), of an ordered compound and a random alloy, respectively, at the same composition. As shown by Zunger *et al* [70], the formation enthalpy of a random alloy can be successfully described by so-called 'special quasirandom structures' (SQS). For the following estimation, we will use the formation enthalpy of SQS14a (Cu_6Zn_2) as the formation enthalpy of the random alloy for $x_{Zn} = 0.25$. Using our CE Hamiltonian, equation (21), this leads to an ordering energy

$$\delta E_{\mathrm{ord}} = \Delta H_{D0_{23}} - \Delta H_{\mathrm{SQS14a}} = -33.1\ \mathrm{meV/atom},$$

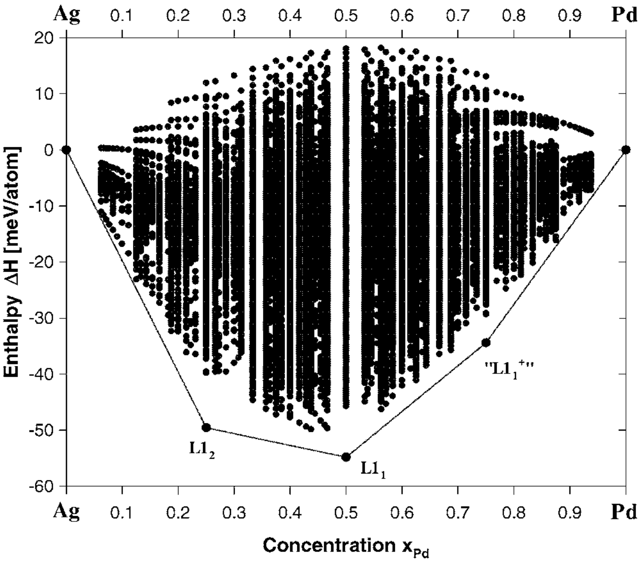

Figure 17. Ground-state diagram of Ag–Pd resulting from a grid search considering all possible structures with up to 16 basis atoms. The result is identical to the ground-state diagram received via MC annealing [161].

while a neglect of constituent strain energies leads to

$$\delta E_{\mathrm{ord(no\text{-}strain)}} = (\Delta H_{D0_{23}} - E_{\mathrm{CS}}(D0_{23})) - (\Delta H_{\mathrm{SQS14a}} - E_{\mathrm{CS}}(\mathrm{SQS14a}))$$
$$= -39.4\ \mathrm{meV/atom}.$$

So, neglecting strain leads to a more negative ordering energy and therefore to a more stable $\mathrm{D0_{23}}$ structure. Consequently, the coherent phase boundary will shift to higher temperatures.

If the ground-state search is carried out for the whole concentration regime, we can construct the full ground-state diagram for the alloy system. A prerequisite for such a construction is the existence of a coherent phase between the two constituents for any arbitrary concentration. Such a situation is given in the fcc-based alloy system Ag–Pd: experimentally [23, 25, 26, 149], Ag–Pd is known to form mutually miscible disordered solid solutions down to ~800 K, but no experimental studies exist at lower temperatures to reveal whether the system will phase-separate or order. The measured [23, 151] mixing enthalpy of the high-temperature disordered alloy is negative, indicative of ordering. Theoretical studies, however, found contradictory results: ordering [89, 152–154] as well as phase-separating tendencies [155, 156] are reported. Additionally, there is a long discussion on the importance of the d bands [157, 158] on the properties of Ag–Pd alloys, such as resistivity and SRO [159, 160]. Pettifor's [9] structure map (section 2) predicts no ordered structure for $x = 0.50$ and 0.75, but the $\mathrm{L1_2}$ structure for $\mathrm{Ag_3Pd}$, while Zunger's orbital radii method [10] predicts ordering at $x = 0.50$.

Analogous to the Cu–Zn studies, we apply the CE, equation (21), to an extensive $T = 0$ ground-state search via the MC simulated annealing method for Ag–Pd. A concentration grid with 5% step width plus $x_{\mathrm{Pd}} = 1/3$ and 2/3 were used for the ground-state search. We then constructed the convex hull (E versus x) to ensure that the predicted ground state at each x is stable with respect to the disproportionation into two structures with $x_1 \leqslant x \leqslant x_2$ as discussed in section 3.2. Again, the annealing process is repeated for different simulation conditions (e.g. different MC cells with up to about $30 \times 30 \times 30 = 27\,000$ sites and up to 10 000 MC

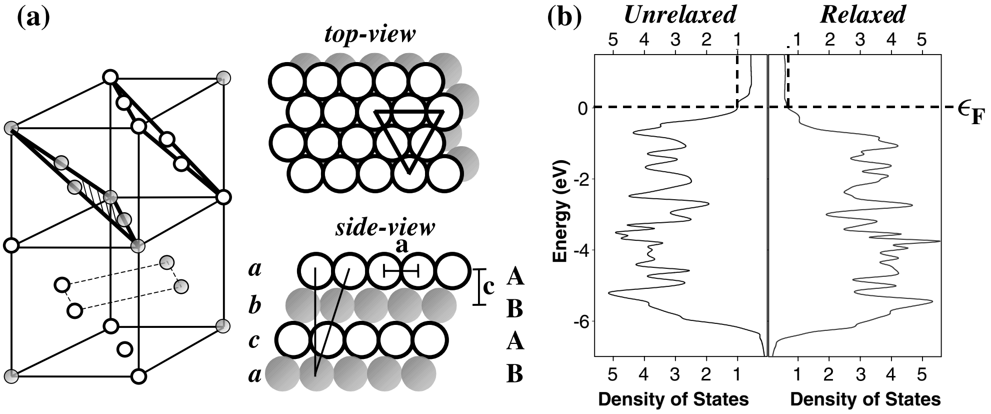

Figure 18. (a) The $\mathrm{L1_1}$ structure is equivalent to a SL of alternating A- and B-atom layers along the [111] direction. The geometric layer stacking sequence is, however, 'abc', characteristic for the fcc(111) orientation. (b) Total DOS of the unrelaxed ($c/a = 1$) and relaxed ($c/a = 1.04$) $\mathrm{L1_1}$ structure of the system Ag–Pd.

steps per temperature, different initial configurations and different temperature grids) to ensure that the result is stable. Beside the final configuration ($T \to 0$) and its formation enthalpy, the corresponding correlation functions were stored for identification and comparison with those of thousands of well-defined intermetallic compounds. We found three LRO ground states for Pd concentrations $x_{\mathrm{Pd}} = 0.25, 0.50, 0.75$. For $x_{\mathrm{Pd}} = 0.25$, $\mathrm{L1_2}$ is the most-stable structure (see figure 14), while for $x_{\mathrm{Pd}} = 0.50$, the $\mathrm{L1_1}$ structure $[(\mathrm{Pd})_1/(\mathrm{Ag})_1(111)$ SL] is found to be the ground state (this structure will be discussed in detail and is shown in figure 18(a)). The compound found for $x_{\mathrm{Pd}} = 0.75$ lacks a special name. It represents a $(\mathrm{Ag_{0.5}Pd_{0.5}})_1/(\mathrm{Pd})_1$ SL along [111]. The Pd and Ag atoms in the $\mathrm{Ag_{0.5}Pd_{0.5}}$ (111) layer form an in-plane c(2 × 2) superstructure. Because of the *additional* Pd atoms in the Ag(111) layers compared to $\mathrm{L1_1}$, we may call this compound $\mathrm{L1_1^+}$. Whereas this structure is only 3 meV below the AgPd $\mathrm{L1_1}$ and fcc Pd tie-line, its appearance as a ground state is a robust feature of our LDA and CE fits [161].

In order to put our results on even safer ground, we chose an alternative way to determine the ground-state line. Instead of applying MC simulated annealing in order to take a large number of structures into account, we restrict the search to compounds with a very limited number of basis atoms and calculate the formation enthalpy of *all possible configurations* via the MSCE Hamiltonian (for technical details, see section 3.2). For Ag–Pd we checked for all configurations with up to 16 basis atoms. This restriction still allows for more than about 130 000 structures, a number which could never be treated by direct DFT calculations for all compounds. The MSCE Hamiltonian permits us to calculate the formation enthalpies of *all* these geometrically fully relaxed structures within a few hours on a high-performance workstation. The resulting ground-state diagram is shown in figure 17. We see that the constructed ground-state line is formed by exactly those three structures which were already detected as ground states via MC annealing.

The most surprising result of our ground-state search is the prediction of the $\mathrm{L1_1}$ structure for low temperatures, since up to now the only binary metal alloy system known possessing $\mathrm{L1_1}$ as a ground state is the Cu–Pt alloy system [24]. This structure is sketched in figure 18(a). While the geometric layer stacking is 'abc', characteristic for fcc(111), the chemical stacking is 'AB'. The question arises, how can this unsuspected result be explained *ex post facto*. Clark *et al* [150] described the existence of the $\mathrm{L1_1}$ structure in Cu–Pt by a coupling between electronic states at L and X Van Hove singularities at the Fermi level, ϵ_F. Furthermore, they suggest that $L1_1$ is stabilized over $L1_0$ by the fact that at the Fermi level the d-electron density of states (DOS) is lower for the $L1_1$ than for the $L1_0$ structure. Indeed, we find that the DOS of $L1_1$-AgPd at ϵ_F is about 20% lower than that of the $L1_0$ structure, in accordance with the 22 meV/atom lower formation enthalpy of $L1_1$ over $L1_0$. However, this result holds only for the *atomically relaxed* structures. For *atomically unrelaxed* structures, the formation enthalpy of $L1_1$ is *still lower* than that of $L1_0$ (by 15 meV/atom), but the DOS at ϵ_F are practically equal. So, in the case of Ag–Pd, for the unrelaxed systems the DOS argument is not sufficient for the stability of $L1_1$, but only a stability supporting factor. Help comes by analysing individual energy parts: we may separate the structure-dependent energy part of the total energy into the electrostatic energy (often referred to as 'Madelung energy' or 'Ewald energy') and the band-structure energy. The former is given by the Coulomb energy of the nuclei system plus the homogeneous electron gas. It turns out that for $Ag_{0.5}Pd_{0.5}$ even for the unrelaxed c/a ratio the Madelung energy amounts to about 400 meV/atom (!) lower for $L1_1$ than for $L1_0$. Although all remaining energy parts (e.g. the Hartree term) are clearly higher in energy for $L1_1$ than for $L1_0$, they cannot compensate for this large difference in the Madelung energy. A relaxation of c/a now additionally causes a reduction of the total DOS below the Fermi level and therefore to a further energy decrease. This behaviour is demonstrated in figure 18(b), giving the DOS for $L1_1$ with and without a relaxed c/a ratio (note that both DOS were smoothed). Interestingly, we also found for the $L1_1^+$ ($x_{\mathrm{Pd}} = 0.75$) ground-state structure that the d band is pushed below the Fermi level, different to, for example, the $L1_2$ ($AgPd_3$) structure, for which the opposite is true. This probably stabilizes $L1_1^+$ over $L1_2$ for $x_{\mathrm{Pd}} = 0.75$. The discussion also makes clear that, although the relaxation in $L1_1$ only leads to an 8 meV/atom more negative formation enthalpy, this small energy difference can already profoundly influence the predicted ground-state diagram, figure 17, where many formation enthalpies of structures differ by less than 5 meV/atom. Therefore, relaxations are essential for a correct description of phase stability [161].

The critical temperatures corresponding to the maximum of the coherent phase boundaries separating disordered alloys and low-temperature ordered compounds were also calculated from MC simulations to be $T_c = 340$, 320 and 270 K for $x = 0.25, 0.50, 0.75$, respectively, and therefore far below the solidus line ($T = 1235$ K for $x \to 0$ and $T = 1828$ K for $x \to 1$) [26]. These low transition temperatures explain why, up to now, the three structures were not observed experimentally. Unfortunately, there are also no SRO measurements for the random alloy at higher temperatures. The determined coherent phase boundaries allow for the construction of a new phase diagram for the system Ag–Pd as schematically shown in figure 19. It now includes three low-temperature LRO phases with critical temperatures at $x_{\mathrm{Pd}} = 0.25$, 0.50 and 0.75.

The predicted LRO Ag–Pd structures represent not only an important addition to the phase diagram of the system, but may also significantly influence mechanical and electronic properties in the low-temperature regime. Unfortunately, an experimental proof of the existence of these compounds is still lacking, probably due to the low transition temperatures between low-temperature compounds and disordered alloys. There is, however, one possibility left for checking the quality of the expanded interactions: the prediction of SRO and mixing enthalpies which will be discussed next.

4.2. Short-range order and mixing enthalpy

In the last section, we have seen that one of the major problems in predicting low-temperature ground states is the missing direct experimental evidence, because often the order–disorder transition takes place at temperatures far too low for any real crystal to grow. Since we claim

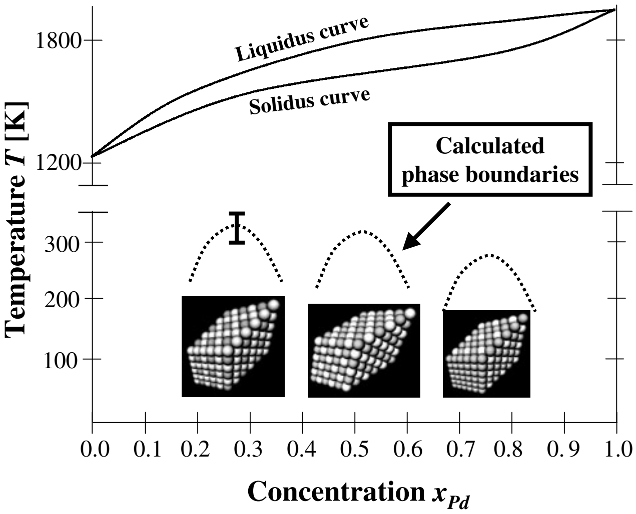

Figure 19. Schematic phase diagram for Ag–Pd including the three predicted LRO phases at low temperature. The calculated phase boundaries are also shown.

that our constructed effective pair and multi-body interactions are universal in the sense that they can be applied for all temperature regimes, we should be able to describe SRO and mixing enthalpies with an accuracy large enough to make a quantitative comparison with experiment possible. Then, a successful prediction of experimentally observed SRO by applying the *same* interactions which were used for the ground-state analysis would strongly support the validity of our ground-state diagram at $T \to 0$ K. Here, we will only focus on two characteristic examples, namely an ordering system (Cu–Zn) and a phase-separating system (Al–Zn).

Coming back to the old question whether there is a LRO phase in α-brass, we face that diffuse intensity measurements via neutron diffuse scattering clearly show diffuse intensities around well defined positions in the Brillouin zone for SRO [139]. The measured SRO pattern is shown on the right side of figure 20. The experiments apply to a sample with a Zn concentration of 31.1% at $T = 200\,^{\circ}\mathrm{C}$. For $x_{\mathrm{Zn}} = 0.311$, the difference between transition temperature (~10 °C) and experimentally used temperature (~200 °C) is small compared to smaller Zn concentrations so that the observed SRO should be characteristic for $\mathrm{D0}_{23}$. The experimental pattern indeed clearly shows SRO intensities around $\boldsymbol{k} = \langle 1\frac{1}{4}0\rangle$. Since the LPS group introduced in section 4.1 possesses the fundamental reciprocal space wavevector $\boldsymbol{k} = \langle 1\frac{1}{2M}0\rangle$ with M being the modulation wavelength, we see the highest intensity for the LPS structure with $M = 2$. As is known from figure 14, this is exactly the modulation wavelength of the $\mathrm{D0}_{23}$ structure which was predicted as the low-temperature state in α-brass. The pattern is in very good agreement with that resulting from our calculation (figure 14).

For a quantitative comparison of the computed SRO with experiment, we calculated the Warren–Cowley SRO parameter α_{lmn} (equation (27)) for the first 16 shells of an $\mathrm{Cu}_{0.689}\mathrm{Zn}_{0.311}$ alloy at $T = 473$ K and compared the values to those obtained from neutron scattering experiments [139] as shown in table 5. Considering the fact that the experimental error of α_{000} amounts to be as large as 8% (since $\alpha_{000} = 1.000$ by definition) and that the authors give about the same error also for all further parameters, the predicted and experimentally determined values agree very well. We see that α_{110} is negative, indicating that Zn atoms prefer Cu atoms as nearest neighbours. Furthermore, all α_{2n00} are positive, while all $\alpha_{(2n-1)10}$ are negative.

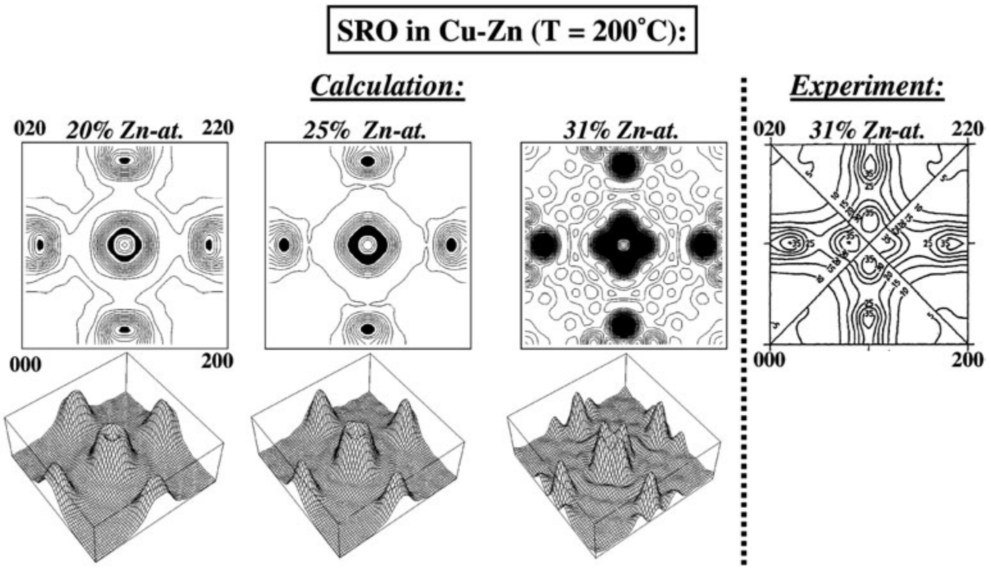

Figure 20. SRO pattern and corresponding contour plot for Cu–Zn solid solutions with different concentrations. For $x_{\mathrm{Zn}} = 0.31$ the SRO intensity pattern resulting from neutron diffraction experiments [139] is shown for comparison with our calculation. In both cases, SRO peaks around $\langle 1\frac{1}{4}0\rangle$ are visible, favouring $D0_{23}$ as the low-temperature ground state.

Table 5. Warren–Cowley SRO parameter α_{lmn} resulting from our calculations and from experimental studies [139] for $Cu_{0.689}Zn_{0.311}$ at $T = 473$ K.

(lmn)	$\alpha_{lmn}^{\mathrm{exp}}$	$\alpha_{lmn}^{\mathrm{theo}}$	(lmn)	$\alpha_{lmn}^{\mathrm{exp}}$	$\alpha_{lmn}^{\mathrm{theo}}$
000	1.0831	1.0000	400	0.0296	0.0279
110	−0.1373	−0.1689	330	−0.0134	−0.0211
200	0.1490	0.1863	411	0.0141	0.0306
211	0.0196	0.0196	420	0.0050	0.0825
220	0.0358	0.0883	332	−0.0005	−0.0050
310	−0.0404	−0.0453	422	−0.0050	−0.0050
222	−0.0077	0.0371	431	0.0068	0.0148
321	−0.0036	−0.0132	510	−0.0107	−0.0186

The concentration dependence of the SRO intensities for $T = 200\,^{\circ}\mathrm{C}$ is also shown in figure 20. For a concentration $x_{\mathrm{Zn}} = 0.31$, the temperature chosen comes closest to the transition temperature T_{trans} ($T \approx 1.55T_{\mathrm{trans}}$) compared with the other two concentrations, so characteristic SRO peaks around $\langle 1\frac{1}{4}0\rangle$ become visible. For $x_{\mathrm{Zn}} = 0.20$, the SRO peaks are no longer exactly on $\langle 1\frac{1}{4}0\rangle$ positions, but are displaced to $\langle 1\frac{1}{6}0\rangle$. This could be a consequence of 'missing' Zn atoms (the concentration is now smaller than 25%) so that, on average, the modulation wavelength M has to be increased and therefore the SRO peaks are shifted towards $\langle 100\rangle$.

In experiment, the SRO parameters, table 5, were used to construct a real-space image of the alloy by using them as input for an inverse MC approach in order to obtain characteristic interactions [139]. In the case of α-brass, real-space images are of special interest for the following reason: as already mentioned, and apparent from table 5, all SRO parameters described by $(lmn) = (2n; 0; 0)$ are positive, while all SRO parameters described by $(2n-1; 1; 0)$ are negative. This property should lead to characteristic chains of Zn atoms along

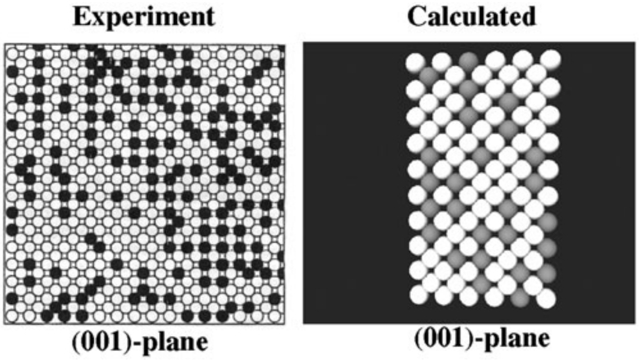

Figure 21. Visualization of a (001) plane of α-brass (cut through the crystal) for $T = 473$ K. While the left pictures result from a model crystal based on diffuse neutron scattering experiments [139], the right picture is the result of MC simulations using ΔH_{CE}. In both cases, chains of Zn atoms along [100] can be seen, indicating that SRO is present and therefore the observed solid solution cannot be described by a random alloy.

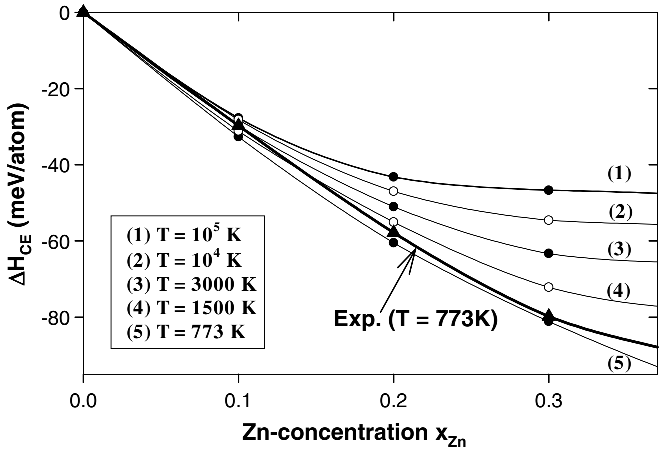

Figure 22. Calculated mixing enthalpies of α-brass for different temperatures [144] and comparison with experimental data [23] (bold curve).

the [100] direction. Figure 21 compares the real-space structure deduced from experiment [139] and from our ‘CE plus MC’ calculation. In both cases, chains of Zn atoms are visible along [100], indicating that SRO is essential for a quantitative correct description of the physical properties of the disordered solid solution of α-brass. Moreover, the type of SRO is consistent with the predicted $D0_{23}$ ground state in section 4.1.

Since SRO plays an important role in α-brass, it should also influence its energetics, i.e. the mixing enthalpy of the system should possess a temperature dependence. To clarify this, figure 22 compares calculated mixing enthalpies, $\Delta H_{\mathrm{mix}}(x, T)$, for different temperatures with experimental data taken from Hultgren’s book [23]. We start with the random alloy ($T \rightarrow \infty$) and go down to temperatures where SRO sets in. Comparing the energy curves for the random and disordered alloy, we see that the calculation neglecting SRO leads to much higher mixing enthalpies. For higher Zn concentrations a good agreement between experiment and calculated mixing enthalpies can only be reached if SRO is taken into account.

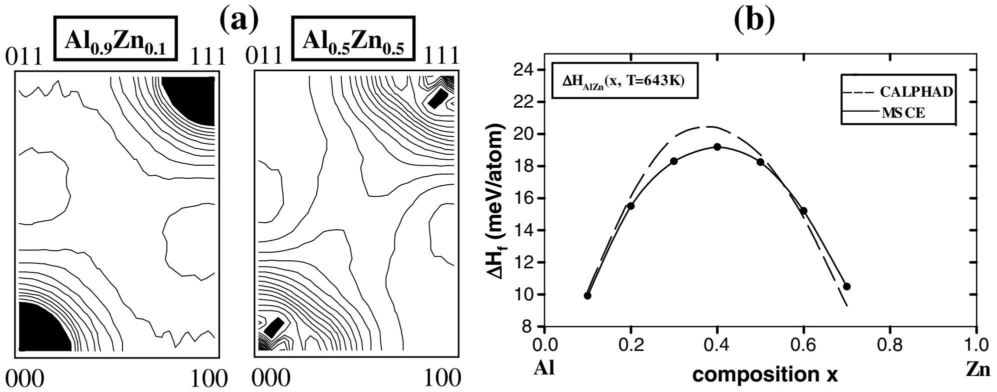

Figure 23. (a) SRO maps of $\mathrm{Al_{0.9}Zn_{0.1}}$ (left) and $\mathrm{Al_{0.5}Zn_{0.5}}$ (right). Peaks are at Γ and streaks in the SRO intensity along $\langle 111\rangle$ are visible. Clustering tendencies are clearly stronger for 10% than for 50% Zn, resulting in a higher intensity value around the Γ point for $\mathrm{Al_{0.9}Zn_{0.1}}$. A temperature of $T = 700$ K was chosen. (b) Calculated mixing enthalpy ΔH of $\mathrm{Al}_x\mathrm{Zn}_{1-x}$ at $T = 643$ K as a function of composition. The broken curve shows the result of a study using CALPHAD [162], while the full curve is our calculated first-principles mixing enthalpy $\Delta H_{\mathrm{AlZn}}(x, 643K)$.

In summary, the alloy is stabilized at low temperatures by deviating systematically from randomness: it eliminates unlike-atom first-neighbour pairs and enhances unlike-atom second-neighbour pairs.

An important point for the characterization of alloy systems is that the phenomenon ‘SRO’ is by no means restricted to ordering systems. Analogous to ordering tendencies in a solid solution like α-brass as discussed above, a solid solution may also form small atomic clusters of identical atoms. As an example, we consider the metal alloy system Al–Zn. The SRO of $\mathrm{Al}_x\mathrm{Zn}_{1-x}$ solid solutions was calculated for two different Zn concentrations, namely 10 and 50% Zn at $T = 700$ K (figure 23(a)). It should be noted that the patterns take the fact into account that the distance between $\langle 000\rangle$ and $\langle 011\rangle$ is larger by a factor of $\sqrt{2}$ than the distance between $\langle 000\rangle$ and $\langle 100\rangle$. The SRO in $\mathrm{Al_{0.5}Zn_{0.5}}$ shows diffuse intensity at $\Gamma = \langle 000\rangle$, with streaks along $\langle 111\rangle$. The SRO at Γ is indicative of a clustering tendency in the solid solution, consistent with the miscibility gap in the Al–Zn phase diagram and the experimentally observed positive formation enthalpies [23]. The streaking of the SRO along $\langle 111\rangle$ is a ‘fingerprint’ (see Al–Zn CE, table 2 of the energetic preference for SL along [111] from the CE, table 2). We also see that, especially for a concentration of 50% Zn, the formation enthalpies of [111] SL are unusually small, sometimes only 1–5 meV/atom less stable than phase separation. The SRO behaviour of Al–Zn alloys in the solid solution is also interesting since it can manifest itself at low temperatures in precipitation experiments. Ageing of Al–Zn alloys show [111] faceting of Zn precipitates as well as a crossover at a critical particle size from spherical to oblate ellipsoid, with the short axis in the [111] direction. We will discuss this subject in the next section. Upon going to Al-rich compositions, the SRO of $\mathrm{Al_{0.9}Zn_{0.1}}$ also peaks at Γ, but the streaking along the $\langle 111\rangle$ direction is diminished. This reduction of the $\langle 111\rangle$ streaks for Al-rich compositions is a consequence of the fact that formation enthalpies of SL along the [111] direction become larger (corresponding to less stable structures) with increasing Al concentration.

The concentration dependence of the mixing enthalpy in Al–Zn was calculated for a temperature $T = 643$ K, because studies performed by Mey [162] for exactly these temperatures opens the possibility for a direct comparison. This earlier investigation is not based on first-principles calculations, but used a polynomial description which was adjusted to fit all available *experimental information* using a least squares program (CALPHAD I [163]). In that sense these calculations give an 'average' mixing enthalpy, i.e. averaged with respect to many experimental values for $\Delta H_{\mathrm{AlZn}}(x, 643\ \mathrm{K})$. The calculation was made for the fcc solid solution relative to its fcc constituents, i.e. the fcc–hcp energy difference for Zn was already subtracted (note that Zn normally possesses an hcp lattice, while in the Al–Zn solid solution it is forced to have a fcc structure). Our calculated first-principles mixing enthalpy $\Delta H_{\mathrm{AlZn}}(x, 643\ \mathrm{K})$ and the fit to experiment of Mey [162] are compared in figure 23(b). The two curves agree very well: they show a maximum around 40% Zn with a corresponding mixing enthalpy of about 20 meV/atom. A comparison to individual experimental studies of the fcc phase appears to be very difficult, because their results differ profoundly: for example, while calorimetric studies of Wittig and Schöffl [164] ($T = 643$ K) and Connel and Downie [165] ($T = 637$ K) lead to a maximum in the mixing enthalpy at about 25% Zn, electromagnetic field studies by Hilliard *et al* [166] ($T = 653$ K) find a maximum around 60% Zn. To my knowledge, these discrepancies for the thermodynamic properties of the fcc solid solution are not yet clarified; hence, future experimental studies would be desirable.

4.3. Coherent precipitates

As already mentioned in section 3.3, solid state decomposition reactions like the phase separation of an alloy into its constituents, $\mathrm{A}_{1-x}\mathrm{B}_x \rightleftharpoons (1-x)\mathrm{A} + x\mathrm{B}$, create so-called precipitates which define an important part of the microstructure of many alloy systems. The early stage of these reactions typically involves the formation of *coherent precipitates* that adopt the crystallographic lattice of the alloy from which they emerge [120]. Coherent precipitates have practical relevance, as they impede dislocation motion and thus lead to 'precipitation hardening' in many alloys [120, 167–169]. Despite their importance, precipitate microstructures were thus far not amenable to first-principles theories, since their description requires 'unit cells' containing 10^3–10^6 atoms or more, well beyond the current capabilities of first-principles methods. The chemical and structural properties of precipitates are determined by the identity of the phases being located to the left and right of the two-phase region in the phase diagram. In the case of the phase-separating system Al–Zn, one of the prototype systems for studying coherent precipitates, the two-phase region corresponds to elemental Al and Zn, so that coherent precipitates formed from the Al-rich fcc-based solid solution consist of only Zn atoms. In experiments, the fcc-Zn precipitates are formed by quenching an Al-rich Al–Zn solid solution deep into the two-phase region of the phase diagram (typically ice-water is used), followed by sample ageing (typically at room temperature). The formed precipitates can then be observed via transmission electron microscopy (TEM) [170] as shown in figure 24. The black spots are coherent fcc-Zn precipitates.

Due to the ability of Al–Zn to harden via precipitate heat treatment the shapes and sizes of coherent precipitates are of particular interest. Therefore, a number of experimental studies have been performed [170–176] to learn more about the size–shape relation of these microstructures. It turns out that for Al–Zn alloys these experiments agree very well with each other and lead to the following scenario: small precipitates tend to be spherical, until they reach a critical radius R_C of about 15–25 Å (dependent on the ageing temperature) at which point they become ellipsoidal/plate-like with the short axis parallel to the [111] direction. The transition radius R_C depends on the temperature: it shrinks as the ageing temperature is reduced. The observed flattening, which is always along [111], allows us to describe the shape of precipitates in a simple way: the shape obtained for a given average size $\bar{R} = (ca^2)^{1/3}$ and temperature T is measured by the ratio c/a between the short (c) and the long (a) axes of the precipitate, as schematically shown in figure 24, too. Such c/a ratios as a function of T and size

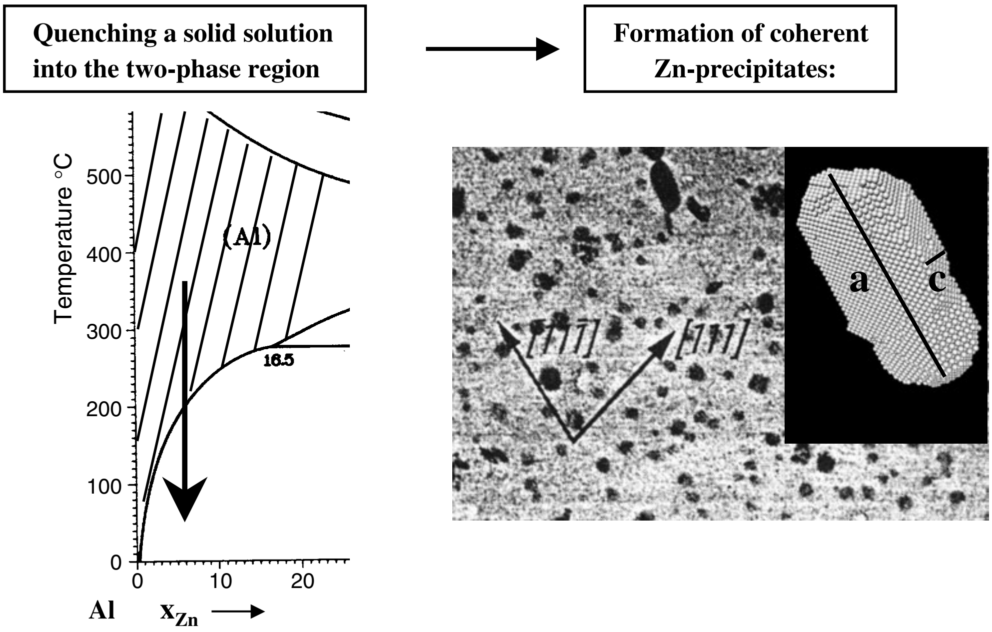

Figure 24. Quenching an Al-rich Al–Zn solid solution into the two-phase region of the phase diagram (left), followed by sample ageing, leads to the formation of Zn precipitates which can then be observed via TEM [170] in the form of black spots (right). The shape of the precipitates are then determined by the c/a ratio as schematically sketched in the TEM image.

were determined in an number of experiments [170–176]. While different ageing times lead to different distribution of sizes, remarkably the size–shape relation is universal, irrespective of whether the ageing period is minutes or weeks. In an atomistic sense, this observation raises the possibility that each individual precipitate represents locally an equilibrium configuration. Such local equilibria are a consequence of the fact that atoms in a single precipitate exchange more readily with each other than with other precipitates. Our strategy will henceforth be to *try* a *thermodynamic* (rather than a kinetic) ansatz to describe the size–shape relation and examine the extent to which the predicted relation does or does not agree with the measured relation of sizes and shapes.

To calculate equilibrium shapes of coherent precipitates we use the MSCE Hamiltonian, equation (21), in canonical ensemble MC simulations. In order to exclude boundary effects, unit cells containing up to $60 \times 60 \times 60 = 216\,000$ atoms were needed. We used fix boundary conditions so that boundary sites are always occupied by Al atoms. These atoms are 'frozen', i.e. cannot flip their identity. This restriction has the advantage that precipitates cannot grow over the cell boundaries. The MC annealing process is initialized at a sufficiently high temperature, where the solid solution is thermodynamically stable. Using a given number N_{Zn} of Zn atoms in the MC cell (hence, a given average precipitate size $\bar{R}$), the system is carefully annealed below the coherent fcc miscibility gap. Upon crossing this solvus, a coherent precipitate is formed. The MC cell size and number of spin flips are increased until the precipitate shape remains unchanged. At this point we record the final equilibrium configuration as a function of temperature.

Figure 25 shows calculated equilibrium shapes of coherent Zn precipitates for different temperatures and sizes. For clarity, *only the Zn atoms are displayed.* We see that

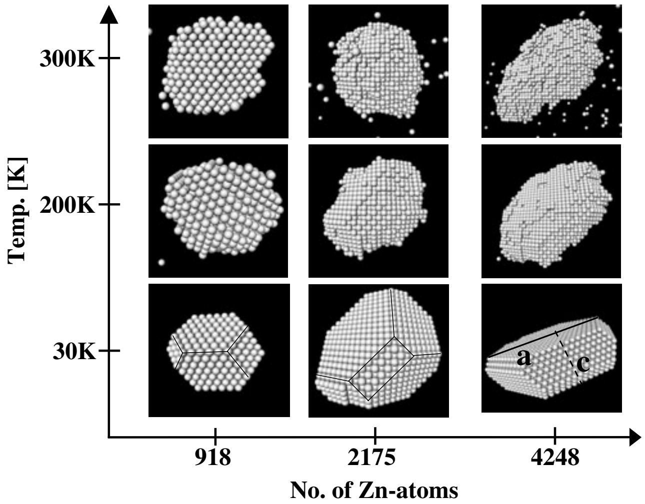

Figure 25. Dependence of the calculated coherent fcc Zn precipitate shape on the number of Zn atoms and temperature in Al–Zn alloys. The bottom right marks the *c* and *a* axes of the precipitate which can be used for a quantitative comparison with experimental data (only Zn atoms are shown).

(i) with increasing size and decreasing temperature precipitates become more ellipsoidal/hexagonal,
(ii) precipitates flatten with increasing size,
(iii) for very low temperatures precipitates show some faceting.

These observations are in qualitative accordance with experimental studies. Moreover, we also find that the short axis of the precipitates is *always* parallel to the [111] direction, in agreement with experiment. To critically assess these results *quantitatively*, figure 26 compares the measured [171, 172, 174–176] and calculated precipitate shapes (c/a) for two different temperatures. The experimental values correspond to $\mathrm{Al}_{1-x}\mathrm{Zn}_x$ alloys with $x = 0.068$ and 0.138 for $T = 300$ and 200 K, respectively. Our quantum-mechanical predictions were done for *exactly* these two concentrations and temperatures. The agreement is excellent: our thermodynamic theory accounts quantitatively for the change of the c/a ratio with size and temperature [177]. For samples aged at room temperature, c/a is nearly 1 up to about $r_m = 2$ nm (2175 Zn atoms). Then, the c/a ratio starts to decrease, e.g. for $r_m = 3.5$ nm (11 660 Zn atoms), $c/a = 0.5$. For a given size $r_m = (ca^2)^{1/3}$, the ratio c/a can only be changed by lowering the ageing temperature: the lower the ageing temperature the smaller is the resulting c/a ratio. We conclude that, although the precipitates are created by an inherently kinetic heat treatment process, the entire series of their size–shape relation can be explained in terms of *thermodynamic* arguments. Furthermore, first-principles theory can *predict* the size–shape relation within experimental accuracy.

To shed more light into the shape-controlling factors, the MSCE Hamiltonian, equation (21), is separated into physically motivated parts as the chemical energy (E_{chem}) containing all the information about different pair and multi-body interactions, and the constituent strain energy, E_{CS}. Naturally, this separation is not unique, but will allow us to discuss and understand which energetic factors control the precipitate equilibrium shape. We annealed an $\mathrm{A}_{24\,825}\mathrm{Zn}_{2175}$ supercell, but this time, instead of applying the *full* Hamiltonian in the MC simulation, we used only the constituent strain energy E_{CS} and the chemical energy

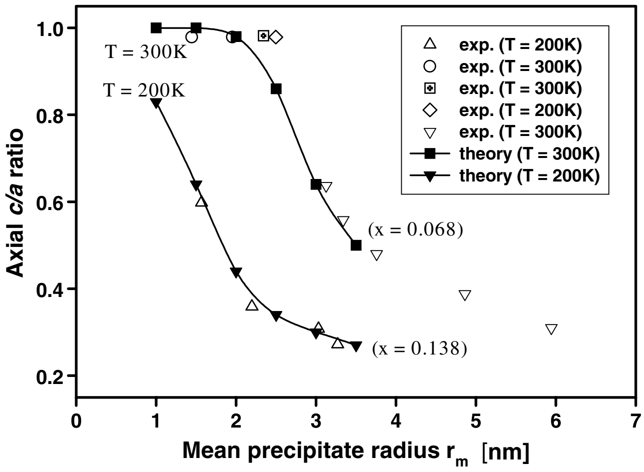

Figure 26. Shape (c/a) versus size relation of Zn precipitates for two different temperatures. The mean precipitate radius r_m is given by $r_m = (ca^2)^{1/3}$. The lines denote the results from our calculations [177] and the open points are taken from different experimental studies [171, 172, 174–176].

E_{chem} separately. If we only use the strain part E_{CS} in the simulation, we receive a flat layer, i.e. the strain part gives platelet stabilization with $c/a \to 0$. Thereby, the direction of the platelet is defined by the elastically softest direction of the material which forms the precipitate. Surprisingly, the resulting layer is oriented towards [111] and *not* [100], which is usually the softest direction for the fcc lattice. The reason is the following: Zn naturally is an hcp element, but in Al-rich $Al_{1-x}Zn_x$ alloys it is forced to adopt the fcc structure of the alloy. It thus develops an instability [94] in the form of an anomalously low energy for the [111]-deformed unit cell. This instability is demonstrated in figure 27 which compares the LDA-calculated total energies of uniaxially distorted fcc-Zn along the [100] and [111] directions. The calculations are volume-conserving, i.e. whilst the ‘basal’ plane lattice parameter a_p is varied, the distance d between layers is chosen so as to maintain the constant volume of the undistorted unit cell. The x axis gives the resulting d/a_p ratio with respect to ideal close-packing. While distortions along the [100] direction have an energy minimum at $d/a_p = 1$ (the ideal fcc cell), distorting fcc-Zn in the [111] direction leads to a new minimum around $d/a_p = 1.15$ lying 5.5 meV *below* the energy level of the ideal undistorted fcc-Zn unit cell. As a consequence, [111] is the elastically softest direction of fcc-Zn, resulting in extremely small (<1 meV/atom) coherence strain energies along this direction. These [111]-soft precipitates are embedded in a matrix of Al which has an elastically soft [100] direction. While the [100] softness of Al has been shown to yield spinodal decomposition fluctuations along this direction [178], it does *not* control the plate orientation of (relatively) large Zn precipitates due to the well-known result of Khachaturyan [168] that the habit plane of a precipitate is determined by the elastic constants of the precipitate phase, and *not* by those of the matrix.

Considering only the‘chemical part’ E_{chem} in the simulations leads to a compact, but *faceted* polyhedron. This faceting caused by the chemical part of the Hamiltonian is a consequence of a strong anisotropy of the chemical energy for Al–Zn. This chemical anisotropy is evident from the fact [94] that (111)-oriented Al_n/Zn_n SL have much lower chemical energies than SL of other orientations. This is reflected by the unusually strong directional dependence of the interfacial energies of Al_n/Zn_n SL, as already shown in figure 8: for SL along [201] the interfacial energies are an order of magnitude larger than for SL along [111]. Interestingly,

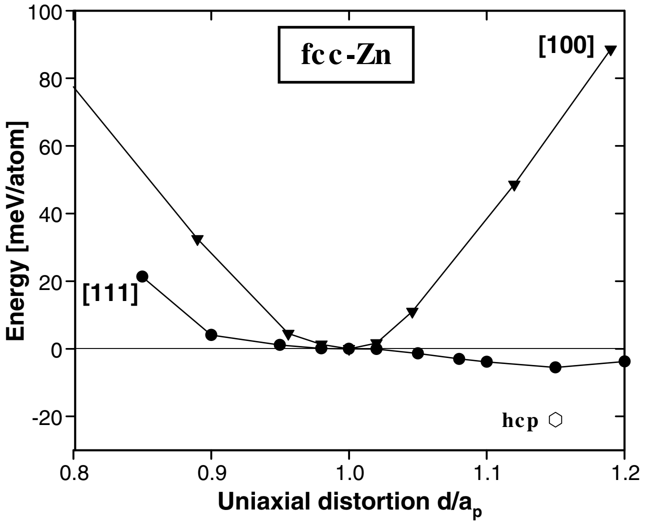

Figure 27. Volume-conserving first-principles total energy calculations of fcc-Zn deformed along different crystallographic directions. The energy differences caused by distortions along [100] and [111] as well as for hcp-Zn are always given with respect to the undistorted fcc lattice. The energy of hcp-Zn is denoted as an open hexagon.

the found ratio $d/a_p = 1.15$ at the energy minimum is identical to the well-known anomalous d/a_p ratio of hcp-Zn [94].

The conventional understanding [168] of spherical versus plate-like precipitate shapes is based on the balance between strain and interfacial (chemical) energies: as precipitates get larger, strain energies dominate over chemical energies and lead to plate-like shapes along the elastically soft direction. For small precipitates, chemical energies can dominate and hence lead to spherical shapes which minimize interfacial area. Here, we find that a third component becomes important: the *anisotropy of the chemical energy* which controls *quantitatively* to which extent the precipitates facet at low temperatures. Figure 28 shows equilibrium shapes resulting from calculations considering the chemical part only: at low temperatures, when entropy is unimportant, the strong anisotropy of the chemical energy creates facets along planes of low interfacial energy. These are mostly (100) and (111) planes whose interfacial energies are the lowest and practically degenerated (see figure 8). In contrast, at high temperatures, where many configurations coexist due to entropy, the chemical anisotropy is largely averaged out and therefore the precipitates become spherical, exactly as found in earlier theoretical studies that assumed simplified *isotropic* chemical terms [119]. However, the chemical part alone, while stabilizing facets, still leads to $c/a = 1$ (as shown by Herring [179], the equilibrium shape obtained from pure chemical interaction is determined by the Wulff construction which does not allow flattening). Indeed, no flattening can be observed in figure 28, because *only the constituent strain* E_{CS} *can produce* $c/a < 1$. Thus, the equilibrium c/a value at $T \to 0$ is dictated by the competition between E_{chem} (driving $c/a \to 1$) and E_{CS} (driving $c/a \to 0$).

One might think that the use of continuum elasticity plus empirical interfacial energies might have sufficed to study precipitate shapes in Al–Zn. However, the present studies show effects that are unsuspected, such as the large anisotropy of the interfacial energies and the critical role of the elastic constants of an unstable phase: fcc-Zn. Our approach provides both quantitative predictions as well as a microscopic picture for the variations in shape and size with temperature.

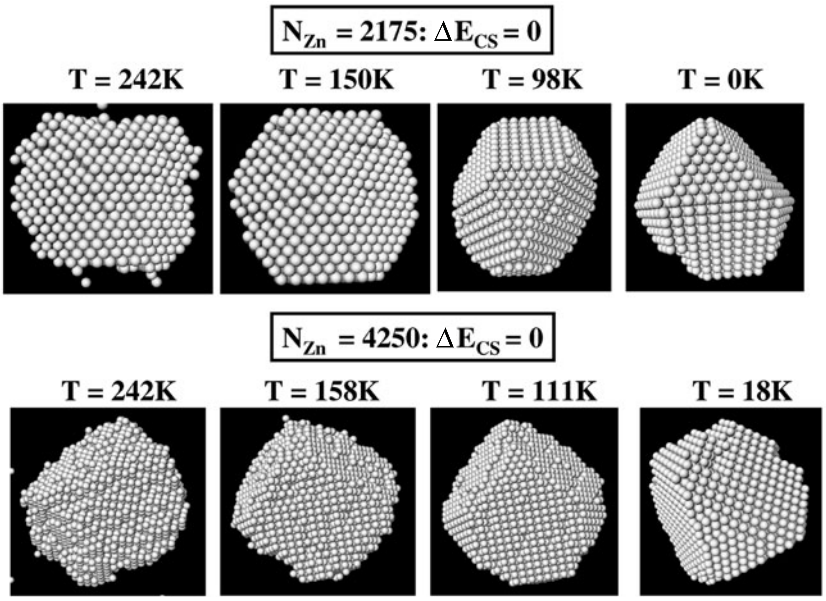

Figure 28. Equilibrium precipitate shapes for different temperatures and sizes resulting from calculations where the constituent strain energy was neglected. The size is given by the number of Zn atoms, N_{Zn}. For low temperatures, the faceting caused by the anisotropy of the chemical energy in Al–Zn becomes visible.

4.4. Non-equilibrium phenomena: ageing of microstructures

In the previous section we have seen that, although the precipitates are created by an inherently kinetic heat treatment process, the *size–shape relation* of fully developed precipitates ($t \rightarrow \infty$) can be explained in terms of *thermodynamic* arguments [46, 177]. However, the *distribution of precipitate shapes and sizes* at finite ageing time is controlled by *kinetics* as studied next. Indeed, the kinetic evolution of an alloy morphology is important for an understanding of how the final shape of the alloy develops. For our calculations we used the two kinetic MC algorithms discussed in section 3.3, whereby periodic boundary conditions are used. Additional to the thermodynamic properties, experimental investigations of the kinetic evolution of precipitates in Al–Zn alloys report the following behaviour [170, 180]:

(i) The distribution of precipitate shapes changes with ageing time: the longer the ageing time the less spherical and the more ellipsoidal the precipitates become.
(ii) The width of the distribution of precipitate shapes and sizes depends on the heat treatment. Lowering the ageing temperature leads to a broadening of the size distribution compared with higher ageing temperatures.
(iii) After the initial formation of precipitates within the first few seconds for a given temperature and concentration, the SRO parameters of the alloy only show a weak, but non-negligible, time dependence. We try to describe and understand these properties theoretically.

As a model system, we chose an $\mathrm{Al}_{0.932}\mathrm{Zn}_{0.068}$ alloy and a MC cell which consists of $56 \times 56 \times 56$ sites (a total of 175 616 atoms) containing a total of 11 942 Zn atoms. For the concentration of 6.8% Zn, the transition temperature (the temperature where precipitation occurs) was determined to be $T_{\mathrm{trans}} \approx 330$ K. Figure 29 shows the time evolution of the

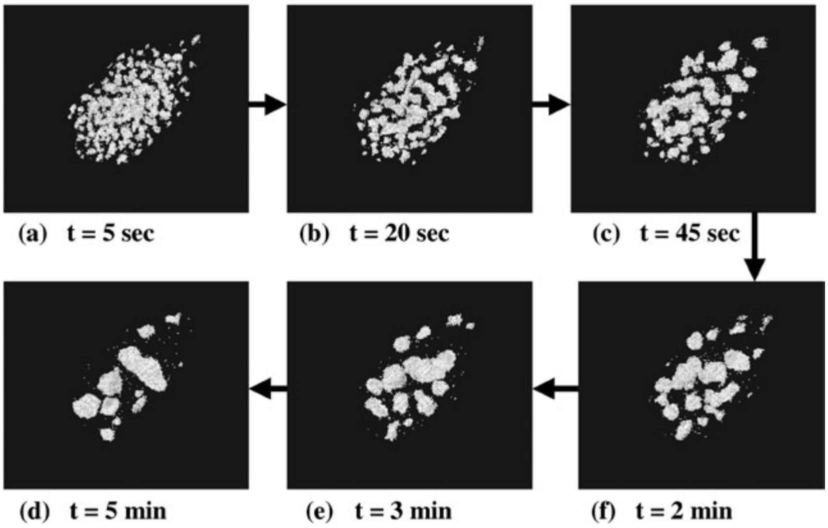

Figure 29. Zn precipitates in Al–Zn as a function of ageing time for $T = 250$ K: with increasing t the average size of the precipitates increases while their number decreases (only Zn atoms are shown).

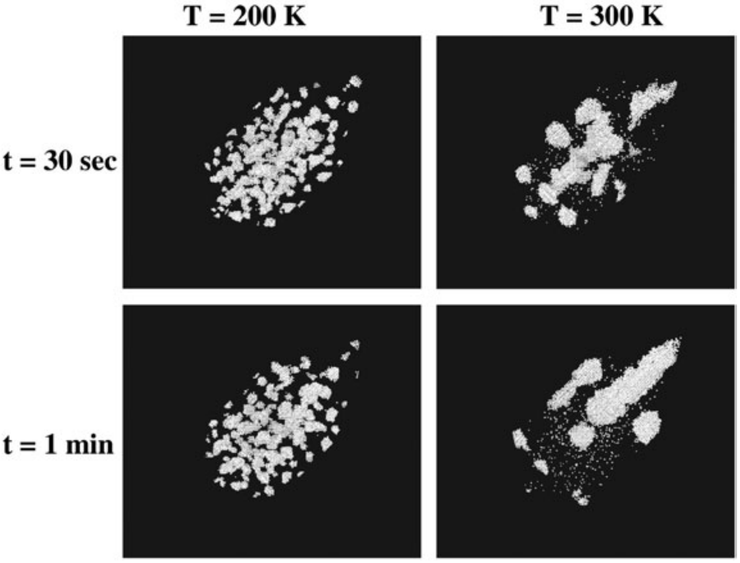

Figure 30. Zn precipitates in Al–Zn for two different ageing temperatures and times: for a constant ageing time, a higher ageing temperature leads to larger, but less, precipitates (only Zn atoms are shown).

precipitate configurations at $T = 250$ K. Frame (a) demonstrates that, even after an ageing time of only 5 s, many small coherent Zn precipitates are visible, while less than 10% of the Zn atoms remains in solution. Furthermore, we see that, with increasing ageing time, the number of precipitates decreases, while their average size increases. So, the number of precipitates decreases from $N_p = 58$ at $t = 5$ s down to $N_p = 10$ at $t = 5$ min.

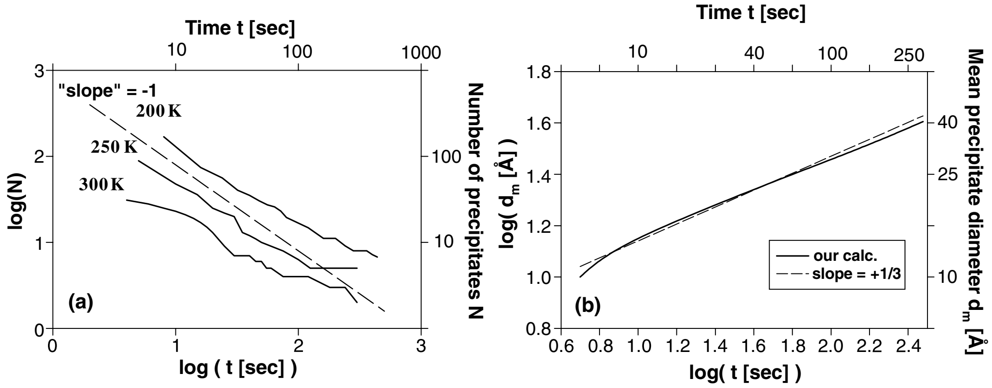

Figure 31. (a) Logarithmic plot of the number of precipitates versus ageing time in an $Al_{0.932}Zn_{0.068}$ alloy (11 942 Zn atoms) for three different temperatures. The slope of all three curves is very close to -1, i.e. the expected value for classical Ostwald ripening (broken line). (b) Logarithmic plot of mean precipitates diameter d_m as a function of ageing time. The resulting curve shows a slope of 0.31, very close to $1/3$ (broken curve) expected for Ostwald ripening.

In order to see the influence of the ageing temperature on the precipitate size distribution, figure 30 shows configurations for two different temperatures and ageing times: for a fixed ageing time the number of precipitates is larger for the lower ageing temperature, while the average size of precipitates is larger for the higher ageing temperature. In order to quantify these observations, figure 31(a) gives a logarithmic presentation of the number of precipitates, N versus the ageing time, t, for three different temperatures. In all cases, the $\log N$ versus $\log t$ plot shows a slope close to -1 (given by the broken line). *This slope is exactly the value expected for classical Ostwald ripening:* smaller precipitates disappear with increasing ageing time, while larger precipitates appear, leading to an increase of the mean diameter d_m via $d_m \propto t^{1/3}$. The fluctuations within each individual curve are caused by the limited system size. So, for example, for an ageing temperature of 250 K and an ageing time of 5 min, there are only 10 precipitates left, leading to quite poor statistics. Figure 31(b) displays the 'mean diameter', d_m, of all precipitates as a function of ageing time for $T = 250$ K. Here, d_m represents the diameter of a sphere with the same volume as the observed precipitate. As defined in section 4.3, this diameter is given by $d_m = 2r_m = 2(ca^2)^{1/3}$ with c and a the thickness and length of the ellipsoidal precipitates. Again, a logarithmic presentation is used, allowing for a direct determination of the observed slope: we find a slope of 0.31 very close to the $1/3$ slope of classical Ostwald ripening (given by the broken line in figure 31(b)). In summary, our studies suggest that the growth process of precipitates in Al–Zn represents an example of Ostwald ripening.

A more quantitative description of the decomposition permits the determination of the Warren–Cowley SRO parameters. Figure 32 shows the values of the first five SRO parameters α_{lmn} as a function of ageing time for $T = 250$ K. The curves correspond to the real-space images of figure 29. The SRO parameters are all positive, reflecting that precipitation is a phase-separating process. They show a significant increase during the first few seconds, in agreement with our observation that already after an ageing time of $t = 5$ s more than 90% of all Zn atoms belong to Zn precipitates (figure 29). After the creation of precipitates is terminated within these first few seconds, the rate of increase of α_{lmn} is reduced. Unlike the early growth stage, the time dependence of α_{lmn} is no longer controlled by the formation of new precipitates but by the disappearance of smaller precipitates in favour of larger precipitates (Ostwald ripening).

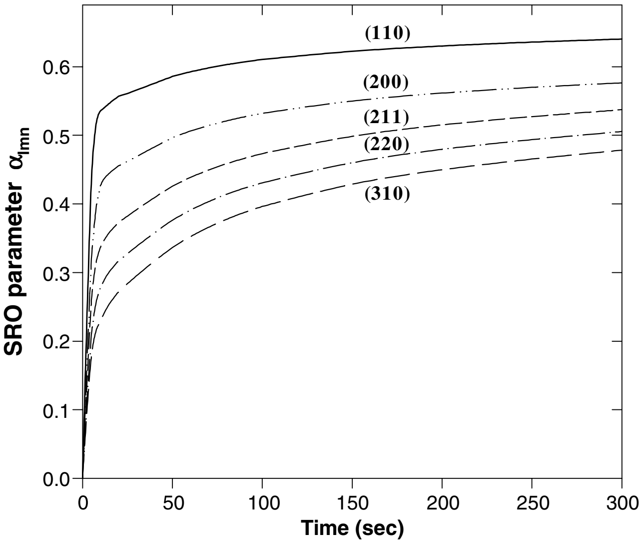

Figure 32. Time dependence of the first five Warren–Cowley SRO parameters ($T = 250$ K).

Table 6. Experimental SRO parameter of a $Al_{0.962}Zn_{0.038}$ alloy given by Haeffner and Cohen [180] at $T = 353$ K for $t = 3$ and 168 h and a comparison to kinetic MC values (this work). The right column gives the calculated parameters for the corresponding equilibrium configuration.

(lmn)	α^{exp}_{lmn} ($t = 3$ h)	α^{theo}_{lmn} ($t = 3$ h)	α^{exp}_{lmn} ($t = 168$ h)	α^{theo}_{lmn} ($t = 168$ h)	α^{theo}_{lmn} (equil.)
000	0.967	1.000	1.113	1.000	1.000
110	0.176	0.309	0.244	0.357	0.569
200	0.110	0.282	0.154	0.296	0.512
211	0.094	0.184	0.141	0.231	0.473
220	0.086	0.154	0.125	0.198	0.449
310	0.077	0.114	0.105	0.168	0.422
222	0.072	0.100	0.099	0.133	0.389
321	0.070	0.074	0.090	0.122	0.377
400	0.053	0.077	0.070	0.103	0.368
330	0.048	0.051	0.076	0.090	0.347
411	0.058	0.057	0.072	0.091	0.351
420	0.054	0.047	0.070	0.080	0.336

In 1989, Haeffner and Cohen studied the SRO order behaviour of $Al_{0.962}Zn_{0.038}$ as a function of ageing time via x-ray diffuse scattering [180]. The resulting experimental SRO parameters ($T = 353$ K) for two different ageing times are given in the second and fourth column of table 6: although the ageing time for the two measurements differ by almost two orders of magnitude, the resulting SRO parameters differ by only 20–50%, being in qualitative agreement with our observation. For a quantitative comparison, we applied our kinetic MC algorithms to an alloy with the same concentration (3.8% Zn) as used in the experiment and simulated the very same ageing times. The simulation of the ageing time of $t = 168$ h took about 5 weeks CPU on a Silicon Graphics Origin 2000. The comparison is given in table 6 together with the SRO parameter of the corresponding equilibrium configuration. Especially for the shorter ageing time ($t = 3$ h) the theoretical values of the first four shells are clearly larger than in experiment, while the agreement is excellent for higher shells [(222), (321), (400), etc]. In principle, this observation also holds for the second time ($t = 168$ h), although the agreement with experiment in the lower shells is improved. Possibly the increase in α_{lmn} is too strong at the early phase of the simulation. Other reasons could be that:

(i) the restriction of our model to nearest-neighbour jumps only is insufficient for the description of the real alloy system
(ii) the experimental data possess large errors.

Nevertheless, even for the long ageing time the configuration *cannot be described by the equilibrium configuration*. This becomes obvious by comparing the SRO parameter of the equilibrium configuration given in the last column of table 6 with the experimental SRO parameter. The theoretical parameters at equilibrium are nearly a factor of two higher than those for an ageing time of 168 h, emphasizing the fact that a description by thermodynamic arguments would not work.

5. Alloy surfaces: segregation, relaxation, ordering

5.1. Crystallographic structure and segregation profile

In the last section, we have seen that the ordering of bulk alloys cannot be simply divided into two classes of systems, namely phase-separating and ordering systems. At finite temperatures, the energetics of disordered alloys is clearly controlled by SRO which, in general, strongly depends on temperature and alloy composition. Now, it will be shown that the same difficulty with respect to classifying ordering tendencies holds also for alloy surfaces. The phenomenon on which we concentrate in the following is called surface segregation, denoting any deviation from an alloy's bulk-like composition and order in the vicinity of the surface. As already mentioned in section 2, the segregation of one component to the surface in *ordering* alloy systems should be forbidden from the fact that this requires the occupation of adjacent sites by identical atoms. There is, however, a second energy component which must be considered: the energetically preferred termination of the alloy surface. Obviously, the equilibrium structure will be controlled by the competition between these two characteristic energy terms. As an example, we will investigate the B2 phase of the systems Co–Al, Fe–Al and Ni–Al. Although the three TMs involved crystallize in different lattices (hcp-Co, bcc-Fe, fcc-Ni), their TM-Al phase diagrams exhibit B2 phases around $\mathrm{TM}_{0.5}\mathrm{Al}_{0.5}$. Since B2 (often referred to as 'CsCl' structure) is the prototype of so-called bcc-based alloys according to 'Strukturbericht', its existence is certainly most surprising in Ni–Al where none of the two constituents possesses the bcc structure. The critical temperature of the B2 phase amounts to about 1930 K for CoAl and NiAl, but only to about 1500 K for Fe–Al [149]. The lower stability of the latter is consistent with the bulk formation enthalpy, ΔH_f, which has a lower modulus for FeAl compared to CoAl and NiAl as already discussed in section 3.1 and displayed in table 1.

The ideal B2 structure of the three systems is schematically displayed in figure 33. In (100) orientation, the compound consists of alternating layers of the TM and Al. This allows for two possible surface terminations. We will focus on the Al-terminated phase, because Al clearly possesses the lower surface energy compared to the TM. For this comparison, the surface energies of the pure elements have to be calculated for the bcc lattice, i.e. bcc-Al ($\Delta E_{\mathrm{surf}} = 0.623$ eV/atom), bcc-Fe ($\Delta E_{\mathrm{surf}} = 1.150$ eV/atom), bcc-Ni ($\Delta E_{\mathrm{surf}} = 1.038$ eV/atom), and bcc-Co ($\Delta E_{\mathrm{surf}} = 1.175$ eV/atom). The low surface energy of bcc-Al should prohibit any segregation of TM atoms to the surface layer. We will see that this simple conclusion fails at least for CoAl(100).

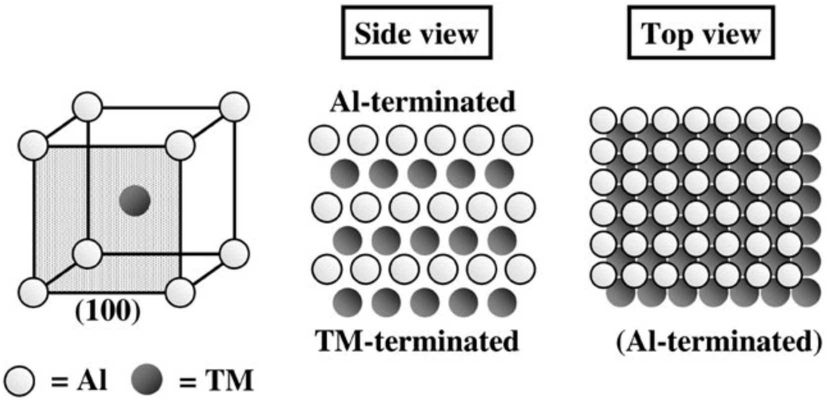

Figure 33. The B2 structure can be interpreted as alternating Al and TM layers along the crystallographic [100] direction. This either leads to an Al- or a TM terminated surface. In this work, we concentrate on the Al-terminated alloy surface (as displayed for the 'top view').

For a detailed geometric characterization of the TM-Al(100) surface structures, GGA-based spin-polarized DFT calculations [181] were performed and the results were compared to the best-fit structure retrieved from low-energy electron diffraction (LEED). The LEED versus DFT comparison is shown in figure 34 using schematic side views. In the case of NiAl(100), the LEED structure determination by Davis and Noonan [182] was carried out for the high-temperature phase of NiAl and finds an Al-terminated surface with no sign of segregation. The layer distances are given as deviation from the bulk layer spacing d_b. For the first interlayer distance d^{12} a strong inward relaxation is observed, whilst the spacing between the second and third layer is slightly increased. Considering the fact that a deviation of 1% corresponds to about 0.014 Å only, LEED and DFT results agree very well. Unfortunately, the situation is not as easy as it seems: different studies arrive at contradictory and mutually exclusive results for the high-temperature annealed NiAl(100) surface including a complete Al termination [182], a termination by a mixed Al-rich layer [183, 184] and even a bulk-like Ni termination with [185] and without [186] vacancies. We will come back to this discrepancy at the end of this section.

The LEED structure determinations for FeAl(100) and CoAl(100) were performed by the Erlangen LEED group [67, 187] using the 'TensErLEED' code for the intensity analysis [63]. The concentrations of the first five layers were determined by applying the ATA [136] introduced in section 3.4, which allows us to simulate the scattering properties of a random alloy.

The FeAl sample used had an average Al concentration of 47% only, so that the question arises whether the 'additional' 3% of Fe atoms occupy sites in the volume or segregate to the surface. As we see from figure 34, the best-fit structure shows an Al-terminated (100) surface which is again consistent with the surface energies of the pure elements. The determined multi-layer relaxation is very similar to the surface of ideal NiAl: the first spacing is contracted and the second one is expanded.

From the results, one may guess that the situation will probably be the same for CoAl(100). However, the LEED analysis tells a different story (figure 34): we find a large amount of Co atoms (30 ± 7%) which reside on the nominal Al-terminated topmost layer. This large enrichment of so-called *antisites* or defect atoms is restricted to the first layer, the second and third layer show much less disorder and no deviation from bulk order and geometry is

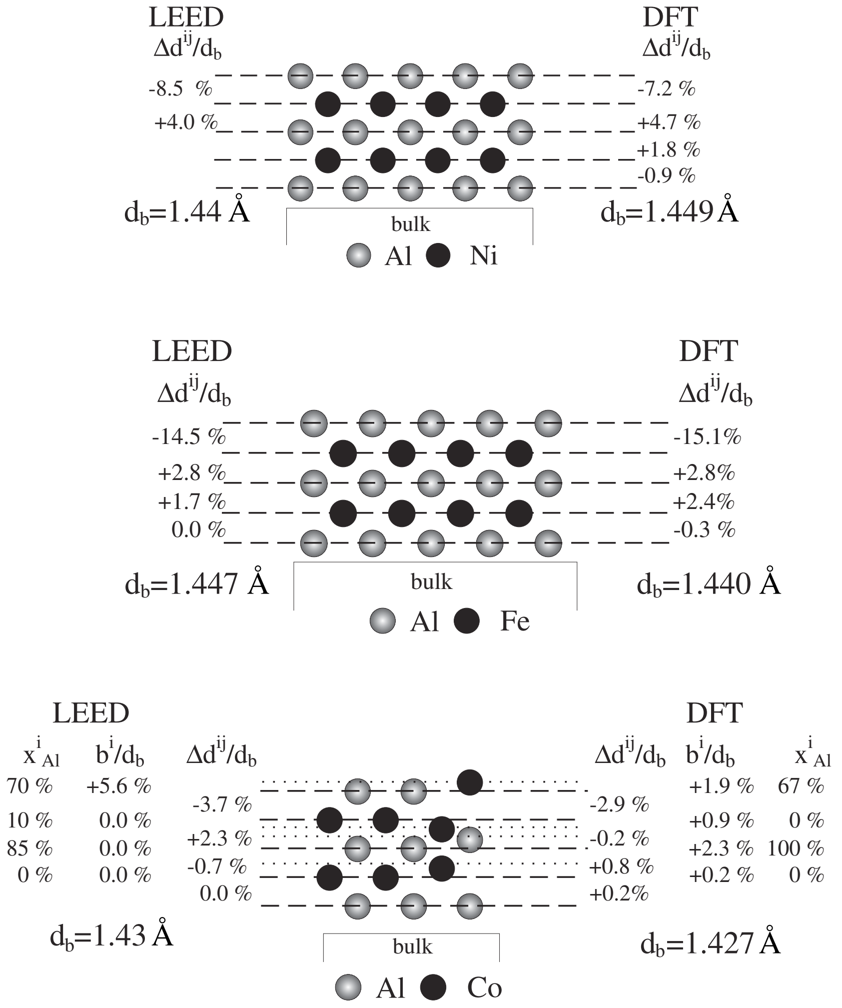

Figure 34. Comparison of structural parameters for CoAl, FeAl and NiAl(100) determined via DFT and LEED structure analyses (schematic side view). While x^i_{Al} denotes the Al concentration in layer i, Δd^{ij} and b^i give the individual layer spacings and buckling amplitudes as deviations from the ideal interlayer distance d_b.

detectable below the third layer. There is some geometric buckling caused by the existence of two different species in the first layer, whereby the Co antisites show some outward relaxations relative to the Al atoms. No buckling is retrieved for deeper layers.

One possible explanation for the found Co antisite defects would be that the experimental data do not correspond to the equilibrium state of a certain antisite concentration in the near-surface region of CoAl(100). This can, however, be excluded by annealing the sample to rather high temperatures in order to disperse the Co antisite defects to the bulk and to follow their segregation behaviour (details are given in [188]). So, the question arises, how the existence of antisites on the CoAl(100) can be explained *ex post facto*. As a first step in understanding, the surface energies, as introduced in section 3.4, for different surface terminations were calculated. Since the first-principles calculations are restricted to ordered arrangements (otherwise, a CE

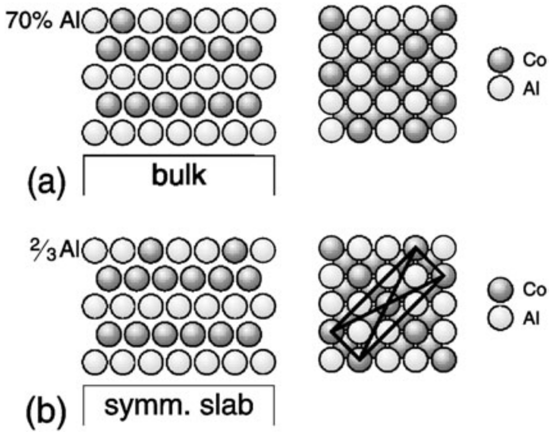

Figure 35. Side and top views of (a) the LEED best fit structure and composition of CoAl(100) assuming a random distribution of atoms within the layer, and (b) the ordered model slab used to simulate top layer antisites in first-principles calculations.

has to be constructed which will be discussed in section 5.2), this demands we select a suitable model to simulate antisites in the topmost layer. We choose the c($\sqrt{2} \times 3\sqrt{2}$)CoAl$_2$ structure for the top layer which is shown in figure 35(b) on top of a B2 ordered substrate. For the ordered model slab the in-plane unit cell is marked by black lines. This structure—often referred to as '(3 × 3)diag' structure—was favoured for two reasons:

(i) The CoAl$_2$ top layer contains 33% Co atoms, very close to the 30% retrieved from LEED.
(ii) Although the experimental LEED pattern of CoAl(100) shows a (1 × 1) symmetry with sharp integer order spots, there were some diffuse intensities indicative of some lateral SRO, consistent with the assumed c($\sqrt{2} \times 3\sqrt{2}$) unit cell.

The model was used for a DFT calculation of the CoAl(100) surface. Considering the fact that the LEED intensity analysis is based on a random alloy, while the DFT calculation used an ordered (3 × 3)diag reconstruction for the topmost layer, there is a reasonable agreement between the structural parameters resulting from DFT and LEED (figure 34). It should be mentioned that the (3 × 3)diag reconstruction is also coupled to some lateral shifts in the topmost layer which are, however, not important for the following discussion.

Table 7 gives the calculated surface energies in electronvolts per atom for a number of different, geometrically fully relaxed (100) alloy surfaces with different terminations. Besides the Al- and Co-terminated surface, and the (3 × 3)diag structure for the topmost layer, we additionally provide data for a chemical c(2 × 2) superstructure (with a '50:50' concentration in the top layer) and a complete Co layer (i.e. all Al atoms are replaced by Co antisites, leading to two complete Co layers at the alloy surface) called 'TM 1L'. We immediately see (table 7) that for *all three systems* the Al-terminated alloy surface has the *lowest surface energy* followed by the (3 × 3)diag-terminated surface. So, the surface energies are *not* responsible for the existence of Co antisites in the topmost layer of CoAl(100).

In equilibrium, there are two possible mechanisms for the top layer enrichment with Co antisite defects: their creation right there or their segregation from a slightly Co-enriched region below. As shown earlier [189], the mere creation of a Co antisite costs as much as 1.29 eV so that the former mechanism can be ruled out. In order to check for the second possibility, i.e. the segregation of existing Co antisites, we use the concept of segregation

Table 7. Surface energies of the TMAl(100) surfaces of B2 compounds with different alloy surface terminations. All energies correspond to geometrically fully relaxed structures.

	ΔE_{surf} (eV/atom)		
Surface termination	FeAl	CoAl	NiAl
Al	0.53	0.94	1.02
TM	1.53	1.91	1.36
(3 × 3) diag	0.81	1.35	1.16
c(2 × 2)	0.93	1.61	1.26
TM 1L	1.55	2.33	2.28

energies, as introduced in section 3.4, equation (33). From there, we recall that the segregation energy ΔE_{seg} is the energy difference with respect to the exchange of a surface atom (here, Al) with a bulk antisite defect (here, TM). This ansatz considers both the change in surface energy by replacing the Al atom by an antisite and the bond energy change between the nearest and possibly more distant neighbours. Methodically, relatively large model slabs are necessary for the calculations: an isolated defect (TM) in a supercell consisting of six 3×3 (100) layers was used as the model (analogous to Bester *et al* [189]) whereby full structural relaxations were allowed for the 54 atoms. The resulting segregation energies for three different surface terminations with antisite concentrations of 50% (c(2 × 2)), 75% ((3 × 3)diag) and 100% (1M TL) Co are shown in table 8. Indeed, the resulting values allow for an interpretation of the experimentally found surface structures, figure 34: for CoAl(100) and NiAl(100) the low segregation energies for the (3 × 3)diag surface structure of −0.85 and −0.61 eV prove that antisite segregation is accompanied by an energy gain so much larger than the thermal energy that even a TM excess well below 1% should drastically influence the surface's stoichiometry when equilibrium is achieved. In contrast, we find positive segregation energies for FeAl(100) whereby the segregation of antisites to the surface, assuming a $c(2 \times 2)$ structure, is energetically degenerated with the case of no segregation. This, however, leads to the interpretation that the surface termination of an *ordered* alloy is *not* necessarily defined by the ideally ordered compound, but can be dominated by *minor* subsurface or bulk deviations from its ideal composition. This result immediately allows us to resolve the experimental discrepancies of NiAl(100) surfaces as described above. The contradictory observations are probably only the result of slightly different levels of off-stoichiometry in the sample used, which can clearly be below the detection limit of the techniques applied. Even if the sample has nominally a concentration of 50% Al, there certainly can be tiny deviations from this value in real alloy crystals. Although this deviation may be extremely small, the type of existing antisites (Al or Co) will dominate the surface properties of the alloy. Our findings receive additional support from recent theoretical works by Ruban [190] for fcc Ni_3Al and Pt_3Fe and Pourovskii *et al* [191] for Ni–Pt, both based on coherent potential calculations in the approximation of geometrically unrelaxed lattices.

The control of the surface composition by tiny bulk off-stoichiometries in CoAl(100) compounds demand we extend today's understanding about the stability of alloy surfaces to the possibility of antisite defect segregation. This concept permits us to place the three related systems NiAl(100), FeAl(100) and CoAl(100) in one consistent picture. The significance of the described scenario should reach beyond the examples described and represents an important step towards a general understanding of the surface and interface properties of strongly ordering materials.

Table 8. Segregation energies, ΔE_{seg} for TMAl(100) of B2 compounds for different surface terminations.

	ΔE_{seg} (eV/atom)		
Surface termination	FeAl	CoAl	NiAl
(3 × 3)diag	+0.05	−0.85	−0.61
c(2 × 2)	+0.00	−0.76	−0.54
TM 1L	+0.23	−0.71	+0.05

Table 9. Interlayer distance d^{12} between the first and second layer of the CoAl(100) surface assuming different structural models for the topmost layer. The bulk spacing is $d_b = 1.43$ Å. The left column gives the value determined by LEED. Furthermore, the buckling amplitude b_1 between structurally independent atoms in the topmost layers is given.

	LEED	DFT-(1 × 1)	DFT-c(2 × 2)	DFT-(3 × 3)diag
d^{12} (Å)	1.38	1.306	1.345	1.385
b_1 (Å)	0.08	—	−0.096	0.027

5.2. Short-range order at surfaces

Although the use of the (3 × 3)diag structure as a model for the CoAl(100) surface reproduces the experimentally determined antisites' stoichiometry, the precise SRO is still lacking as there are no experimental data available. A way out is offered by the influence of the top layer chemical structure on the spacing and buckling of the top layer which are available with high precision from LEED. Table 9 compares the results calculated for the c(2 × 2) and (3 × 3)diag long-range ordering as well as for the absence of segregation [(1 × 1)] with experiment. Only the (3 × 3)diag structure provides the correct sign of buckling and, at the same time, the calculated top layer contraction comes closest to experiment.

However, this favourable comparison might be by chance or other models might fit the experiment even better. Therefore, we apply the combination of DFT and CE, as used for alloy bulk problems in section 4. The consideration of the surface's properties demand some additional effort (see section 3.4), especially with respect to the number of input DFT structures. However, in the case of Co–Al, the problem can be simplified: from the LEED best-fit structure of the CoAl(100) surface it is known that antisites exclusively segregate to the *topmost* alloy layer. There is no significant antisite segregation in the next Al layer (third layer) visible; only 10% Co are detected in the third layer of CoAl(100) via LEED. This percentage is so small that it may be caused by some strong parameter correlations in the LEED structure determination [192]. Since the second alloy layer is always a complete Co layer, the local environment with respect to deeper layers is the same for all atoms in the topmost layer. Indeed, a deviation from a complete Co layer in the second layer would demand the formation of Al antisites. The energy cost to replace a Co atom by an Al antisite amounts to 3.11 eV/atom and therefore such an exchange will not happen at all in practice. For these reasons, the lateral SRO in the topmost layer of CoAl(100) should be describable by a two-dimensional CE as sketched in figure 36. The subsurface layers are treated as layers of a perfectly ordered B2 compound, while the ordering properties of the first layer are studied by combining CE with MC simulations. Such an ansatz was successfully used to characterize a single atomic PdAu [193] and CoAg [194] layer evaporated on Ru(0001). A similar approach was applied by Scheffler's group for investigations on adsorption [195] and oxidation [196] on surfaces.

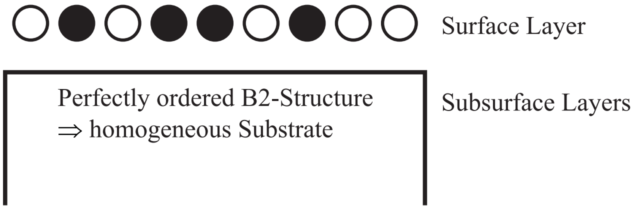

Figure 36. Schematic side view of the model used for the CoAl(100) CE.

Table 10. Detected ground states of the topmost layer of CoAl(100) as a function of Co antisite concentration. The ground states result from the constructed ground-state diagram, figure 38.

Model	Top view	Co conc. %	ΔE_{surf} (meV/atom)	$\Delta E_{\mathrm{surf,mix}}$ (meV/atom)
Al-terminated	○○ ○○	0	935	0.0
Structure (a)	○○●○ ○○○○ ●○○○ ○○○○	12.5	1083	−27
(4 × 4) diag	○○○● ○○●○ ○●○○ ●○○○	25.0	1237	−48
Structure (c)	○○●● ○○●○ ●●○○ ●○○○	37.5	1405	−54
Structure (d)	○○●● ○○●● ●●○○ ●●○○	50.0	1576	−58
Co 1L	●● ●●	100	2333	0.0

A set of 18 input structures only for the topmost layer was necessary to stabilize the 14 pair and multi-body figures used for the CE construction as given in figure 37. The calculated surface energies of the selected input configurations correspond to geometrically fully relaxed structures. Thereby, a positive value of the interaction stands for ordering, with a negative value for clustering. A further reduction of the given set of effective interactions will destabilize the CE fit. Again, the Conolly–Williams approach [102] (section 3) was applied for the determination of the interactions. It should be mentioned that there is no nearest-neighbour bond within the (100) layer, but only *between* neighbouring layers. Therefore, the first pair interaction constructed corresponds to the second neighbour distance. We see from figure 37 that the first and third in-plane neighbour interactions are positive, favouring ordering, while the second neighbour interaction is negative, favouring clustering, consistent with the assumed ordering type, (3 × 3)diag, in section 5.1.

Analogous to section 4.1, a ground-state diagram is constructed whereby, however, we now use the Co concentration in the topmost alloy layer as a parameter with a perfectly ordered B2 structure below. *All* possible atomic configurations with up to 20 basis atoms in the in-plane unit cell have been considered for the ground-state search. The resulting ground-state line which was constructed from more than a million configurations is shown in figure 38. The y axis of the diagram gives the *surface mixing enthalpy*, $\Delta E_{\mathrm{surf,mix}}$, with the surface energies of the purely Al ($x = 0$) and purely Co ($x = 1$) terminated surface of the B2 structure as reference energies (so, $\Delta E_{\mathrm{surf,mix}} = 0.0$ meV for the Al- and Co-terminated surfaces). For $0 \leqslant x \leqslant 1$

$$\Delta E_{\mathrm{surf,mix}}(\sigma) = \Delta E_{\mathrm{surf}}(\sigma) - (1 - x)\Delta E_{\mathrm{surf}}(\text{Al-term}) - x\Delta E_{\mathrm{surf}}(\text{TM 1L}) \tag{45}$$

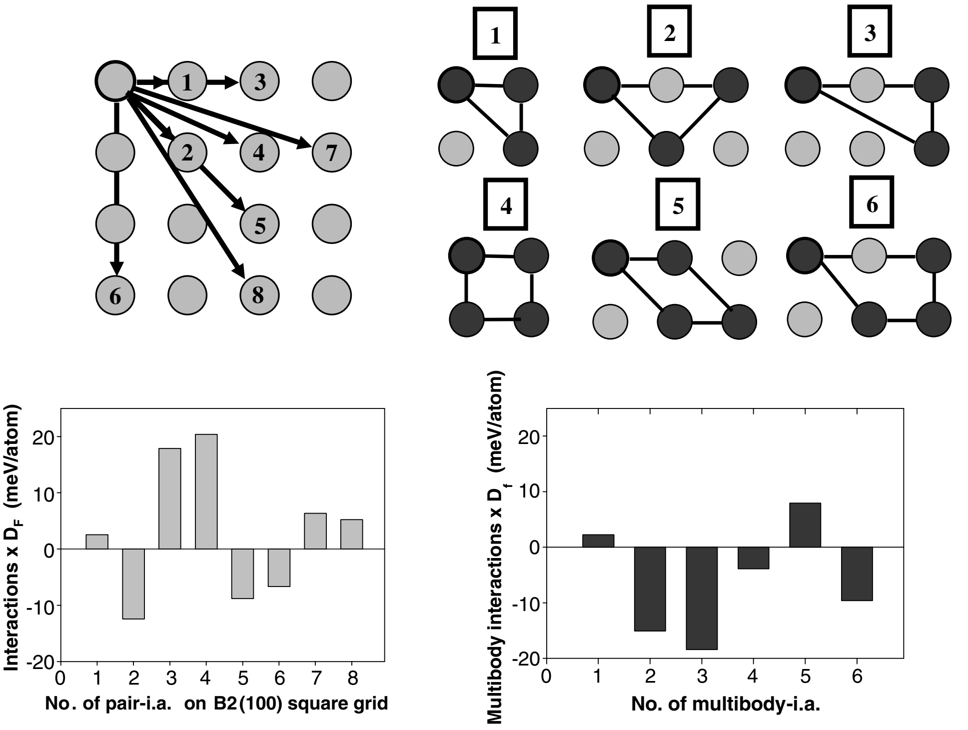

Figure 37. Used pair and multi-body figures for the two-dimensional CE of CoAl(100) and corresponding interaction energies. The values are already multiplied by their individual degeneration factors D_F.

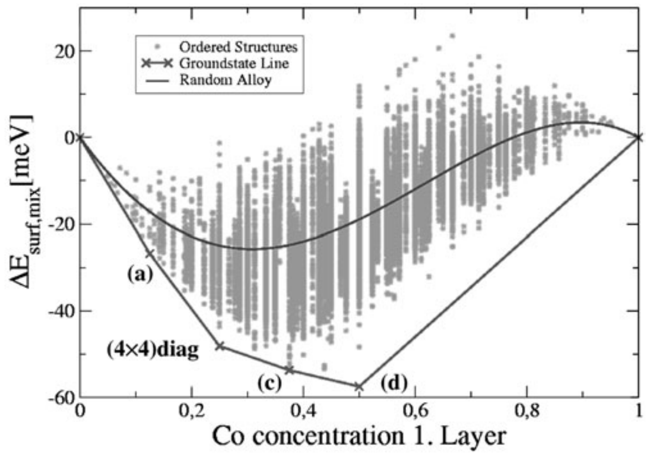

Figure 38. Calculated ground-state diagram for the CoAl(100) surface.

results, whereby ‘TM 1L’ again describes an alloy surface with the first Al layer completely replaced by Co antisites. We find a number of LRO structures within the topmost alloy layer as listed in table 10. Most important for the problem discussed in this work, the predicted ground state for $x_{\mathrm{Co}} = 1/3$, is formed by two domains: the (4 × 4)diag structure being the ground state for $x_{\mathrm{Co}} = 1/4$ and 'structure (c)' in table 10 being the ground state for $x_{\mathrm{Co}} = 3/8$. So we see that, indeed, the assumed (3×3)diag structure is not a ground state, although the ordering type found (diagonal chains) is very similar to that of the (3×3)diag. The ground-state diagram, figure 38, also displays the surface mixing enthalpy for all other considered surface terminations as well as for the ideal random alloy. The latter lies energetically far above the ground-state line manifesting the lateral ordering tendency of the topmost layer.

Although the ground-state analysis allows us to determine the kind of ordering for any arbitrary antisite concentration in the topmost layer, one has to remember that it applies to $T = 0$ K. In order to get access to *finite* temperatures, the constructed interactions (figure 37) were used in MC simulations in order to predict the SRO of the topmost layer at finite temperatures. We chose temperatures $T = 200$ and 500 K for the simulations. The number of MC steps was increased until the resulting energy per atom became constant except for the usual statistical fluctuations.

For a 60×60 cell the resulting real-space configurations at $T = 200$ K are displayed for $x_{\mathrm{Co}} = 0.30$ and 0.50 by schematic top views in figure 39. The lower panels show enlarged sections marked by white frames in the complete MC cell (upper panels). For $x_{\mathrm{Co}} = 0.30$, we see the formation of Co chains along the [011] direction (along the diagonal defined by the lower left and upper right corners). These Co chains are mostly separated by at least two or three diagonal Al rows; there is *no clustering of Co(011) chains*. These ordering tendencies are, indeed, characteristic for the ground-state structures found at this concentration (table 10). Even for the higher antisite concentration, $x_{\mathrm{Co}} = 0.50$, the system tries to prohibit the occupation of parallel diagonal [011] rows by Co atoms. Instead, chains of Co atoms along the [001] and [010] directions are found. This behaviour is consistent with the ground-state structure determined: reinspecting table 10, we see that for 50% Co antisites the resulting ground state is given by quadratic blocks ordered along [011] consisting of four Co antisites.

Increasing the temperature destroys a large percentage of the characteristic Co chains along [011] which is shown for $x_{\mathrm{Co}} = 0.30$ in figure 40: for $T = 500$ K the configuration already clearly shows less diagonal chains of Co atoms than the configurations displayed in figure 39. However, the ordering still shows deviations from an ideal random alloy.

In summary, our calculations demonstrate that, although the use of the (3×3)diag structure as a model for the topmost layer of a CoAl(100) surface represents a very reasonable guess, it is not the ground state with respect to the ordering of the topmost layer. Our studies would even allow for a quantitative comparison of SRO with experiment via the Warren–Cowley SRO parameter. However, this would demand experimental investigations via STM on such surfaces which do not—to the best of my knowledge—exist so far.

5.3. Beyond the limits of cluster expansion: incommensurate phases

It was already mentioned that the considerable interest in lightweight material alloys such as Al–Cu, Al–Mg or Al–Zn comes from the possibility of hardening these alloys by controlled heating and cooling processes. It is believed that the hardening effect is due to coherent precipitates which act as obstacles for dislocation motions through the crystal. As we have seen in section 4.3, the combination of MSCE and MC with DFT calculations allows us for the first time to study extensively the shape-controlling factors of these microstructures on quantum-mechanical grounds. However, up to this point we ignored the fact that, especially for technical applications, the properties of the alloy surface become relevant. Surface properties of Al-rich Al–Zn alloys are of particular interest with respect to the influence of precipitate hardening on the surface. For this reason, we return to the phase-separating, fcc-based alloy system Al–Zn which will bring our investigations beyond the applicability of CE. Moreover,

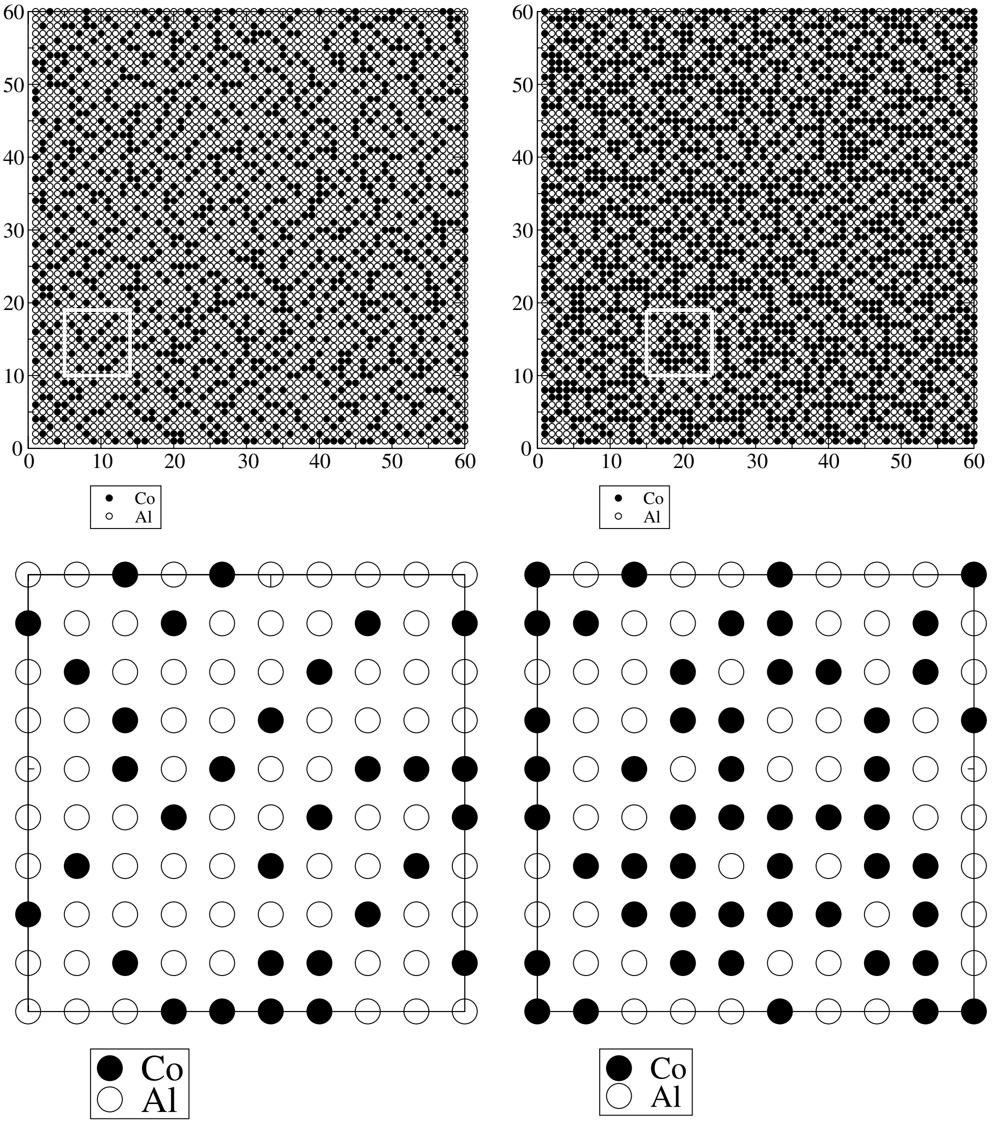

Figure 39. Resulting top layer configurations of CoAl(100) at $T = 200$ K for $x_{\mathrm{Co}} = 0.30$ and $x_{\mathrm{Co}} = 0.50$. Especially for $x_{\mathrm{Co}} = 0.30$, the tendency of Co antisites to form chains along [011] is clearly visible. For $x_{\mathrm{Co}} = 0.50$ chains along [010] and [001] were formed to prevent clustering of [011] chains.

surface segregation at low-index surfaces still represents probably the best-suited model to study segregation at grain boundaries which are normally too complex for a treatment via first-principles calculations.

In the following, we focus on the Al–Zn(111) surface for two different reasons: on the one hand, the difference in the surface energies of Al(111) and fcc-Zn(111) is largest among the low index surfaces (table 3), so that Zn segregation may be expected. On the other hand, the mechanical instability against rhombohedral distortions found in this direction (figure 27) allows for large relaxations of the Zn layers. As a consequence, many segregation profiles

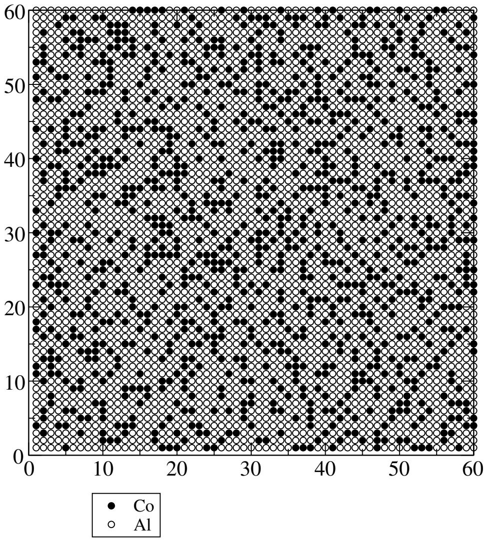

Figure 40. Resulting top layer configurations of CoAl(100) with 30% Co antisites for $T = 500$ K.

possess nearly identical surface formation energies, because the creation of [111] interfaces does not cost more than 1–2 meV/atom. Indeed, this energy amount is much smaller than the mentioned difference in the surface energies of fcc-Zn(111) and Al(111). Consequently, calculations via fcc-based CE lead, for $T \to 0$, to a lowest energy structure with two [111] interfaces and two Zn-terminated surfaces. Again, the starting point for this calculation was an ideal random alloy containing 8% Zn, from which the final configuration has emerged via MC simulated annealing.

Indeed, experimental observations [197] of Al–Zn(111) surfaces report Zn-covered surfaces even at room temperature. We may interpret this enrichment of Zn atoms at the surface as a *Zn film on the surface of an Al-rich Al–Zn alloy*. From this perspective, the system Al–Zn(111) could be interpreted as a 'self-epitaxial' system with the formation of a Zn film driven by segregation. Since [111] is the elastically softest direction in fcc-Zn, but the hardest direction in Al, the equilibrium lattice parameter in Al-rich Al–Zn alloys comes very close to the lattice constant of pure Al: as we know from LDA calculations applying the concept of constituent strain, for a (111) Al–Zn SL with 8% Zn the expected lattice parameter is practically identical to that of elemental Al. Consequently, the properties of an Al–Zn(111) interface separating even a large number of near-surface Zn layers from the Al-rich bulk should be well described by Zn layers grown on Al(111).

However, the existence of a nanometre-thick Zn film demands the consideration of the following two problems:

(i) Even if the Zn film maintains coherence at the interface with the Al bulk, it would be unlikely that near-surface Zn layers still crystallize in the fcc lattice, because the misfit in the in-plane lattice constants of hcp-Zn and Al amounts to as much as 7%. Instead, the stacking sequence may switch from fcc to hcp stacking which can be realized simply by stacking faults (figure 41). While both fcc(111) and hcp(0001) crystal surfaces are built from the same close-packed layer, their stacking is different: fcc(111) possesses the 'ABC' stacking sequence, but hcp(0001) is 'AB' stacked. We applied DFT to study the

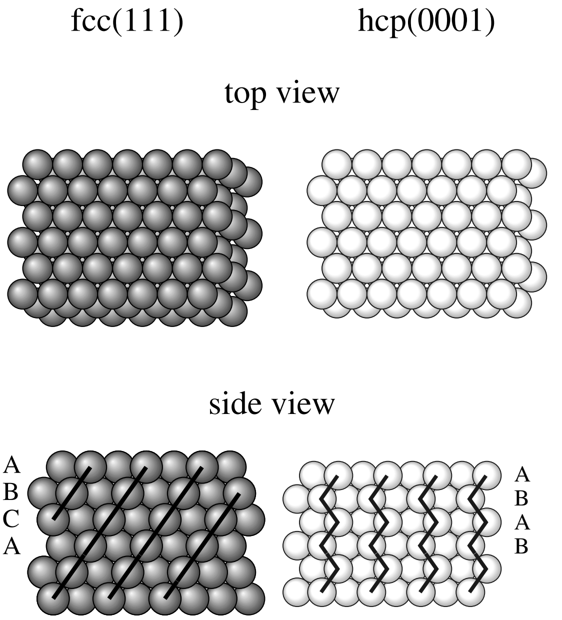

Figure 41. While fcc(111) and hcp(0001) are both formed by close-packed layers (top view), their stacking is different (side view): fcc(111) shows 'ABC' stacking, whilst for hcp(0001) 'AB' stacking applies.

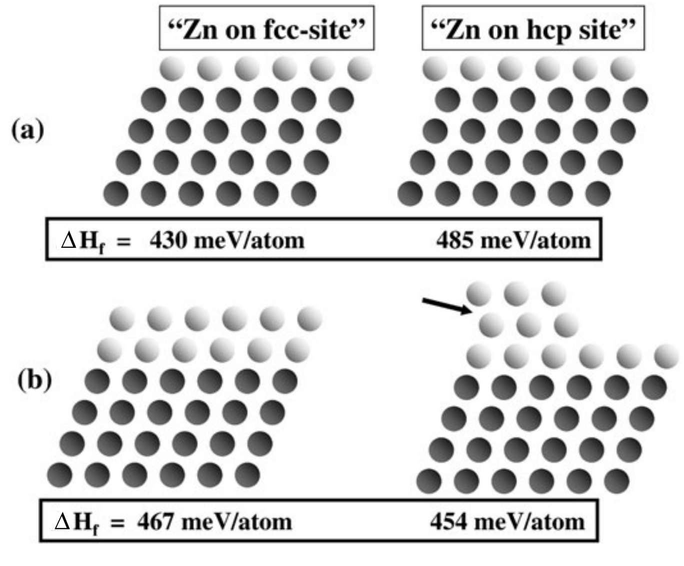

Figure 42. Schematic side views of different stacking sequences of epitaxially grown Zn films on Al(111): results of first-principles calculations, assuming that the Zn film grows commensurately on Al. (a) For 1 ML thick films, fcc stacking is energetically preferred. (b) For larger coverages, stacking faults and three-dimensional island growth are found.

stacking sequence of film layers for the hypothetical epitaxial system Zn/Al(111) which is—following the discussion above—probably the best-suited model to get access to this alloy interface. We found that, for film thicknesses up to two monolayers (ML),[3] only the continuation of the Al fcc stacking is energetically favoured. As an example figure 42(a) compares the surface formation energies for a coherent fcc- and hcp-stacked Zn layer on Al(111), demonstrating the preference for the fcc stacking. We also checked for the growth mode. Thus, we compared the energies of different film morphologies (flat layers, islands with different height and stacking, etc) for a given Zn coverage. Our calculations clearly predict Stranski–Krastanov growth for epitaxially grown Zn films: first a complete Zn layer is formed on the Al(111) surface, before three-dimensional island growth sets in. As an example, figure 42(b) compares the surface formation energies of 2 ML Zn films consisting of two flat fcc layers (left) and a '50–50' mixture of a trilayer and a monolayer (right). The stacking fault (with respect to fcc) in the trilayer between the top and second film layer corresponds to the arrangement of the lowest energy for islands that are three layers high. We see that the configuration with two different island heights lies energetically below layer-by-layer growth. All surface formation energies given apply to geometrically fully relaxed structures.

(ii) If the growing film switches its stacking from fcc to hcp, it may also be possible that the in-plane lattice parameter changes from the Al to the Zn (hcp-Zn) lattice constant. Then, the system can no longer be described as a *coherent* system. Instead, a *grain boundary* will emerge. In epitaxial growth, this is called *incommensurate growth*. In order to check for that, we repeated our DFT calculations for the initial growth mode for small, i.e. laterally limited, Zn islands, whereby both the island size and its position on the substrate were varied. Technically, this demands DFT calculations of model systems with more than 200 atoms, which is close to the limits of current computers, especially when geometric relaxations have to be considered. We used a 6×6 Al surface unit cell so that Al layers consist of 36 atoms, whilst the island sizes varied between 7 and 19 Zn atoms. Since the main conclusions are largely independent of the island size, we can restrict the discussion to the smallest one, as shown in figure 43(a): as soon as we allow for lateral relaxations, the Zn island *no longer maintains coherence* with the Al(111) substrate, but relaxes laterally close to its native lattice parameter[4], while the layer distance between the Zn island and Al substrate slightly changes. The resulting energy gain amounts to 52 meV/atom. Thus, the centre atom of the island favours the fcc-hollow site over the hcp-hollow site of the Al substrate by 22 meV/atom. We also determined the orientation of the incommensurate island by rotating it around its centre. The result is shown in figure 43(b) as a function of the rotation angle Θ ($\Theta = 0$ corresponds to the orientation of two fcc-hollow sites). The minimum energy develops for $\Theta = 0$, i.e. the configuration where the island has its in-plane lattice vectors parallel to those of the Al substrate. With the calculations repeated for bilayer high islands, the results are the same: there is incommensurate growth with a lattice parameter very close to that of hcp-Zn. Interestingly, the distance between the two Zn layers is already according to the anomalous d/a_p ratio of hcp-Zn ($d/a_p = 1.15$).

At this point, we will compare the calculations with experimental results retrieved from our LEED studies. The experiments were carried out in a standard UHV chamber equipped with a four-grid LEED optics which also served as a retarding-field spectrometer for Auger electron spectroscopy (AES). The film coverage was determined via thermal desorption spectroscopy (TDS). Zn was evaporated from a Mo crucible (experimental details are given elsewhere [198]).

---

[3] We define one monolayer as that amount of atoms necessary to completely cover the Al substrate surface by Zn. In the case of coherent growth the number of film atoms per layer is identical to the number of substrate atoms per layer.

[4] The discrepancy between the Zn bulk lattice constant and the lattice parameter found (figure 43(a)) of the island is caused by the rather limited island size and disappears with increasing number of Zn atoms.

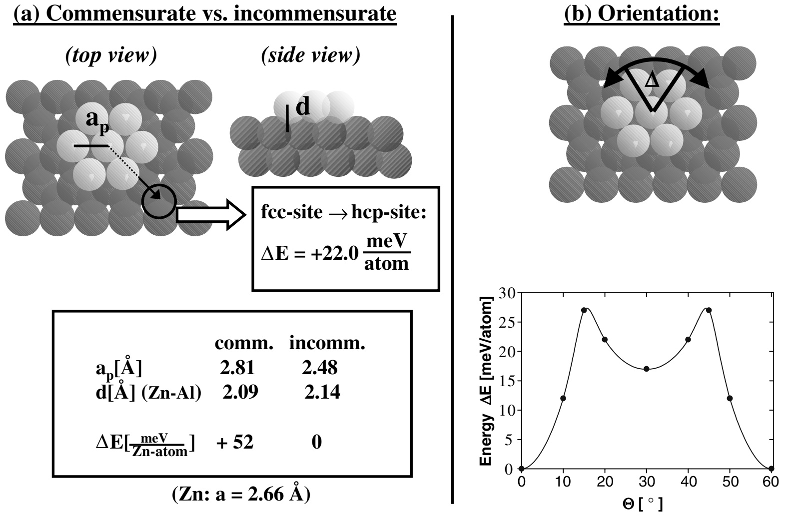

Figure 43. (a) Top and side view of a 1 ML high and 7 atoms large Zn island on an fcc(111) surface: As soon as we allow for lateral relaxation the Zn island becomes incommensurate with respect to Al(111). (b) Energy per Zn atom as a function of island orientation. The lowest energy position corresponds to a parallel adjustment of Zn and Al surface unit cell vectors.

Figure 44 shows the LEED pattern ($T = 100$ K) of a Zn film ($\Theta \approx 2$ ML) evaporated on Al(111) at $T = 400$ K. There are six satellite spots around every integer-order spot. The hexagonal arrangement of the integer-order spots reflects the symmetry of the Al(111) surface. With increasing energy of the incident electron beam a second, third, etc, diffraction order of these satellite spots appears in the LEED pattern which can be interpreted by the following picture: the satellite spots are caused by a close-packed film layer with a *smaller* in-plane lattice parameter than Al(111). Consequently, its unit-cell vectors in k space must be *larger* than those of Al(111). It turns out that, with increasing Zn coverage, all satellite spots disappear except for that one called $(1, 0)_{\mathrm{Zn}}$ in figure 44. This spot lies to the right of the Al integer-order spot and therefore the corresponding real-space unit vector is smaller than that of Al. The same observation also holds for the (0,1) spot. All other satellite spots arise by multiple diffraction processes between incommensurate Zn and Al layers and disappear together with the Al integer-order spots when the film thickness exceeds the penetration depth of the LEED electrons. A detailed analysis of a number of LEED patterns recorded for different electron energies and Zn coverages always finds that the $(1, 0)_{\mathrm{Zn}}$ satellite spot corresponds to about a 7% smaller in-plane lattice parameter being exactly the misfit between the in-plane lattice parameters of Al(111) and Zn(0001). So, our observation is consistent with the predicted growth of an incommensurate Zn film on Al(111) from the very beginning. However, the LEED pattern allows for more information: we see that the superstructure spots are as sharp as the integer-order spots, i.e. there is long-range ordering, at least within the range of the transfer width of the LEED optics (~200 Å). Therefore, the first Zn layer will most likely already be completed before the next film layer starts to grow. With increasing Zn coverage the Al spots disappear as well as the multiple diffraction spots, i.e. one of the six satellite spots remains so that finally a (1×1) LEED pattern can be observed due to an unreconstructed, incommensurate Zn film. The LEED pattern has threefold symmetry. With further increasing Zn coverage the symmetry of the pattern changes continuously from three- to sixfold as shown in figure 45 by comparing experimental LEED $I(E)$ spectra for the (10) and (01) beams. At this

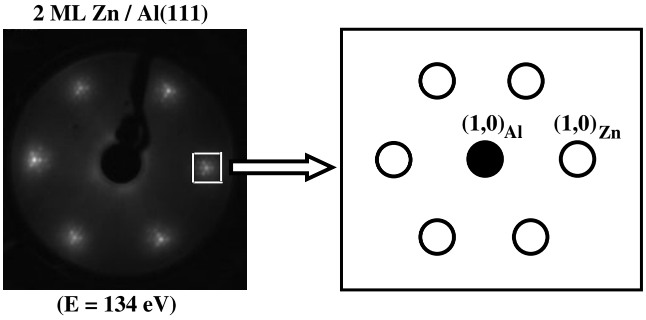

Figure 44. LEED pattern of 2 ML Zn/Al(111). The superstructure spots around each Al spot are characteristic for incommensurate growth (see the text).

point the reader should note that both threefold and sixfold symmetry can be due to different physics. A sixfold symmetry of an hcp(0001) surface demands, for example, the presence of atomic steps so that both possible hcp domains exist. The side view in figure 41 of the hcp(0001) surface shows an A-layer-terminated hcp(0001) surface. Removing this top layer leads to an B-layer-terminated hcp(0001) surface. Each of the two terminations has threefold symmetry; only their coexistence in a 1:1 ratio leads to sixfold symmetry. However, up to now, it is by no means clear that the growing Zn film possesses an hcp stacking at all, because equally weighted fcc twins would also lead to a sixfold symmetry. Fortunately, LEED $I(E)$ spectra are extremely sensitive to the detailed stacking sequence of the near-surface layer and therefore intensity analyses allow for a detailed determination of the stacking in the Zn film which will be discussed next. This access to stacking was already successfully applied to, for example, epitaxial Co films on Cu(111) [199–201].

Full dynamical LEED intensity analyses were carried out to determine the structure of the Zn films for different thicknesses. Thus, *we never detected any fcc stacking between near-surface film layers.* The film consists of the two described hcp domains only. For low coverages one of the hcp domains dominates and therefore the film shows only threefold symmetry. The percentages of the two domains for three different film thicknesses, together with the first three layer distances, the spacing common to all deeper layers and the in-plane lattice parameter are given in table 11 resulting from the quantitative LEED analyses. The errors given result from the variance of the Pendry R factor [55] (see section 3.4). The last table column gives the values resulting from DFT where the in-plane parameter was adjusted to that determined via LEED. Interestingly, the three top layer distances do not depend on the film thickness. The agreement between the resulting DFT and LEED values is excellent. Figure 46 compares experimental and theoretical best-fit spectra for the 25 ML film which already has sixfold symmetry. Surprisingly, however, there is a discrepancy for the first layer distance (determined by LEED with an accuracy of ± 0.01 Å). A possible reason could be the adsorption of residual gas molecules on the Zn film surface. As we know from our studies [202, 203] for the epitaxial system Ni/Cu(100), such adsorption can lead to considerable expansion of the first film interlayer distance.

The continuous change from three- to sixfold symmetry allows us to speculate with respect to the growth mode. Independent from the actual roughness of the Zn film, layer-by-layer growth cannot account for the transition from three- to sixfold symmetry, only the $I(E)$ curves of (1,0) and (0,1) beams are exchanged after every evaporated Zn monolayer. This situation is illustrated in figure 47: adding one ML to the surface transforms all A domains to B domains,

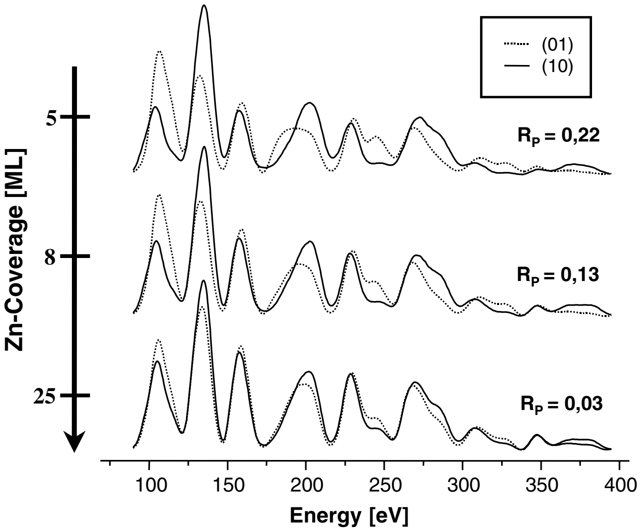

Figure 45. Experimental LEED $I(E)$ spectra of the (1, 0) and (0, 1) beam for three different Zn coverages. For the 25 ML film the spectra are practically identical as expected for a film with sixfold symmetry.

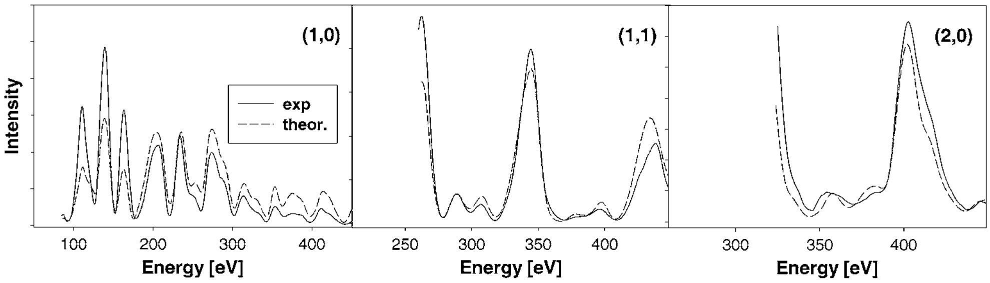

Figure 46. Comparison between experimental and theoretical best-fit LEED spectra for a 25 ML Zn film on Al(111).

and vice versa. Experimentally, this would lead to an exchange of the (1,0) and (0,1) intensities with every additionally deposited Zn ML which, however, was never observed. So, the continuous transition from three- to sixfold symmetry must come by 3d island growth. With increasing Zn coverage the height distribution of Zn islands becomes wider, until both domains reach, on average, a distribution of 50%. Such behaviour was also observed for Co/Cu(111) [199–201].

The question arises, what causes the unequal weight of hcp-Zn domains for low coverages leading to a LEED pattern with threefold symmetry? Unfortunately, DFT calculations of a complete incommensurate Zn layer on an Al(111) substrate would go far beyond the possibilities of today's computers (slabs containing more than 1000 atoms would be necessary). Moreover, the CE cannot be applied, because the ansatz is restricted to coherent problems. However, from our LEED studies we know that in the initial growth most likely a complete layer is formed which causes sharp extra spots in the LEED pattern. With more Zn deposited, the arriving Zn atoms again have the choice to occupy 'nearly' (because of the 7% misfit with respect to the Al substrate) fcc- or hcp-hollow sites. Our DFT calculations carried out for bilayer

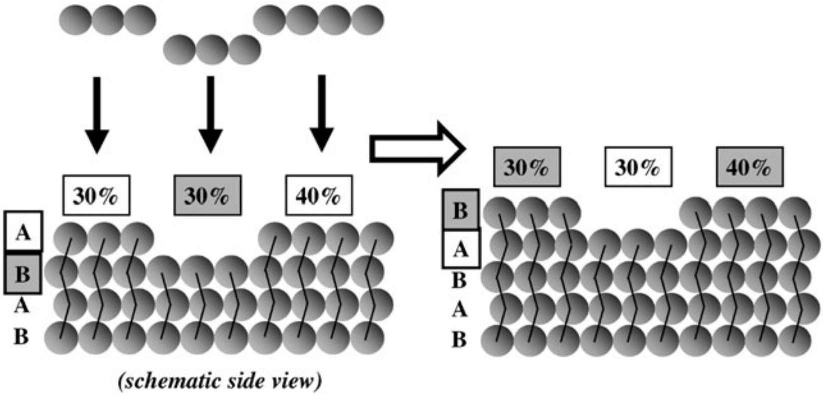

Figure 47. Layer-by-layer growth cannot explain the observed continuous transition from three- to sixfold symmetry as shown by a schematic side view. The evaporation of a complete layer only leads to the exchange of the percentages of A- and B-terminated surface areas.

Table 11. Best-fit parameters resulting from LEED intensity analyses and DFT calculations. Here, d_{mn} stands for the layer distance between the mth and nth film layers, while a_p gives the fitted in-plane lattice parameter. The errors result from the variance, equation (43), of the Pendry R factor [55].

	LEED results			DFT
Parameter	5 ML Zn	8 ML Zn	25 ML Zn	hcp(0001)
Ratio (hcp-dom.)	25:75	30:70	50:50	
d_{12} (Å)	2.46 ± 0.01	2.46 ± 0.01	2.47 ± 0.01	2.43
d_{23} (Å)	2.41 ± 0.02	2.41 ± 0.02	2.41 ± 0.02	2.41
d_{34} (Å)	2.41 ± 0.04	2.43 ± 0.04	2.43 ± 0.03	2.43
d_b (Å)	2.45 ± 0.04	2.45 ± 0.03	2.45 ± 0.03	2.45
a_p (Å)	2.66 ± 0.03	2.66 ± 0.02	2.66 ± 0.02	2.66 (fix)
R_p	0.108	0.107	0.079	

high islands find that, indeed the occupation of 'nearly' fcc sites is clearly preferred over hcp-sites by 16 meV/Zn atoms. The reason is the following: Al atoms in the top substrate layer with positions 'nearly' directly underneath the hcp-hollow site of the film layer repulsively interact with a Zn atom occupying the 'nearly' hcp-hollow site. The mentioned repulsive interaction can be avoided by occupying the 'nearly' fcc-hollow site with no Al atom underneath. As discussed above, three-dimensional growth starts with the second Zn layer so that this second growing layer is not yet completed when the next layer starts to grow. We even calculated the energetic situation for three ML high Zn islands: the two stacking possibilities on an relaxed fcc-stacked bilayer are nearly energetically degenerated, i.e. the influence of the Al substrate on the film energetics disappears. So, the unequal weight of the two hcp domains for low coverages is most likely caused by the initial growth of the second Zn layer.

The results above hint towards the following scenario: from the very beginning, Zn forms incommensurate islands, until a complete incommensurate ML with a well-defined orientation (dictated by the Al substrate) exists leading to sharp LEED extra spots. When the second layer starts to grow the fcc stacking sequence of the substrate orientation is still preferred due to the repulsive interaction between hcp-site-deposited Zn atoms and Al atoms in the first substrate layer. With the first Zn layer completed, three-dimensional island growth sets in and the preference for occupying fcc sites is lost. With further increasing Zn coverage, island growth leads to unequally weighted hcp domains, equivalent to a continuous transition from threefold to sixfold symmetry, as observed by LEED.

Although the investigations above were carried out for the special model system Zn/Al(111), we believe that the results should be representative for the Al–Zn(111) surface for the following reasons:

(i) The predicted ground state via CE for an fcc-based $Al_{0.92}Zn_{0.08}$ alloy with (111) surface orientation consists of a purely Zn block near the surface, separated from Al by an interface along [111]. Following the discussion above, this should cause the development of a *grain boundary*.

(ii) The equilibrium lattice constant of Al-rich Al–Zn alloys is within $\frac{5}{1000}$ Å, identical to that of pure fcc-Al.

Methodologically, we see that the combination of quantitative LEED, DFT and CE permits a detailed structural characterization of near-surface interfaces, even if the interface considered represents a grain boundary. The understanding of such interfaces with respect to their detailed atomic structure may also help to learn more about grain boundaries in bulk alloys. Nevertheless, the transformation of the results to real Al–Zn(111) alloys is still an assumption, i.e. experimental studies of these alloy surfaces are highly desirable.

6. Summary

The quantitative description of the properties of binary metal alloy is a very delicate task: on the one hand, the theoretical model should be based on quantum mechanics to be as accurate as possible, while, on the other hand, the description should allow us to study problems ranging from the atomic to the micrometre length scale. Additionally, the temperature dependence of quantities considered must be taken into account. Therefore, *the main aim of this work was to illustrate the present status in the field in this sense and to demonstrate the considerable improvements having become possible by recent methodological developments.* The applied combination of quantum mechanics and statistical physics via DFT, CE and MC simulations creates the, up to now, most successful approach to describe the phase stability and formation of metal alloys and their surfaces.

Since the results of this combination reach an accuracy rendering a quantitative comparison with experimental data possible, the method allows us to check directly the correctness of our calculations (e.g. by LEED structure determinations in the case of surface studies) as well as to settle our quantitative understanding of alloy properties. Examples are the influence of SRO on mixing enthalpies, the shape controlling factors of characteristic microstructures in quenched solid solutions or the energetic terms which determine the segregation profile at an alloy surface.

Apart from their practical importance, the alloy problems presented were also selected to demonstrate the large range of applications of the method. Thus, some long-standing questions could be answered and experimental discrepancies removed. Indeed, the new methods' treatment of different alloy phenomena allows us to study important properties such as

- *Ground states:* extended ground-state searches for α-brass and Ag–Pd detect the existence of low-temperature ground states as an important expansion of the corresponding phase diagrams. While in the case of α-brass our prediction perfectly agrees with experimental studies, for Ag–Pd an experimental verification is still lacking and would be highly desirable.

- *Short-range order:* for a quantitative experiment–theory agreement, calculations of mixing enthalpies of solid solutions demand a consideration of SRO. This was demonstrated for α-brass, where the SRO parameters determined agree very well with experimental data. The extension of 'CE plus MC' to treat alloy surfaces was applied to identify the SRO behaviour of Co antisites in the topmost layer of CoAl(100) as determined by quantitative LEED, and also applied in the present work.
- *Precipitation—morphology and dynamics of microstructures:* the possibility to study giant configurations consisting of many thousands of atoms with our approach was applied to calculate the size–shape relation of coherent Zn precipitates in Al–Zn alloys, whereby again excellent agreement with experiment was reached. Our results led to an important extension of today's understanding of the shape-controlling factors of precipitates: the observed faceting of microstructures at low temperatures can only be explained by the anisotropy of the interfacial energy rather than by the strain energy which, however, is responsible for the observed flattening of precipitates. Moreover, a kinetic MC approach was developed in order to study the dynamics of the microstructures. Their distribution follows classical Ostwald ripening.
- *Surface segregation:* as an important example of surface segregation, the segregation of TM defect atoms in the B2 structure of TM-Al alloys was studied. The investigations solve some experimental discrepancies regarding the NiAl(100) surface and allow us to develop a model which places the three related systems NiAl(100), FeAl(100) and CoAl(100) in one consistent picture. The surface properties of these systems are controlled by very small off-stoichiometries from the ideal concentration of 50% Al. The theoretical predictions agree with experimental data resulting from the—again quantum-mechanical—evaluation of LEED intensities.
- *Grain boundaries:* finally, we have seen that the combination of DFT, CE and MC with LEED structure determination even allows us to learn more about incoherence. In the case of the fcc-based system Al–Zn, the heavily segregating Zn atoms lead to a grain boundary between the segregated Zn layers and the Al-rich Al–Zn alloy driven by the energy gain of the Zn layer by giving up the instable fcc phase.

Since the approach used is only a few years' old, its application potential is by no means already reached. There are a number of solid properties which may be treated via DFT, CE and MC after some further development, such as, for example, nucleation processes, the initial growth of epitaxial films, island growth on surfaces or an extension to ternary metal systems. Since the approach allows us to describe the behaviour of real alloy systems, a strong interplay with experimental groups is highly desirable.

Acknowledgments

From all the people who made this article possible special thanks go to Klaus Heinz for his constructive advice over many years, his faith in me and his friendship. Except for the Ni–Al analysis, all LEED structure determinations presented in this work were performed in his group. I am happy to be a part of it. Special thanks also go to Alex Zunger for all the lessons and many valuable discussions during my time in his group. The continuing collaboration with him, Chris Wolverton (special thanks for the lessons in metallurgy) and Lin-Wang Wang formed the basis for the successful application of DFT and CE to the presented alloy problems. I would also like to express my gratitude to Lutz Hammer for the many useful comments and discussions about alloy and metal surfaces. The experiments on Al–Zn surfaces were done by Monika Wendler. Ole Wieckhorst performed the calculations on Fe–Al, Co–Al and Ni–Al surfaces. Many thanks! Valuable and stimulating discussions with Volker Blum, Sebastian Walter, Ralf Drautz, Manfred Fähnle, Matthias Scheffler and Raimund Podloucky are gratefully acknowledged. Part of this work was supported by the US Department of Energy and the Deutsche Forschungsgemeinschaft.

References

[1] Maddox J 1988 *Nature* **335** 7

[2] Hohenberg P and Kohn W 1964 *Phys. Rev.* **136** 864B

[3] Kohn W and Sham L J 1965 *Phys. Rev.* **140** 1133A

[4] Sanchez J M, Ducastelle F and Gratias D 1984 *Physica* A **128** 334

[5] Pendry J B 1974 *Low Energy Electron Diffraction* (London: Academic)

[6] Van Hove M A and Tong S Y 1979 *Surface Crystallography by LEED* (Berlin: Springer)

[7] Hume-Rothery W, Mabbott G W and Channel-Evans K M 1934 *Phil. Trans. R. Soc.* A **233** 1

[8] Miedema A R, de Boer F R and de Chatel P F 1973 *J. Phys. F: Met. Phys.* **3** 1558

[9] Pettifor D G 1993 *Electron Theory of Crystal Structure in Structure of Solids* ed V Gerold (Weinheim: VCH)
Pettifor D G 1988 *Meas. Sci. Technol.* **4** 2480 and references therein

[10] Zunger A 1980 *Phys. Rev. Lett.* **44** 592
Zunger A 1980 *Phys. Rev.* B **22** 5834
Zunger A 1981 *Structure and Bonding in Crystals* vol 1, ed M O Keefe and A Navrotsky (London: Academic) p 73

[11] Villars P 1983 *J. Less-Common. Met.* **92** 215
Villars P 1984 *J. Less-Common. Met.* **99** 33

[12] Bieber A and Gautier F 1986 *Acta Metall.* **34** 2291

[13] Catlow C R and Mackrodt W C 1982 *Computer Simulations in Solids* vol 1 (Berlin: Springer)

[14] Daw M S and Baskes M I 1983 *Phys. Rev. Lett.* **50** 1285

[15] Foiles S M 1990 *Surface Segregation and Related Phenomena* ed P A Dowben and A Miller (Boca Raton, FL: Chemical Rubber Company Press) p 79

[16] Treglia G, Legrand B, Ducastelle F, Saul A, Gallis C, Meunier I, Mottet C and Senhaji A 1999 *Comput. Mater. Sci.* **15** 196

[17] Kikuchi R, Sanchez J M, de Fontaine D and Yamaguchi H 1980 *Acta Metall.* **28** 651
Sanchez J M, Barefoot J R, Jarrett R N and Tien J K 1984 *Acta Metall.* **32** 1519

[18] Sigli C and Sanchez J M 1985 *Acta Metall.* **33** 1097

[19] Ducastelle F and Gautier N 1976 *J. Phys. F: Met. Phys.* **6** 2039

[20] Sluiter M and Turchi P E A 1989 *Phys. Rev.* B **40** 11215

[21] Drchal V, Pasturel A, Monnier R, Kudrnovsky J and Weinberger P 1999 *Comput. Mater. Sci.* **15** 144

[22] Ruban A V and Skriver H L 1999 *Comput. Mater. Sci.* **15** 119

[23] Hultgren R, Desai P D, Hawkins D T, Gleiser M and Kelley K K 1973 *Selected Values of the Thermodynamic Properties of Binary Alloys* (Metals Park, OH: American Society for Metals)

[24] Villars P and Calvert L D 1991 *Pearson's Handbook of Crystallographic Data* (Materials Park, OH: ASM International)

[25] Hansen M 1958 *Constitution of Binary Alloys* (New York: McGraw-Hill)

[26] Massalski T B 1986 *Binary Alloy Phase Diagram* ed J L Murray, L H Bennett and H Baker (Metals Park, OH: American Society Metals)

[27] Brown K R, Venie M S and Woods R A 1995 *JOM* **7** 20

[28] Hatch J E 1998 *Aluminum: Properties and Physical Metallurgy* (Metals Park, OH: American Society for Metals)

[29] Davisson C J and Germer L H 1927 *Nature* **119** 558

[30] Ziman J M 1979 *Models of Disorder* (Cambridge: Cambridge University Press)

[31] Muto T and Takagi Y 1955 *Solid State Phys.* **1** 193

[32] Guttman L 1956 *Solid State Phys.* **3** 145

[33] Cowley J M 1950 *J. Appl. Phys.* **21** 24

[34] Krivoglaz M A 1996 *X-Ray and Neutron Diffraction in Nonideal Crystals* (Berlin: Springer)

[35] Sparks C J and Borie B 1966 *Local Arrangements Studied bx X-Ray Diffraction* ed J B Cohen and J E Hilliard (New York: Gordon and Breach)
Sparks C J and Borie B 1966 *Met. Soc. Conf.* **36** 5
Borie B and Sparks C J 1964 *Acta Crystallogr.* **17** 827

[36] Schönfeld B 1999 *Prog. Mater. Sci.* **44** 435

[37] Hume-Rothery W, Smallman R E and Haworth C W 1969 *Structure of Metals and Alloys* (London: Institute of Metals)

[38] Miedema A R and de Chatel P F 1980 *Theory of Alloy Phase Formation* ed L H Bennett (Warrendale, PA: The Metallurgical Society of the AIME) p 344

[39] Miedema A R, de Chatel P F and de Boer F R 1980 *Physica* B **100** 1 and references therein

[40] Alonso J A and March N H 1990 *Electrons in Metals and Alloys* (London: Academic)

[41] Pettifor D G and Podloucky R 1984 *Phys. Rev. Lett.* **53** 1080

[42] Pettifor D G 1984 *Solid State Commun.* **51** 31

[43] Voter A F 1986 *Phys. Rev.* B **34** 6819

[44] Zunger A 1994 *Statics and Dynamics of Alloy Phase Transformations* (*NATO ASI Series*) ed P E A Turchi and A Gonis (New York: Plenum) p 361

[45] Wolverton C 1999 *Phil. Mag. Lett.* **79** 683

[46] Müller S, Wolverton C, Wang L-W and Zunger A 2000 *Acta Mater.* **48** 4007

[47] Müller S, Wang L-W and Zunger A 2002 *Model. Sim. Mater. Sci. Eng.* **10** 131

[48] Sachtler W M H and von Santen R A 1979 *Appl. Surf. Sci.* **3** 121

[49] Burton J J and Machlin E S 1976 *Phys. Rev. Lett.* **37** 1433

[50] Watson P R, Van Hove M A and Hermann K 1999 *NIST Surface Structure Database* version 3.0 (Gaithersburg, MD: National Institute of Standards and Technology)

[51] Drautz R, Reichert H, Fähnle M, Dosch H and Sanchez J M 2001 *Phys. Rev. Lett.* **87** pp 236102-1

[52] Van Hove M A, Moritz W, Over H, Rous P J, Wander A, Barbieri A, Materer N, Starke U and Somorjai G A 1993 *Surf. Sci. Rep.* **19** 191

[53] Heinz K 1988 *Prog. Surf. Sci.* **27** 239
Heinz K 1995 *Rep. Prog. Phys.* **58** 637

[54] Heinz K and Hammer L 1998 *Z. Kristallogr.* **213** 615

[55] Pendry J B 1980 *J. Phys. C: Solid State Phys.* **13** 937

[56] Van Hove M A, Weinberg W H and Chan C-M 1986 *Low-Energy Electron Diffraction* (*Springer Series in Surface Science vol 6*) (Berlin: Springer)

[57] Rous P J, Pendry J B, Saldin D K, Heinz K, Müller K and Bickel N 1986 *Phys. Rev. Lett.* **57** 2951

[58] Rous P J and Pendry J B 1989 *Surf. Sci.* **219** 355
Rous P J and Pendry J B 1989 *Surf. Sci.* **219** 373

[59] Heinz K and Hammer L 1999 *J. Phys.: Condens. Matter* **11** 8377

[60] Heinz K, Müller S and Hammer L 1999 *J. Phys.: Condens. Matter* **11** 9437

[61] Müller S, Prieto J E, Rath C, Hammer L, Miranda R and Heinz K 2001 *J. Phys.: Condens. Matter* **13** 1793

[62] Müller S, Prieto J E, Krämer T, Rath C, Hammer L, Miranda R and Heinz K 2001 *J. Phys.: Condens. Matter* **13** 9897

[63] Blum V and Heinz K 2001 *Comput. Phys. Commun.* **134** 392

[64] Kottcke M and Heinz K 1997 *Surf. Sci.* **376** 352

[65] Döll R, Kottcke M and Heinz K 1993 *Phys. Rev.* B **48** 1973

[66] Löffler U, Döll R, Heinz K and Pendry J B 1994 *Surf. Sci.* **301** 346

[67] Blum V, Hammer L, Meier W, Heinz K, Schmid M, Lundgren E and Varga P 2001 *Surf. Sci.* **474** 81

[68] Fernando G W, Watson R E and Weinert M 1992 *Phys. Rev.* B **45** 8233

[69] Johnson D D, Nicholson D M, Pinski F J, Gyorffy B L and Stocks G M 1986 *Phys. Rev. Lett.* **56** 2088

[70] Zunger A, Wei S-H, Ferreira L G and Bernard J E 1990 *Phys. Rev. Lett.* **65** 353

[71] Payne M C, Teter M P, Allen D C, Arias T A and Joannopoulos J D 1992 *Rev. Mod. Phys.* **64** 1064

[72] Jones R O and Gunnarsson O 1989 *Rev. Mod. Phys.* **61** 689

[73] Dreizler R M and Gross E K U 1990 *Density Functional Theory* (Berlin: Springer)

[74] Dreizler R M and da Providencia J 1985 *Density Functional Theory* (New York: Plenum)

[75] Krachko E S and Ludena E V 1990 *Energy Density Functional Theory of Many Electron Systems* (Boston, MA: Kluwer–Academic)

[76] Ceperley D M and Alder B J 1980 *Phys. Rev. Lett.* **45** 567

[77] Perdew J P and Zunger A 1981 *Phys. Rev.* B **23** 5048

[78] Perdew J P and Wang Y 1992 *Phys. Rev.* B **45** 13244

[79] Singh D J 1994 *Planewaves, Pseudopotentials and the LAPW Method* (Boston, MA: Kluwer)

[80] Hamann D R, Schlüter M and Chiang C 1979 *Phys. Rev. Lett.* **43** 1494

[81] Troullier N and Martins J L 1991 *Phys. Rev.* B **43** 1993

[82] Vanderbilt D 1990 *Phys. Rev.* B **41** 7892

[83] Kresse G and Hafner J 1994 *J. Phys.: Condens. Matter* **6** 8245

[84] Kresse G and Joubert D 1999 *Phys. Rev.* B **59** 1758

[85] Blöchl P E 1994 *Phys. Rev.* B **50** 17953

[86] Wang L-W, unpublished: This code was developed at the National Renewable Energy Laboratory and later at NERSC Computer Centre, Berkeley. Some details can be found in the Appendix of Müller S *et al* 1999 *Phys. Rev.* B **60** 16448

[87] Kresse G and Furthmüller J 1996 *Phys. Rev.* B **54** 11169
Kresse G and Furthmüller J 1996 *Comput. Mater. Sci.* **6** 15

[88] Blaha P, Schwartz K and Luitz J 1997 *WIEN97, A Full Potential Linearized Augmented Plane Wave Package for Calculating Crystal Properties* Technical University of Vienna
This is an improved and updated Unix version of the original copyrighted WIEN code, which was published by
Blaha P, Schwarz K, Sorantin P and Trickey S B 1990 *Comput. Phys. Commun.* **59** 399

[89] Lu Z W, Laks D B, Wei S-H and Zunger A 1994 *Phys. Rev.* B **50** 6642

[90] Laks D B, Ferreira L G, Froyen S and Zunger A 1992 *Phys. Rev.* B **46** 12587

[91] Wolverton C, Ozoliņš V and Zunger A 1998 *Phys. Rev.* B **57** 4332

[92] Zunger A 1994 *Handbook of Crystal Growth* vol 3, ed T D J Hurle (Amsterdam: Elsevier) p 997 and references therein

[93] Wood D M and Zunger A 1988 *Phys. Rev. Lett.* **61** 1501

[94] Müller S, Wang L-W, Zunger A and Wolverton C 1999 *Phys. Rev.* B **60** 16448

[95] Ozoliņš V, Wolverton C and Zunger A 1998 *Phys. Rev.* B **57** 4816

[96] Ozoliņš V, Wolverton C and Zunger A 1998 *Phys. Rev.* B **57** 6427

[97] Bottomeley D J and Fons P 1978 *J. Cryst. Growth* **44** 513

[98] de Gironcoli S, Giannozzi P and Baroni S 1991 *Phys. Rev. Lett.* **66** 2116

[99] Sigli C and Sanchez J M 1988 *Acta Metall.* **36** 367

[100] Gyorffy B L and Stocks G M 1983 *Phys. Rev. Lett.* **50** 374

[101] Johnson D D, Nicholson D M, Pinski F J, Gyorffy B L and Stocks G M 1986 *Phys. Rev. Lett.* **56** 2088

[102] Conolly J W D and Williams A R 1983 *Phys. Rev.* B **27** 5169

[103] Zunger A, Wang L G, Hart G L W and Sanati M 2002 *Model. Sim. Mater. Sci. Eng.* **10** 685

[104] Ferreira L G, Wei S-H and Zunger A 1991 *J. Supercomp. Appl.* **5** 34

[105] Hart G L W and Zunger A 2001 *Phys. Rev. Lett.* **87** 275508

[106] Wolverton C, Ozoliņš V and Zunger A 2000 *J. Phys.: Condens. Matter* **12** 2749

[107] Metropolis N, Rosenbluth A W, Rosenbluth M V, Teller A and Teller E 1974 *J. Chem. Phys.* **60** 1071

[108] Toda M, Rubo R and Saito N 1983 *Statistical Physics* vol 1 (Berlin: Springer)

[109] Fichthorn K A and Weinberg W H 1991 *J. Chem. Phys.* **95** 1090

[110] Börtz A B, Kalos M H and Lebowitz J L 1975 *J. Comput. Phys.* **17** 10

[111] Jacobsen J, Jacobsen K W, Stoltze P and Norskov J K 1995 *Phys. Rev. Lett.* **74** 2295

[112] Wang Y, Chen L-Q and Khachaturyan A G 1991 *Scr. Metall.* **25** 1387

[113] Chan L-Q and Khachaturyan A G 1992 *Phys. Rev.* B **46** 5899

[114] Wang Y, Chen L-Q and Khachaturyan A G 1993 *Acta Metall.* **41** 279

[115] Dobretsov V Y, Vaks V and Martin G 1996 *Phys. Rev.* B **54** 3227

[116] Rubin G and Khachaturyan A G 1999 *Acta Mater.* **47** 1995

[117] Lee J K 1997 *Mater. Sci. Eng.* A **238** 1

[118] Choy J-H and Lee J K 2000 *Mat. Sci. Eng.* A **285** 195

[119] Lee J K 1996 *Metall. Mater. Trans.* A **27** 1449

[120] Guinier A 1959 *Solid State Phys.* **9** 293

[121] Swendson R H and Wang J-S 1987 *Phys. Rev. Lett.* **58** 86

[122] Wolff U 1989 *Phys. Rev. Lett.* **62** 361

[123] Soisson F, Barbu A and Martin G 1996 *Acta Mater.* **44** 3789

[124] Binder K and Heermann D W 1988 *Monte Carlo Simulations in Statistical Physics* (Berlin: Springer)

[125] Kellogg G L and Feibelman P 1990 *Phys. Rev. Lett.* **64** 3143

[126] Stumpf R and Scheffler M 1994 *Phys. Rev. Lett.* **72** 254

[127] Krüger P and Pollmann J 1995 *Phys. Rev. Lett.* **74** 1155

[128] Bechstedt F, Stekolnikov A A, Furthmüller J and Käckell P 2001 *Phys. Rev. Lett.* **87** 016103

[129] Oppo S, Fiorentini V and Scheffler M 1993 *Phys. Rev. Lett.* **71** 2437

[130] Scheffler M and Stampfl C 1999 *Handbook of Surface Science* ed K Horn and M Scheffler (Amsterdam: Elsevier) p 286

[131] Pentcheva R and Scheffler M 2000 *Phys. Rev.* B **61** 2211

[132] Spisak D and Hafner J 2001 *Phys. Rev.* B **63** 094424

[133] Walter S, Blobner F, Krause M, Müller S, Heinz K and Starke U 2003 *J. Phys.: Condens. Matter* **15** 5207

[134] Lippmann B A and Schwinger J 1950 *Phys. Rev.* **79** 469

[135] Sakurai J J 1985 *Modern Quantum Mechanics* (Redwood City, CA: Addison-Wesley)

[136] Beeby J L 1964 *Phys. Rev.* **135** A130

[137] Aitchison L 1969 *A History of Metals* (London: MacDonald and Evans)

[138] Hume-Rothery W 1931 *The Metallic State* (London: Oxford University Press)

[139] Reinhard L, Schönfeld B, Kostorz G and Bührer W 1990 *Phys. Rev.* B **41** 1727

[140] Sato H and Toth R S 1961 *Phys. Rev.* **124** 1833

[141] Johnson D D, Nicholson D M, Pinski F J, Gyorffy B L and Stocks G M 1990 *Phys. Rev.* B **41** 9701

[142] Turchi P E A, Sluiter M, Pinski F J, Johnson D D, Nicholson D M, Stocks G M and Staunton J B 1991 *Phys. Rev. Lett.* **67** 1779

[143] Turchi P E A, Sluiter M, Pinski F J, Johnson D D, Nicholson D M, Stocks G M and Staunton J B 1992 *Phys. Rev. Lett.* **68** 418 (erratum)

[144] Müller S and Zunger A 2001 *Phys. Rev.* B **63** 094294

[145] Faulkner J S and Stocks G M 1981 *Phys. Rev.* B **23** 5628

[146] Terasaki O and Watanabe D 1981 *Japan. J. Appl. Phys.* **20** 381

[147] Broddin D, Van Tendeloo G, Van Landuyt J and Amelinckx S 1988 *Phil. Mag.* B **57** 31

[148] Broddin D, Van Tendeloo G, Van Landuyt J, Amelinckx S, Portier R, Guymont M and Loiseau A 1986 *Phil. Mag.* A **54** 395

[149] Predel B 1991 *Phase Equilibria, Crystallographic and Thermodynamic Data of Binary Alloys* (*Landolt–Börnstein New Series*) Group IV, vol 5a (Berlin: Springer)

[150] Clark J F, Pinski F J, Johnson D D, Sterne P A, Staunton J B and Ginatempo B 1995 *Phys. Rev. Lett.* **74** 3225

[151] Chan J P and Hultgren R 1969 *J. Chem. Thermodyn.* **1** 45

[152] Abrikosov I A and Skriver H L 1993 *Phys. Rev.* B **47** 16532

[153] Takizawa S, Terakura K and Mohri T 1989 *Phys. Rev.* B **39** 5792

[154] Gonis A, Butler W H and Stocks G M 1983 *Phys. Rev. Lett.* **50** 1482

[155] Johnson R A 1990 *Phys. Rev.* B **41** 9717

[156] Takano N, Yoshikawa A and Terasaki F 1998 *Solid State Commun.* **107** 213

[157] Chae K H, Jung S M, Lee Y S, Whang C N, Seon Y, Croft M, Sills D, Ansari P H and Mack K 1996 *Phys. Rev.* B **53** 10328

[158] Coulthard I and Sham T K 1996 *Phys. Rev. Lett.* **77** 4824

[159] Williams R K 1982 *Scr. Metall.* **16** 683

[160] Raoufi A, Arajs S and Rao K V 1986 *Phys. Status Solidi* a **97** 571

[161] Müller S and Zunger A 2001 *Phys. Rev. Lett.* **87** 165502-1

[162] an Mey S 1993 *Z. Metallk.* **84** 451

[163] Lukas H L, Henig E-T and Zimmermann B 1977 *Calphad* **I** 225

[164] Wittig F E and Schöffl L 1960 *Z. Metallk.* **51** 700

[165] Connel R A and Downie D B 1973 *Met. Sci. J.* **7** 12

[166] Hilliard J E, Averbach B L and Cohen M 1954 *Acta Metall.* **2** 621

[167] Cohen J B 1986 *Solid State Phys.* **39** 131

[168] Khachaturyan A G 1983 *Theory of Structural Transformations in Solids* (New York: Wiley)

[169] Zandberger H W, Andersen S J and Jansen J 1997 *Science* **277** 1221

[170] Ramlau R and Löffler H 1983 *Phys. Status Solidi* a **79** 141

[171] Laslaz G and Guyot P 1977 *Acta Metall.* **25** 277

[172] Bubeck E, Gerold V and Kostorz G 1985 *Cryst. Res. Technol.* **20** 97

[173] Hübner G, Löffler H and Wendrock G 1986 *Cryst. Res. Technol.* **21** 8

[174] Fumeron M, Guillot J P, Dauger A P and Caisso J 1980 *Scr. Metall.* **14** 189

[175] Deguercy J, Denanot M F, Fumeron M, Guillot J P and Caisso J 1982 *Acta Mater.* **30** 1921

[176] Gerold V, Siebke W and Tempus G 1987 *Phys. Status Solidi* a **104** 213

[177] Müller S, Wolverton C, Wang L-W and Zunger A 2001 *Europhys. Lett.* **55** 33

[178] Cahn J 1961 *Acta Metall.* **9** 795

[179] Herring C 1953 *Structure and Properties of Solid Surfaces* ed R Gomer and C S Smith (Chicago, IL: University of Chicago Press) p 5

[180] Haeffner D R and Cohen J B 1989 *Acta Metall.* **37** 2185

[181] Vosko S H, Wilk L and Nusair M 1980 *Can. J. Phys.* **58** 1200

[182] Davis H L and Noonan J R 1988 *The Structure of Surfaces* vol 2, ed J F van der Veen and M A Van Hove (Berlin: Springer)

[183] Mullins D R and Overbury S H 1988 *Surf. Sci.* **199** 141

[184] Roos W D, du Plessis J, van Wyk G N, Taglauer E and Wolf S 1996 *J. Vac. Sci. Technol.* A **14** 1648

[185] Stierle A, Formoso V, Comin F and Franchy R 2000 *Surf. Sci.* **467** 85

[186] Blum R-P, Ahlbehrendt D and Niehus H 1996 *Surf. Sci.* **366** 107

[187] Meier W, Blum V, Hammer L and Heinz K 2001 *J. Phys.: Condens. Matter* **13** 1781

[188] Blum V, Hammer L, Schmidt Ch, Meier W, Wieckhorst O, Müller S and Heinz K 2002 *Phys. Rev. Lett.* **89** 266102

[189] Bester G, Meyer B and Fähnle M 1999 *Phys. Rev.* B **60** 14492

[190] Ruban A V 2002 *Phys. Rev.* B **65** 174201

[191] Pourovskii L V, Ruban A V, Johansson B and Abrikosov I A 2003 *Phys. Rev. Lett.* **90** 026105

[192] Blum V, Hammer L, Meier W and Heinz K 2001 *Surf. Sci.* **488** 219

[193] Sadigh B, Asta M, Ozolins V, Schmid A K, Bartelt N C, Quong A A and Hwang R Q 1999 *Phys. Rev. Lett.* **83** 1379

[194] Ozoliņš V, Asta M and Hoyt J J 2002 *Phys. Rev. Lett.* **88** 096101

[195] Stampfl C, Kreuzer H J, Payne S H, Pfnür H and Scheffler M 1999 *Phys. Rev. Lett.* **83** 21993

[196] Bonn M, Funk S, Hess C, Denzler D N, Stampfl C, Scheffler M, Wolf M and Ertl G 1999 *Science* **285** 1042

[197] Reichert H 2002 private communication

[198] Müller S, Hammer L, Wendler M and Heinz K 2003 at press

[199] Müller S, Kostka G, Schäfer T, de la Figuera J, Prieto J E, Ocal C, Miranda R, Heinz K and Müller K 1996 *Surf. Sci.* **352–354** 46

[200] Rath C, Prieto J E, Müller S, Miranda R and Heinz K 1997 *Phys. Rev.* B **55** 10791

[201] Prieto J E, Rath C, Müller S, Miranda R and Heinz K 1998 *Surf. Sci.* **401** 248

[202] Müller S, Schulz B, Kostka G, Farle M, Heinz K and Baberschke K 1996 *Surf. Sci.* **364** 235

[203] Platow W, Bovensiepen U, Poulopoulos P, Farle M, Baberschke K, Hammer L, Walter S, Müller S and Heinz K 1999 *Phys. Rev.* B **59** 12641